Theoretical study for physical meanings of the grain-size distribution (GSD) in pyroclastic fall deposits with applications to the 2011 Shinmoe-dake subplinian eruption

入山, 宙

Theoretical study for physical meanings of the grain-size distribution (GSD) in pyroclastic fall deposits with applications to the 2011 Shinmoe-dake subplinian eruption

March 2017

Doctoral Dissertation

Yu Iriyama

Department of Earth and Planetary Sciences,

Graduate School of Science, Kyushu University.

Abstract

Grain–size distributions (GSDs) of pyroclasts play a significant role of the explosive volcanic eruptions. To reconstruct the temporal change of the volcanic activity quantitatively, it is necessary to establish a methodology by using the spatial variations of GSDs in pyroclastic fall deposits. The author carried out a theoretical study for the transportation and sedimentation processes of pyroclasts. The author first defined the GSD function to explain the temporal and the spatial variations of the GSD depending on the particle size and surrounding environment. By using the GSD function, the author formulated one–dimensional and two–dimensional theories, and established models. The established models enable to estimate the eruption duration from the characteristic sedimentary structure, and the temporal variation of the source GSD from the stratigraphic variation of GSD in the deposit. The steady–state model enables to identify the cause of the grading structure. The author applied the established models to the 2011 Shinmoe–dake subplinian eruption. The estimated supply duration was similar to the observed eruption duration. Then, we estimated the temporal change of the source GSD. According to the estimated source GSD and the observed eruption column height, the expected change of the mass eruption rate was consistent to the geodetic volume change. In case of the 2011 Shinmoe–dake subplinian eruption, it was suggested that the cause of the reverse grading structure shown in the lower part of the deposit was caused not by the effect of the steady–state transportation, but by the effect of the temporal change of the eruption. It is expected that the established theory and models are applicable to apply to various types of the fall deposits all over the world.

Contents

Chapter 1

Introduction

A plinian eruption is a kind of the explosive volcanic activity in which the duration of a single eruption extends from a few hours to about a day. Large amount of the mixture of pyroclasts and gas is released owing to the eruption, which has a serious effect on human lives and economy. Furthermore, there are some cases in that lava effusion eruption and/or caldera forming eruption follow a plinian eruption. Thus, to devise effective schemes of disaster prevention before the eruption, it is important to figure out the mechanism of the temporal change of the volcanic activities in a single eruption and the relationship among the pre–plinian phase, main plinian phase, and post–plinian phase. Thanks to the recent geophysical observations, it has been reported the relationship among the temporal variations of volcanic processes such as eruption column height, crustal deformation, seismic tremor, and infrasonic tremor during a single eruption (e.g., Shimbori et al., 2013; Kozono et al., 2013; Ueda et al., 2014; Ichihara 2016). In case of the 2011 Shinmoe–dake subplinian eruptions, Japan, it was reported that seismic and infrasonic tremors, eruption column height, and magma discharge rate during the eruption are correlated each other (Ichihara, 2016). Similarly, it is expected that the grain–size distribution (GSD) of pyroclasts at the vent also temporally changes.

To take a temporal variation of GSD of ejecta at the vent during the eruption, two observation methods can be thought: in–situ observation during the eruption by using remote sensing and reconstruction from the pyroclastic fall deposit after the eruption.

Recently, it has become possible to observe the GSD of ejecta directly by using remote sensing. However, there are few observation examples to obtain the GSD of ejecta from in–situ observations. Thus, it is necessary to develop a theory to reconstruct the temporal variation of GSDs of ejecta and to provide the physical meanings of GSDs from the pyroclastic fall deposits.

In terms of the GSD and the amount of pyroclasts, researchers have studied about the dispersal of pyroclasts, stratigraphy, total grain–size distribution (TGSD), and total amount of ejecta, and have understood their physical meanings. Total amount of pyroclasts is obtained from the horizontal distribution of the thickness of the pyroclastic fall deposit, which corresponds to intensity of eruption (Pyle, 1989; Fierstein and Nathenson, 1992; Bonadonna et al., 1998; Bonadonna and Houghton, 2005, Bonadonna and Costa, 2012). TGSD of pyroclasts is also obtained from the horizontal distribution of pyroclasts. TGSD retains fundamental information on fragmentation mechanisms (e.g., Kaminski and Jaupart, 1998; Rust and Cashman, 2011) and is suggested the statistical relationship to the eruption column height (Costa et al., 2016).

Dispersal of pyroclasts also has been related to volcanic activities. Eruption style is defined by the characteristic values of the thickness of the pyroclastic fall deposit and GSD (Walker, 1973, 1980). Total amount of pyroclasts, TGSD, and expansion rate of an umbrella cloud are estimated by the horizontal variation of GSD in the entire sediment owing to the theoretical study (Koyaguchi, 1994; Koyaguchi and Ohno, 2001). Distribution of the thickness of the sediment is theoretically obtained from the simple assumptions of tephra transportation (Suzuki, 1983). After Suzuki (1983), various tephra transport and dispersal models (TTDMs) have been made to forecast ash dispersal (e.g., Folch, 2012). On the other hand, theories of plume dynamics and clast transport have been developed (e.g., Wilson, 1976; Sparks, 1986). Numerical study of the transport of lithic fragments enables us to estimate the eruption column height from the dispersal of maximum lithic (ML) fragments (Carey and Sparks, 1986). A numerical study on plume dynamics re-

ported that GSD of pyroclasts influences on the maximum plume height and the rate of ash injection into the atmosphere (Girault et al., 2014). In the case of a pyroclastic fall deposit in the deep sea, it is possible to estimate the eruption duration from the stratigraphic variations of the largest particle size and the smallest one (Ledbetter and Sparks, 1979).

Empirical, theoretical, and numerical studies shown above are helpful to reconstruct the temporal variation of the volcanic activity. In fact, the temporal change of the eruption column height has been reconstructed by extending the method of Carey and Sparks (1986) to including stratigraphic variations of ML (e.g., Carey and Sigurdsson, 1987). However, this method deals with only ML dispersal, the physical meanings of the spatial variations of the GSD of pyroclasts remain poorly understood. While it is thought that stratigraphic variations of GSDs in pyroclastic fall deposits may have significant information on the temporal change of volcanic activity, there are few models for reconstruction. Aim of this study is to develop a theory on the transportation and sedimentation of pyroclasts to reconstruct the temporal variations of volcanic activity, especially the temporal variation of the GSD at the source position.

In part I, the author developed new models on the transportation and sedimentation processes in vertical one–dimensional region and in vertical and horizontal two-dimensional region. In Chapter 2, the author defined the basic theory on the evolution of GSD during the transportation and sedimentation processes. The author defined the GSD function and gave fundamental equations about the transportation during the fall process and the accumulation during the sedimentation process by using GSD function. In Chapter 3, the author developed one–dimensional models. The author formulated a fundamental equation in which GSDs are related between at the one–dimensional source position and at the sedimentation surface. By using the fundamental equations, the author developed models on the simple source conditions: the constant source (CS) model. This model is simple but is strongly helpful to decode physical information on a volcanic

activity. In Chapter 4, the author developed two–dimensional models. The author formulated an equation that describes GSD relationship between at the two–dimensional source position and at the sedimentation surface, which depends on the expansion style of ash cloud and downwind velocity. Furthermore, the author constrained on the grading structure of the pyroclastic fall deposit in the constant source (CS) model.

In Part Ⅱ, the author applied the established models to the 2011 Shinmoe–dake subplinian eruption. In Chapter 5, the author introduced overviews of the eruption and materials which we used. In Chapter 6, the author applied one–dimensional models to the eruption. As an application of the CS model, the author estimated the source duration and compared to observed eruption duration. As an application of the constant height (CH) model, the author converted the stratigraphic variation of GSDs in the pyroclastic fall deposit to the temporal variation of GSDs at the one–dimensional source. In Chapter 7, the author applied two–dimensional models to the eruption. As an application of the CS model, the author identified the cause of the reverse grading structure in the pyroclastic fall deposit. As an application of the CH model, the author converted the stratigraphic variation of GSDs in the pyroclastic fall deposit to the temporal variation of GSDs at the two–dimensional source. In Chapter 8, the author discussed the relationship among estimated temporal variation of GSDs at the two–dimensional source. Then the author discussed the advantages of our models and remaining problems. At the end of this article, the author mentioned future studies.

Part I

Development of models

Chapter 2

Basic theory

Definitions of the grain–size distribution (GSD) function

In order to describe temporal and spatial variation of the grain–size distribution (GSD) quantitatively, we define the grain–size distribution (GSD) function. The number of particles at (x, y, z) and time t with radius a in unit volume is defined as $f(a, x, y, z, t)$ no./(m$^3\cdot$ m) (Figs. 2.1 and 2.2). Total number of particles at (x, y, z) and time t with entire range of particle sizes in unit volume, $f_{tot}(x, y, z, t)$ no./m^3 is defined by the size integration of f (Fig. 2.2), then

$$f_{tot}(x, y, z, t) = \int_0^\infty f(a, x, y, z, t)\, da. \tag{2.1}$$

Similarly, the number of particles at (x, y) and time t with radius a in unit area is defined as $F(a, x, y, t)$ no./(m$^2\cdot$ m) corresponding to the spatial integration of f, then

$$F(a, x, y, t) = \int_0^\infty f(a, x, y, z, t)\, dz. \tag{2.2}$$

Total number of particles at (x, y) and time t with entire range of particle sizes in unit volume, $F_{tot}(x, y, t)$ no./m^2 is defined by the size integration of F, then

$$\begin{aligned} F_{tot}(x, y, t) &= \int_0^\infty F(a, x, y, t)\, da \\ &= \int_0^\infty \int_0^\infty f(a, x, y, z, t)\, dzda. \end{aligned} \tag{2.3}$$

GSD function is converted from the distribution of the number of particles to distributions of volume and mass of particles. If we give the volume of a particle with radius a

as $V^*(a)$ m^3/no., which only depends on the particle size, the distribution of the volume of particles at (x, y, z) and time t with a radius a in unit volume, $V(a, x, y, z, t)$ $\mathrm{m}^3/(\mathrm{m}^3 \cdot \mathrm{m})$ is

$$V(a, x, y, z, t) = f(a, x, y, z, t) \times V^*(a). \tag{2.4}$$

And if we give density of a particle with a radius a, $\rho_s(a)$ $\mathrm{kg/m}^3$, which only depends on the particle size, the mass of particles at (x, y, z) and time t with radius a in unit volume, $m(a, x, y, z, t)$ $\mathrm{kg}/(\mathrm{m}^3 \cdot \mathrm{m})$ is

$$\begin{aligned} m(a, x, y, z, t) &= V(a, x, y, z, t) \times \rho_s(a) \\ &= f(a, x, y, z, t) \times V^*(a) \times \rho_s(a). \end{aligned} \tag{2.5}$$

We focus on the GSD functions at the source height and the sedimentation surface. We identify the coordinates between at the source height $(x', y', z' = H(x', y', t'), t')$ and at the sedimentation surface $(x, y, z = h(x, y, t), t)$, where $H(x', y', t')$ m is the source height at (x', y') and time t', and $h(x, y, t)$ m is the thickness of the sediment at (x, y) and time t. We redefine the GSD at the source height (the source GSD) as f_{src} and the GSD at the sedimentation surface (the settling GSD) as f_{stl} (Fig. 2.3), then

$$f_{src}(a, x', y', t') = f(a, x', y', z' = H(x', y', t'), t'), \tag{2.6}$$

$$f_{stl}(a, x, y, t) = f(a, x, y, z = h(x, y, t), t). \tag{2.7}$$

The source GSD f_{src} and the sediment GSD f_{stl} are related by giving the settings of moving manner during the transportation of the particles.

Transportation of solid particles depends on the properties of the particles and surrounding gas, which has a highly variable. In case of the pyroclasts ejected by the volcanic eruption, properties of solid particle such as size and density depend on the mechanism of the magma fragmentation (e.g., Kaminski and Jaupart, 1998). Atmospheric properties are different depending on the location of the volcano, season, height, and time. It is difficult

to evaluate the transportation of the particles uniquely under the complex settings. To understand a pure effect of the simple transportation, we assume that the transportation of the particles during the fallout process is induced by the gravitational force and the advection owing to the wind. For the sake of simplicity, we don't consider the diffusion process to understand the pure size segregation effect during the transportation process depending on the particle size. We assume that the fall velocity of particles always reaches the terminal fall velocity (TFV) and has only vertical component, then the absolute value of the TFV is defined as v_t m/s. The TFV of a particle with a radius a can be estimated from fluid mechanics by

$$v_t = \left[\frac{8ga\left(\rho_s - \rho_l\right)}{3\rho_s C_d}\right], \tag{2.8}$$

where g is the acceleration due to the gravity, ρ_l is density of the surrounding atmosphere, and C_d is an experimentally determined drag coefficient (Kunii and Levenspiel, 1969). The particle Reynolds number Re is defined as

$$Re = \frac{2a\rho_l v_t}{\mu}, \tag{2.9}$$

where μ is the dynamic viscosity of the atmosphere (Kunii and Levenspiel, 1969). For spherical particles, the TFV can be determined by the relation between the drag coefficient C_d and the particle Reynolds number Re (Kunii and Levenspiel, 1969; Bonadonna and Phillips, 2003), then

$$C_d = \begin{cases} \frac{24}{Re} & \text{for } Re < 6, \\ \frac{10}{Re^{0.5}} & \text{for } 6 \leq Re < 500, \\ 0.43 & \text{for } 500 \leq Re < 200,000. \end{cases} \tag{2.10}$$

From Equations (2.8) to (2.10), the TFV is rewritten as

$$v_t = \begin{cases} \frac{2ga^2(\rho_s-\rho_l)}{9\mu} & \text{for } Re < 6, \\ 2a\left[\frac{4g^2(\rho_s-\rho_l)^2}{225\rho_l\mu}\right]^{\frac{1}{3}} & \text{for } 6 \leq Re < 500, \\ \left[\frac{6.2ga(\rho_s-\rho_l)}{\rho_l}\right]^{\frac{1}{2}} & \text{for } 500 \leq Re < 200,000. \end{cases} \tag{2.11}$$

We give constant density of particles ρ_s for the entire range of particle sizes, then the TFV depends on the particle size a, atmospheric conditions ρ_l and μ and the particle Reynolds number Re.

We define transportation distance in time Δt as Δx, Δy, and Δz for each axes. These values depend on the TFV of a particle and wind velocity. We give wind velocity $\boldsymbol{v}$, then

$$u\left(x,y,z,t\right) = \boldsymbol{v}\left(x,y,z,t\right)\hat{\boldsymbol{x}}, \tag{2.12}$$

$$v\left(x,y,z,t\right) = \boldsymbol{v}\left(x,y,z,t\right)\hat{\boldsymbol{y}}, \tag{2.13}$$

$$w\left(x,y,z,t\right) = \boldsymbol{v}\left(x,y,z,t\right)\hat{\boldsymbol{z}}, \tag{2.14}$$

where u, v, and w are components of the wind velocity in x–direction, y–direction, and z–direction, respectively, and $\hat{\boldsymbol{x}}$, $\hat{\boldsymbol{y}}$, and $\hat{\boldsymbol{z}}$ are unit vectors of x–coordinate, y–coordinate, and z–coordinate, respectively. The velocities of particles are

$$\frac{\Delta x\left(x,y,z,t\right)}{\Delta t} = u\left(x,y,z,t\right), \tag{2.15}$$

$$\frac{\Delta y\left(x,y,z,t\right)}{\Delta t} = v\left(x,y,z,t\right). \tag{2.16}$$

$$\frac{\Delta z\left(a,x,y,z,t\right)}{\Delta t} = w\left(x,y,z,t\right) - v_t\left(a,x,y,z,t\right). \tag{2.17}$$

As shown in Equations (2.15) to (2.17), the first term in the right hand side is advection term and the second term in the right hand side is fallout term. It is possible to formulate the relationship between the source GSD function f_{src} and the settling GSD function f_{stl} if we give settings of input parameters, such as a source height H and atmospheric conditions ρ_l, μ, and $\boldsymbol{v}$.

Descriptions of physical quantities

We define fluxes of falling particles with a radius a corresponding to the total amount of falling particles with a radius a through the test plane in unit time, then

$$\boldsymbol{j_n}\left(a,x,y,z,t\right) = f\left(a,x,y,z,t\right) \times \left\{\boldsymbol{v}\left(x,y,z,t\right) - v_t\left(a,x,y,z,t\right)\hat{\boldsymbol{z}}\right\}, \tag{2.18}$$

$$\boldsymbol{j_v}\left(a,x,y,z,t\right) \;=\; f\left(a,x,y,z,t\right) \times \left\{\boldsymbol{v}\left(x,y,z,t\right) - v_t\left(a,x,y,z,t\right)\hat{\boldsymbol{z}}\right\}$$

$$\times V^{*}(a), \tag{2.19}$$

$$\begin{aligned}\boldsymbol{j_m}(a,x,y,z,t) &= f(a,x,y,z,t)\times\{\boldsymbol{v}(x,y,z,t)-v_t(a,x,y,z,t)\,\hat{\boldsymbol{z}}\}\\ &\quad\times V^{*}(a)\times\rho_s(a),\end{aligned} \tag{2.20}$$

where $\boldsymbol{j_n}$, $\boldsymbol{j_v}$, and $\boldsymbol{j_m}$ are the number flux of falling particles with radius a, the volumetric flux of falling particles with radius a, and the mass flux of falling particles with radius a, respectively (Fig. 2.4). Similarly, fluxes of falling particles for the entire range of particle sizes corresponding to the total amount of the falling particle through the test plane in unit time for the entire range of particle sizes, then

$$\boldsymbol{J_n}(x,y,z,t)=\int_0^{\infty} f(a,x,y,z,t)\times\{\boldsymbol{v}(x,y,z,t)-v_t(a,x,y,z,t)\,\hat{\boldsymbol{z}}\}\,da, \tag{2.21}$$

$$\begin{aligned}\boldsymbol{J_v}(x,y,z,t) &= \int_0^{\infty} f(a,x,y,z,t)\times\{\boldsymbol{v}(x,y,z,t)-v_t(a,x,y,z,t)\,\hat{\boldsymbol{z}}\}\\ &\quad\times V^{*}(a)\,da,\end{aligned} \tag{2.22}$$

$$\begin{aligned}\boldsymbol{J_m}(x,y,z,t) &= \int_0^{\infty} f(a,x,y,z,t)\times\{\boldsymbol{v}(x,y,z,t)-v_t(a,x,y,z,t)\,\hat{\boldsymbol{z}}\}\\ &\quad\times V^{*}(a)\times\rho_s(a)\,da,\end{aligned} \tag{2.23}$$

where $\boldsymbol{J_n}$, $\boldsymbol{J_v}$, and $\boldsymbol{J_m}$ are the number flux of falling particles, the volumetric flux of falling particles, and the mass flux of falling particles, respectively (Fig. 2.4).

When particles arrive at the sedimentation surface with the height $h(x,y,t)$, the accumulation rate of the sediment dh/dt corresponds to the vertical volumetric component of the flux of falling particle (Fig. 2.5), then

$$\begin{aligned}\frac{dh(x,y,t)}{dt} &= \frac{-\boldsymbol{J_v}(x,y,z=h(x,y,t),t)\,\hat{\boldsymbol{z}}}{\varphi_{PF}(x,y,z=h(x,y,t),t)}\\ &= \frac{1}{\varphi_{PF}(x,y,z=h(x,y,t),t)}\\ &\quad\times\int_0^{\infty} f_{stl}(a,x,y,t)\\ &\quad\times\{w(x,y,z=h(x,y,t),t)-v_t(a,x,y,z=h(x,y,t),t)\}\end{aligned}$$

$$\times V^{*}(a)\, da, \tag{2.24}$$

where φ_{PF} is the volumetric fraction of particles in the sediment at (x, y) and time t corresponding to the packing fraction of the sediment.

Assumptions of models

To give an account of the temporal and the spatial variation of the GSD function, we give assumptions:

(a) There is no external supply and sink terms.

(b) Particle interactions such as break up and aggregation during the fallout process are negligible.

(c) Parameters of the surrounding atmosphere such as the dynamic viscosity, the density of the atmosphere, and wind velocity are homogeneous and constant during the entire processes.

(d) The vertical component of the wind velocity in Equation (2.14) is negligible.

(e) The coordinate of the ground surface corresponding to the height at the beginning of the sedimentation is given as $(x, y, z = 0)$.

Assumptions (a) and (b) imply that the number of particles is conserved through the fallout process. Assumptions (c) and (d) imply that the density of the surrounding atmosphere ρ_l, the dynamic viscosity of the atmosphere μ, and wind velocity $\boldsymbol{v}$ are the same at any coordinate in atmosphere, then TFV and wind velocities in Equations (2.11) to (2.14) are

$$v_t(a, x, y, z, t) = v_t(a), \tag{2.25}$$

$$\boldsymbol{v}(x, y, z, t)\, \hat{\boldsymbol{x}} = \bar{u} = \text{const.}, \tag{2.26}$$

$$\boldsymbol{v}(x, y, z, t)\, \hat{\boldsymbol{y}} = \bar{v} = \text{const.}, \tag{2.27}$$

$$\boldsymbol{v}\left(x,y,z,t\right)\hat{\boldsymbol{z}}=\bar{w}=0, \tag{2.28}$$

where $v_t\left(a\right)$ is a constant TFV through the fallout process which only depends on the particle size, and $\bar{u}$, $\bar{v}$, and $\bar{w}$ are components of the constant wind velocity in x–direction, y–direction, and z–direction, respectively.

In the above assumptions, it is possible to relate the departure time t' at the source height and the arrival time t at the sedimentation surface (Fig. 2.6), then

$$t=t'+t_a, \tag{2.29}$$

$$t_a=\frac{H\left(x',y',t'\right)-h\left(x,y,t\right)}{v_t\left(a\right)}, \tag{2.30}$$

where t_a is the fall time of particle with a radius a from the source height $H\left(x',y',t'\right)$ to the sedimentation surface $h\left(x,y,t\right)$. From Equations (2.15) to (2.17) and (2.25) to (2.30), coordinates between at the source height (x',y') and at the sedimentation surface (x,y) are related, then

$$x=x'+\bar{u}t_a, \tag{2.31}$$

$$y=y'+\bar{v}t_a. \tag{2.32}$$

For the sake of simplicity, we assume that the source height $H\left(x',y',t'\right)$ is much higher than the thickness of the thickness $h\left(x,y,t\right)$, then the fall time of particle with a radius a, t_a in Equation (2.30) is approximated as

$$t_a\left(a,x',y',t'\right)\approx\frac{H\left(x',y',t'\right)}{v_t\left(a\right)}, \tag{2.33}$$

then Equations (2.29), (2.31), and (2.32) are rewritten as

$$t=t'+\frac{H\left(x',y',t'\right)}{v_t\left(a\right)}, \tag{2.34}$$

$$x=x'+\bar{u}\frac{H\left(x',y',t'\right)}{v_t\left(a\right)}, \tag{2.35}$$

$$y = y' + \bar{v}\frac{H\left(x', y', t'\right)}{v_t\left(a\right)}. \tag{2.36}$$

The settling GSD function in Equation (2.7) is also approximated as

$$f_{stl}\left(a, x, y, t\right) \approx f\left(a, x, y, z = 0, t\right). \tag{2.37}$$

The quantitative relationship between the source GSD function $f_{src}\left(a, x', y', t'\right)$ and the settling GSD function $f_{stl}\left(a, x, y, t\right)$ is formulated by giving settings in each of the following chapters.

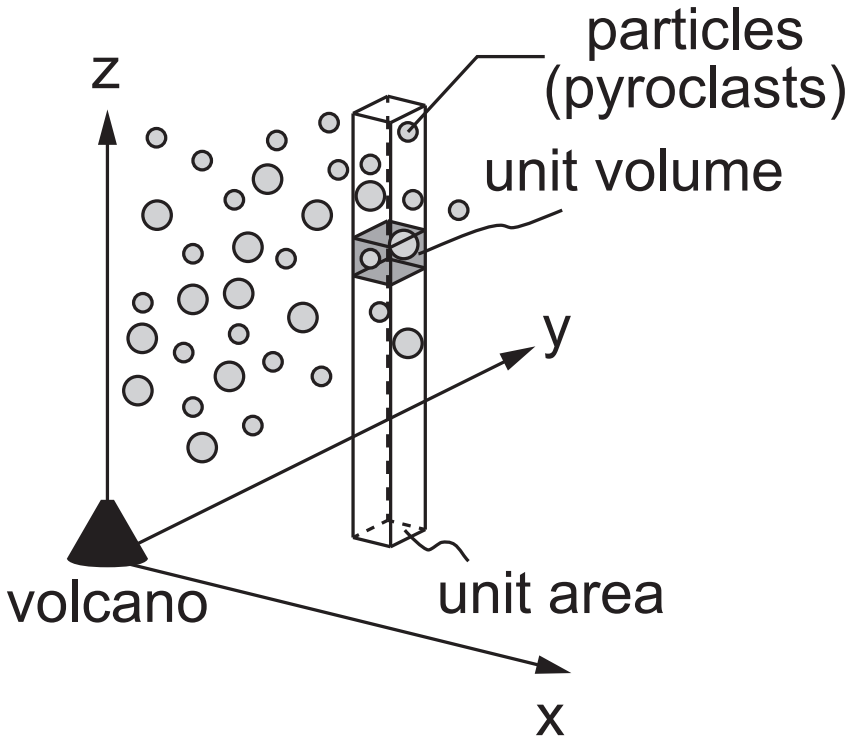

Figure 2.1: A schematic illustration of a coordinate system. We focus on the grain–size distributions (GSDs) in unit volume f and in unit area F.

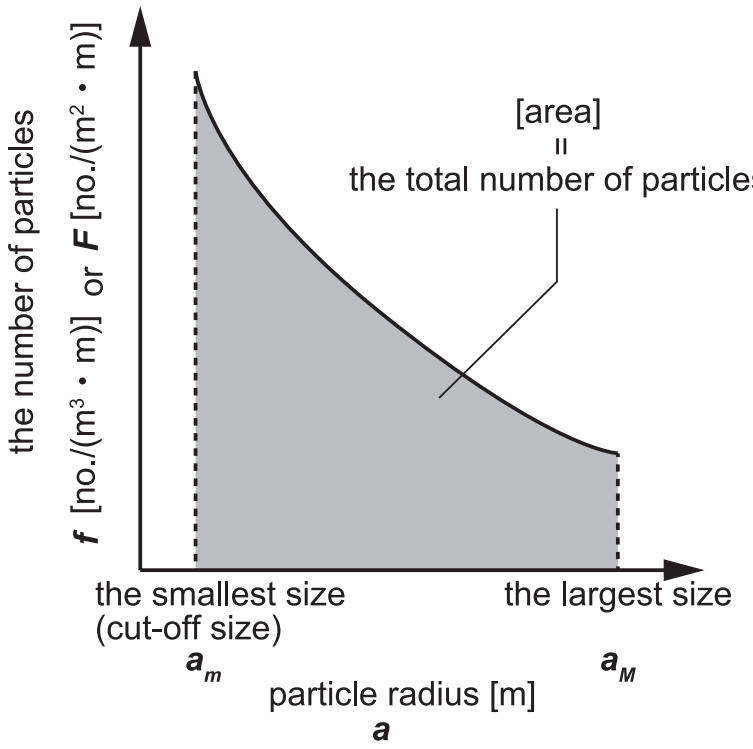

Figure 2.2: An example of the GSD plot. A GSD function is defined as the number of particles with a radius a in unit volume or in unit area. The total number of particles in unit volume or in unit area is given by size integration of the GSD function.

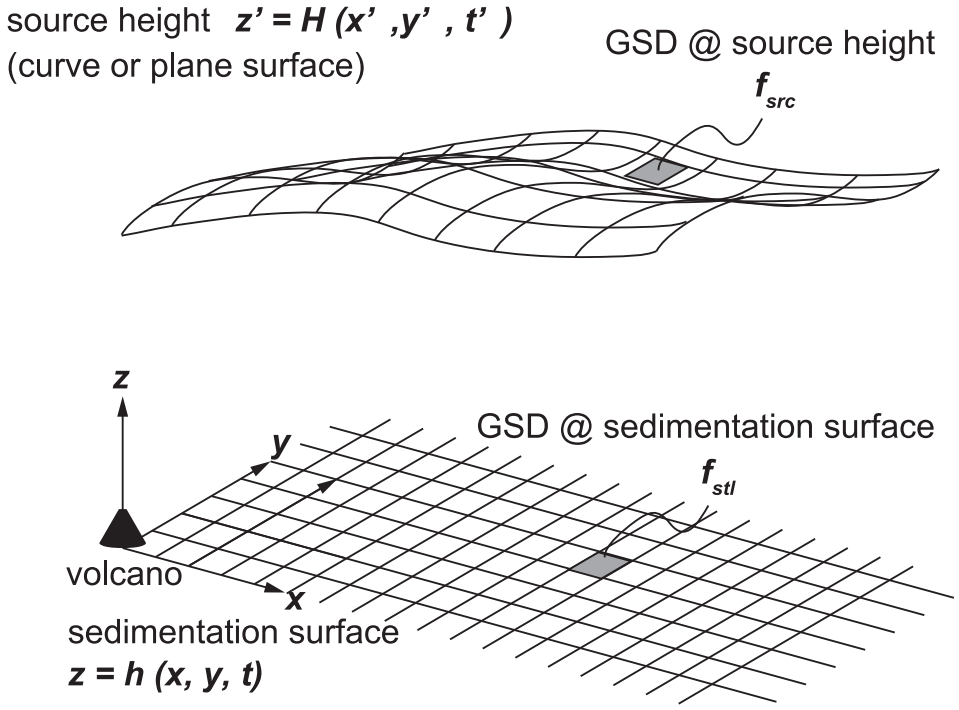

Figure 2.3: A schematic illustration of definitions on the source GSD function f_{src} and the settling GSD function f_{stl}. f_{stl} is related to f_{src} by giving the moving manner.

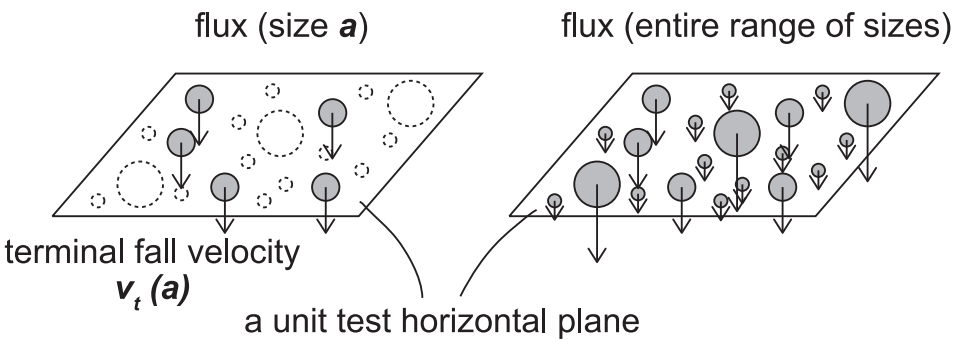

Figure 2.4: Schematic illustrations of fluxes of falling particles. A flux is defined as the amount of particles through the test plane in unit time.

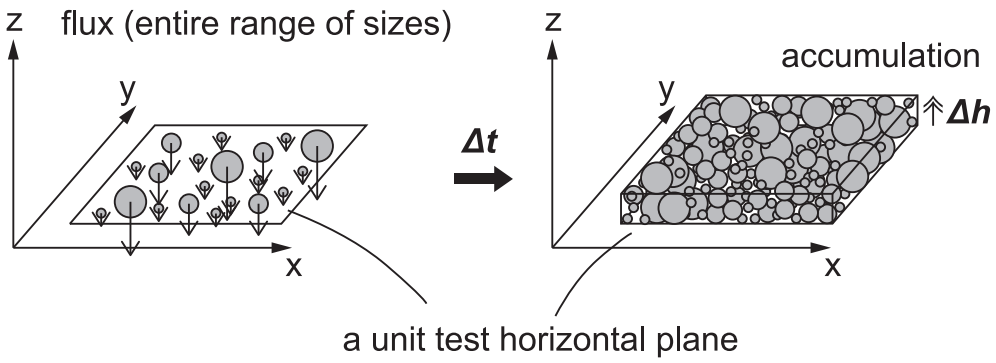

Figure 2.5: Schematic illustrations of the sedimentation process. Accumulation rate corresponds to the volumetric flux of the settling particles given by the settling GSD function.

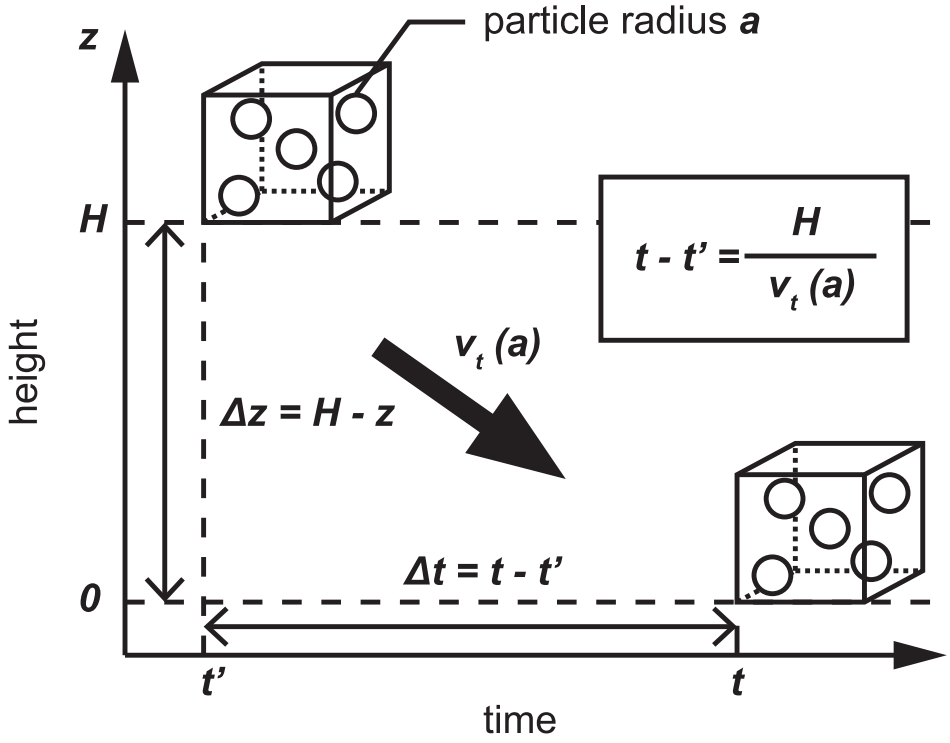

Figure 2.6: A schematic illustration of the time relationship. The relationship between the departure time at the source height, t' and the arrival time at the sedimentation surface, t is given by the terminal fall velocity of particles with a radius a.

Chapter 3

One–dimensional models

To figure out the fundamental descriptions in the transportation and sedimentation processes, we carried out the theoretical study in the vertical one–dimensional space. In this chapter, we focus on the size segregation effect during the fall process. The size segregation effect is induced by the difference of the TFV of particles (Fig. 3.1).

Definitions of the grain–size distribution (GSD) function in the one–dimensional model

In the one–dimensional model, GSD function is generally defined as $f(a, z, t)$. As shown in Equations (2.6) and (2.7), the source GSD function f_{src} and the settling GSD function f_{stl} in the one–dimensional descriptions are defined as

$$f_{src}(a, t') = f(a, z' = H(t'), t'), \tag{3.1}$$

$$f_{stl}(a, t) = f(a, z = h(t), t). \tag{3.2}$$

As shown in Equation (2.37), the settling GSD function f_{stl} is approximated as

$$f_{stl}(a, t) \approx f(a, z = 0, t). \tag{3.3}$$

The source height is defined as $H(t')$, and the height of the sedimentation surface at time t is defined as $h(t)$. As shown in Equation (2.33), the fall time from the source height with departure time t' to the sedimentation surface with the arrival time t with a radius a particles, t_a is

$$t_a(a, t') = \frac{H(t')}{v_t(a)}, \tag{3.4}$$

then the relationship between the departure time and the arrival time in Equation (2.34) is

$$\begin{aligned} t &= t' + t_a(a, t') \\ &= t' + \frac{H(t')}{v_t(a)}, \end{aligned} \tag{3.5}$$

Descriptions of physical quantities

In the one–dimensional models, fluxes of falling particles in Equations (2.18) to (2.20) are

$$j_n(a, z, t) = f(a, z, t) \times v_t(a), \tag{3.6}$$

$$j_v(a, z, t) = f(a, z, t) \times v_t(a) \times V^*(a), \tag{3.7}$$

$$j_m(a, z, t) = f(a, z, t) \times v_t(a) \times V^*(a) \times \rho_s(a), \tag{3.8}$$

where j_n, j_v, and j_m are absolute values of the number flux, the volumetric flux, and the mass flux of falling particles with a radius a, respectively. Similarly, fluxes in Equations (2.21) to (2.23) in one–dimensional models are

$$J_n(z, t) = \int_0^\infty f(a, z, t) \times v_t(a)\, da, \tag{3.9}$$

$$J_v(z, t) = \int_0^\infty f(a, z, t) \times v_t(a) \times V^*(a)\, da, \tag{3.10}$$

$$J_m(z, t) = \int_0^\infty f(a, z, t) \times v_t(a) \times V^*(a) \times \rho_s(a)\, da, \tag{3.11}$$

where J_n, J_v, and J_m are absolute values of vertical components of the number, the volumetric flux, and the mass flux of falling particles, respectively.

The accumulation rate of the sediment in Equation (2.24) is rewritten as

$$\frac{dh(t)}{dt} = \frac{1}{\varphi_{PF}(z = h(t), t)} J_v(z = h(t), t)$$

$$
\begin{aligned}
&\approx \quad \frac{1}{\varphi_{PF}\left(z=0,t\right)} J_v\left(z=0,t\right) \\
&= \quad \frac{1}{\varphi_{PF}\left(z=0,t\right)} \int_0^\infty f_{stl}\left(a,t\right) v_t\left(a\right) V^*\left(a\right) da. \qquad (3.12)
\end{aligned}
$$

In the following sections, we give settings of the supply to apply the theory to a practical sediment.

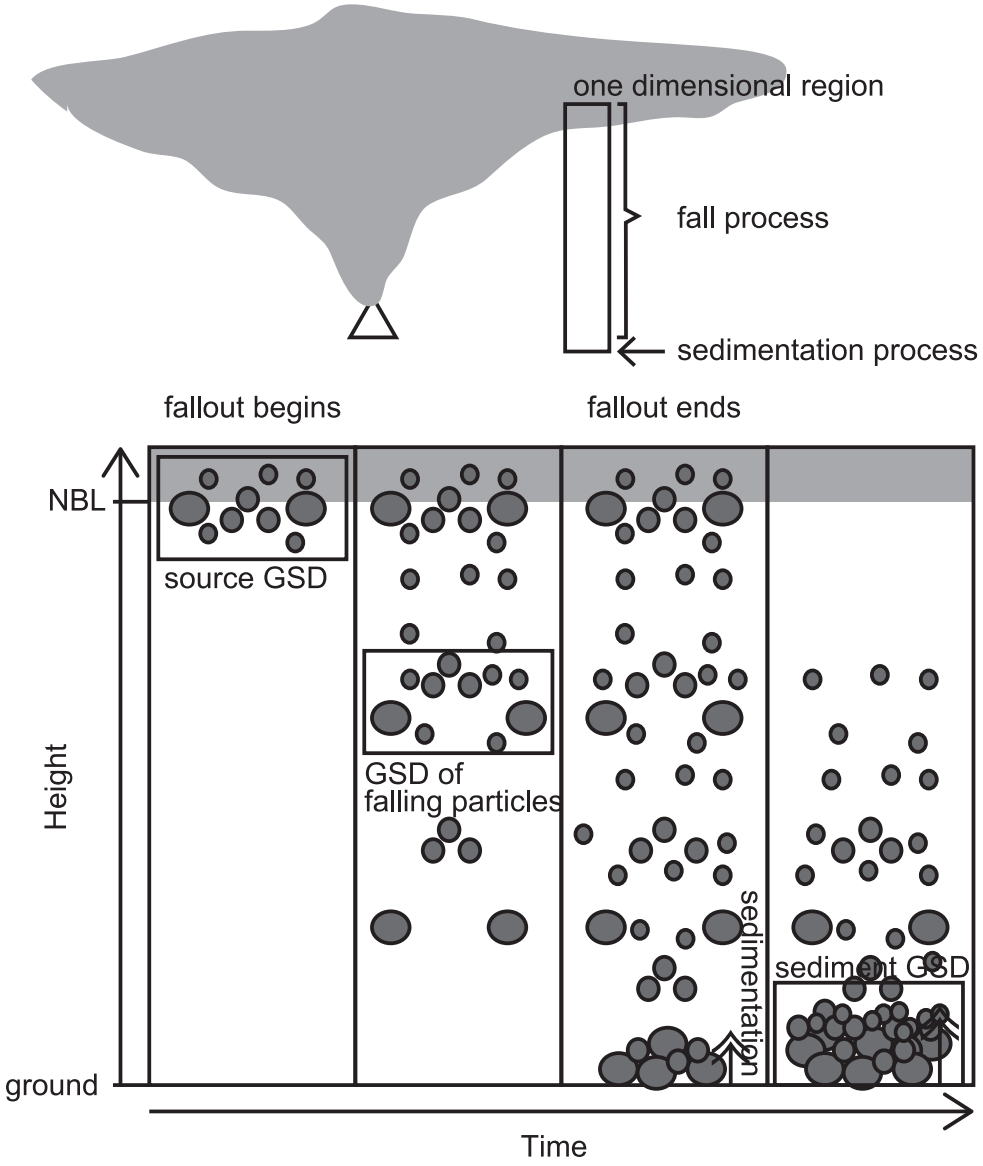

Figure 3.1: A schematic illustration of the vertical one–dimensional fall and sedimentation processes. In the vertical one–dimensional region, particles are supplied from the bottom of the ash cloud which is referred as the source. The GSD of the falling particles temporally varies owing to the size segregation effect induced by the difference of the terminal fall velocity. The temporal variation of the settling GSD is assumed as a function of the source GSD.

3.1 Conservation of the number

In this section, we formulate the relationship between the source GSD function f_{src} and the settling GSD function f_{stl} under the situation of the variable source GSD and the source height. We give the source GSD function $f_{src}(a, t')$ and the source height $H(t')$ as temporally variable values in the one–dimensional description. Conservation of the number is developed from two aspects satisfying a fundamental equation on the relationship between the departure time t' and the arrival time t in the one–dimensional transportation and sedimentation processes shown in Equation (3.5).

We first focus on the conservation of the number of particles with a radius a. The numbers of particles at the source position and at the sedimentation surface are related (Fig. 3.3), then

$$j_n(a, z = 0, t)\, dadt = j_n(a, z' = H(t'), t')\, dadt', \tag{3.13}$$

$$f_{stl}(a, t)\, v_t(a)\, dadt = f_{src}(a, t')\, v_t(a)\, dadt', \tag{3.14}$$

$$f_{stl}(a, t) = f_{src}(a, t') \left(\frac{\partial t'}{\partial t}\right)_a, \tag{3.15}$$

with

$$\left(\frac{\partial t'}{\partial t}\right)_a = \frac{1}{\left|1 + \frac{1}{v_t(a)} \frac{dH(t')}{dt'}\right|}. \tag{3.16}$$

Second, we focus on the conservation of the number of particles which settle at time t. The particles which settle at $z = 0$ and time t are a group of particles with a radius a which depart at $z = H(t')$ and time t' satisfying Equation (3.5) (Fig. 3.4). The GSD at the sedimentation surface is given as

$$f_{stl}(a, t) = \int_0^\infty f_{src}(a, t')\, \delta(G(t'))\, dt', \tag{3.17}$$

with

$$G(t') = t - t' - \frac{H(t')}{v_t(a)}, \tag{3.18}$$

where δ is delta function, and G is time relation function. The characteristic of the Dirac's delta function gives a solution of Equation (3.17), then

$$f_{stl}\left(a,t\right)=\sum_{i}\frac{f_{src}\left(a,\zeta_{i}\left(a,t\right)\right)}{\left|1+\frac{1}{v_{t}(a)}\frac{dH(\zeta_{i}(a,t))}{dt'}\right|}, \tag{3.19}$$

$$G\left(t'\right)=0 \quad \text{for } t'=\zeta_{i}\left(a,t\right), \tag{3.20}$$

where ζ is solution of the function $G\left(t'\right)=0$, and i indicates multiple solutions. Equation (3.19) implies that the settling GSD function f_{stl} can be converted to the source GSD function f_{src} by assuming the temporal variation of the source height H.

We develop models by giving the setting about the source height H in the followings.

Constant height (CH) case

When we give the constant source height (CH) case with time (Fig. 3.5), the time difference of the source height is

$$\frac{dH\left(t'\right)}{dt'}=0. \tag{3.21}$$

The differential relation between the departure time t' and the arrival time t is

$$\left(\frac{\partial t'}{\partial t}\right)_{a}=1. \tag{3.22}$$

Thus, Equation (3.19) is

$$f_{stl}\left(a,t\right)=f_{src}\left(a,t'\right). \tag{3.23}$$

Characteristics in the CH case is discussed in Chapter 3.2.

Linear height increase (LHI) case

When we give the source height which increases its height linearly (Fig. 3.6), then

$$H\left(t'\right)=H_{0}+bt', \tag{3.24}$$

$$\frac{H\left(t'\right)}{dt'}=b, \tag{3.25}$$

where H_0 is the initial source height and $b\,(>0)$ is an increase rate of the source height. The differential relation between the departure time t' and the arrival time t is

$$\left(\frac{\partial t'}{\partial t}\right)_a = \frac{1}{1+\frac{b}{v_t(a)}}. \tag{3.26}$$

Thus, Equation (3.19) is

$$f_{stl}\,(a,t) = f_{src}\,(a,t') \times \frac{1}{1+\frac{b}{v_t(a)}}. \tag{3.27}$$

Equation (3.27) suggests that the settling GSD function f_{stl} becomes dilute compared to the source GSD function f_{src} in the LHI case (Fig. 3.6).

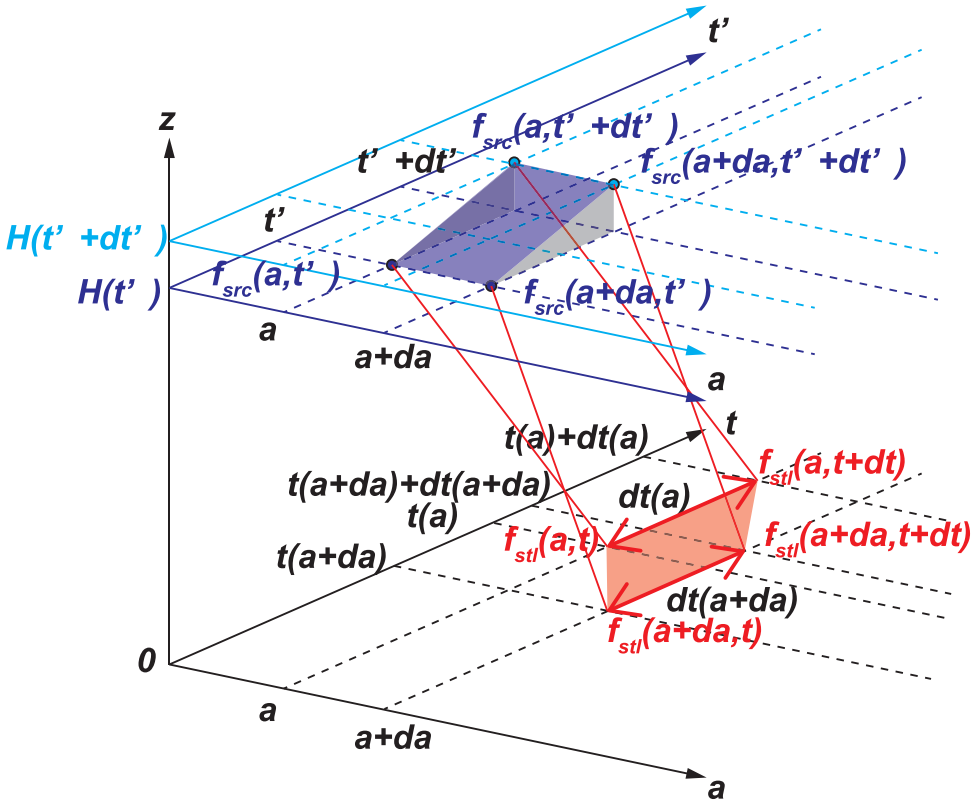

Figure 3.2: A schematic illustration of the conservation of the number in the settings of the unsteady source GSD f_{src} and the source height H. The flux at the source height colored with blue equals to that at the sedimentation surface colored with red.

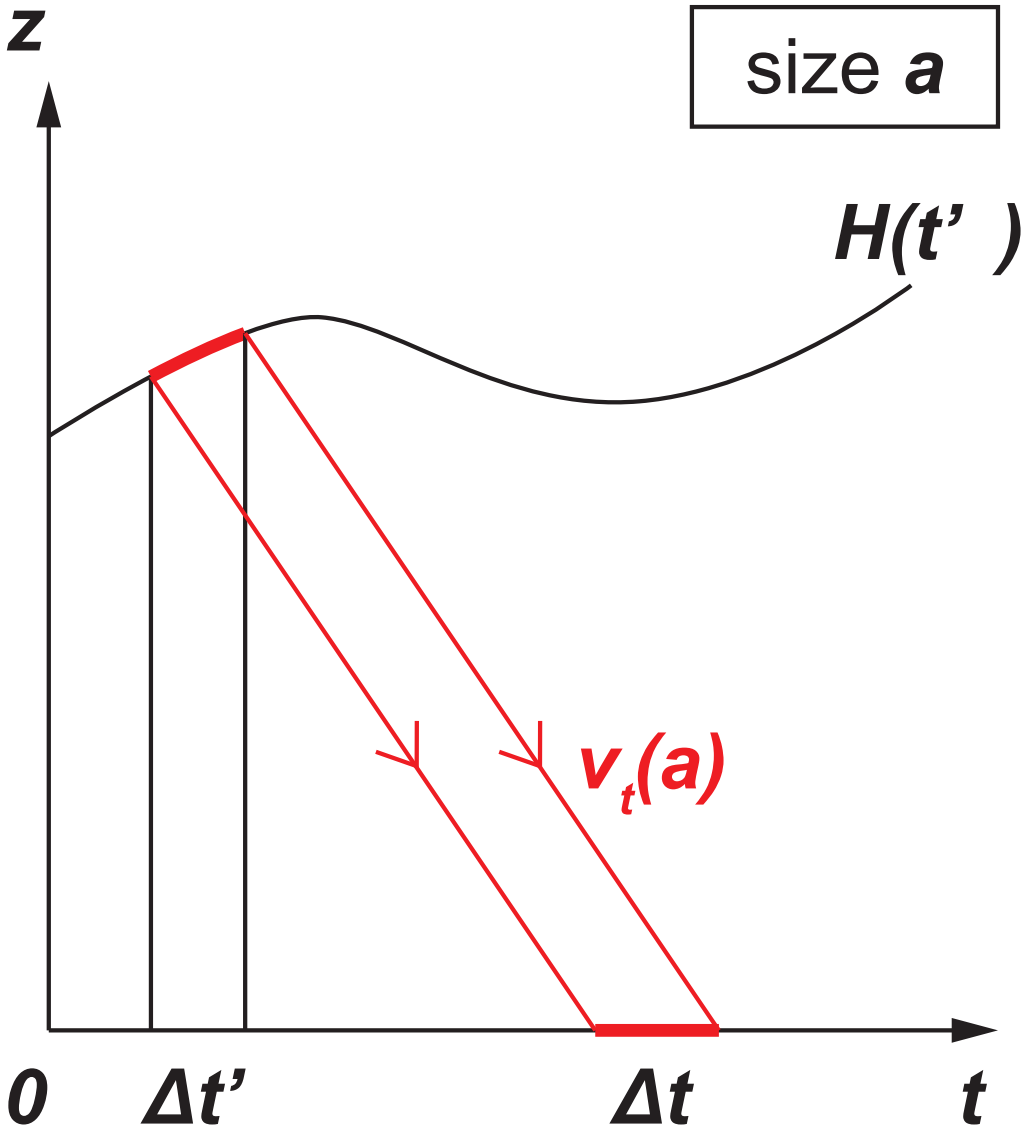

Figure 3.3: Cross-section surface of Figure (3.2) with a radius a. The number of particles with a radius a released at a height H within a duration $\Delta t'$ is conserved at the sedimentation surface within the duration Δt.

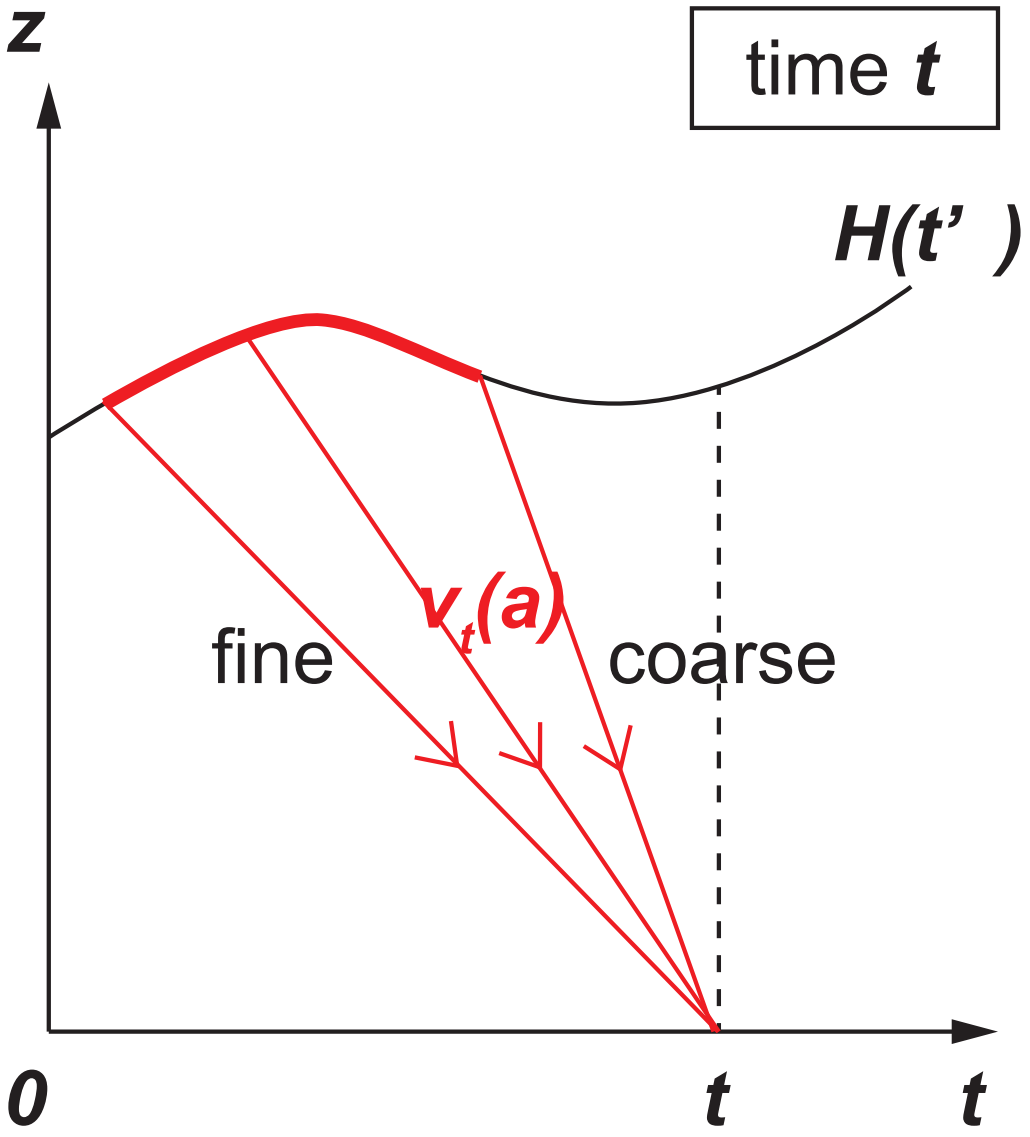

Figure 3.4: Cross-section surface of Figure (3.2) at time t. The departure time t' depends on the particle radius a restricted by Equation (3.5).

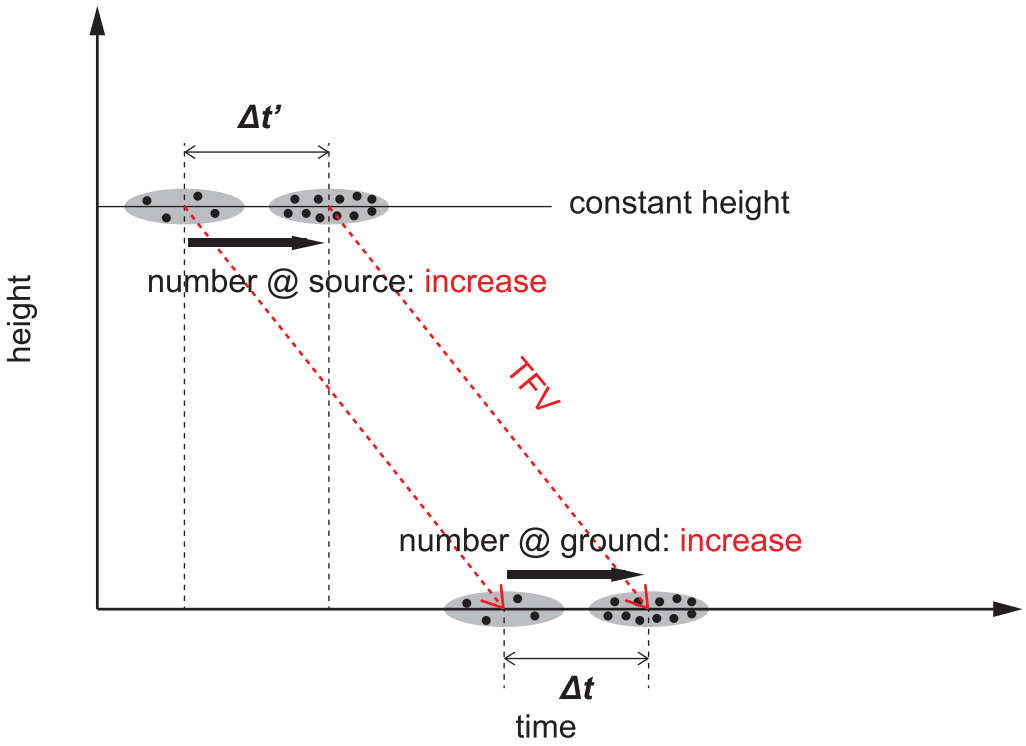

Figure 3.5: A schematic illustration of the constant height (CH) case. In the CH case, the time interval at the source height $\Delta t'$ equals to that at sedimentation surface Δt. Thus, the number of particles observed at the sedimentation surface corresponds to that supplied from the source height linearly.

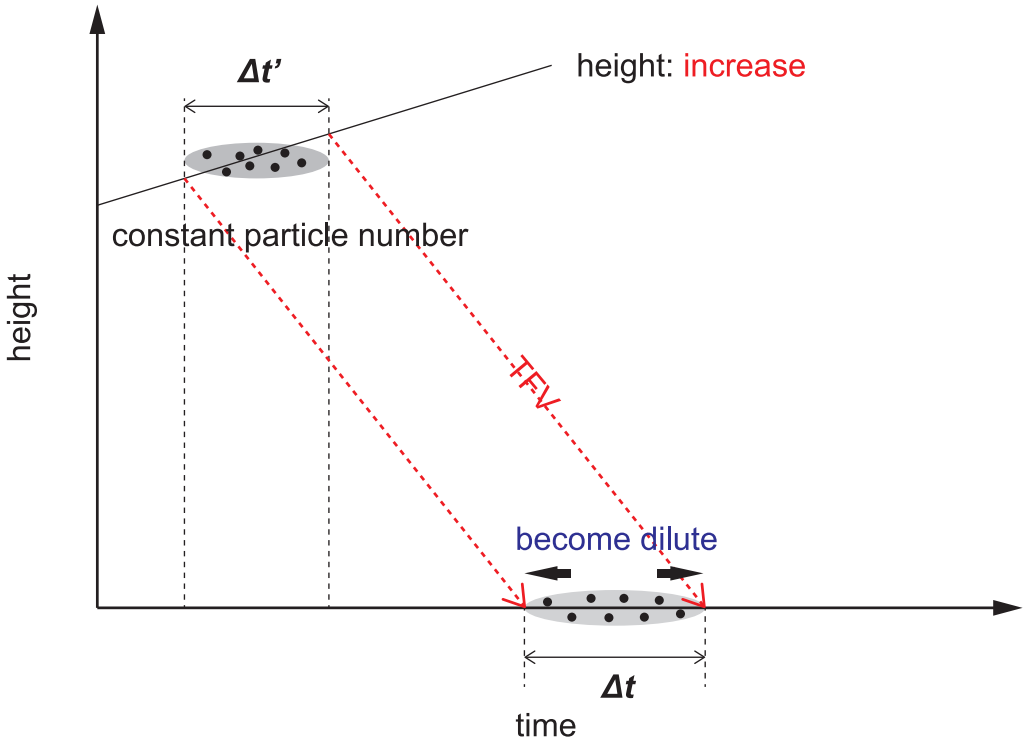

Figure 3.6: A schematic illustration of the linear height increase (LHI) case. The total number of particles is conserved between at the source height and at the sedimentation surface. In the LHI case, the number of particles observed at the sedimentation surface seems to become dilute relative to that at the source position owing to the increase of the source height.

3.2 Constant source (CS) model

Derivation

As a simple application of our theory, we consider the particle transportation in an idealistic eruption event in which the source GSD and the source height are constant during the source duration, t_{src} ($0 \leq t' \leq t_{src}$), which is referred as the CS model. In the CS model, the source GSD function can take finite non–zero values only during the source duration t_{src} (Fig. 3.7). The source GSD function f_{src} is expressed by rectangular function of time:

$$f_{src}(a, t') = f_{src}^{CS}(a) \times \sqcap(\tau'), \tag{3.28}$$

$$\tau' = \frac{t'}{t_{src}}, \tag{3.29}$$

$$\sqcap(\tau') = \begin{cases} 1 & \text{for } 0 \leq \tau' \leq 1, \\ 0 & \text{for } 1 < \tau', \end{cases} \tag{3.30}$$

where f_{src}^{CS} is the source GSD function in the CS model, τ' is dimensionless time scaled by the source duration, and $\sqcap$ is rectangular function. From Equations (3.23) and (3.28), the relationship of GSD functions between at the source position and at the sedimentation surface is given by

$$f_{stl}(a, t)\, da = f_{src}^{CS}(a) \times \sqcap\left(\frac{t - t_a}{t_{src}}\right) da. \tag{3.31}$$

Here, $f_{stl}(a, t)$ is non–zero for

$$t_a(a) \leq t \leq t_{src} + t_a(a), \tag{3.32}$$

otherwise $f_{stl}(a, t) = 0$, where $t_a(a)$ is given by Equation (3.31).

The maximum and the minimum sizes at the sedimentation surface, a_1 and a_2 is determined in the following (Fig. 3.7). If time t is less than the time at which the largest particle a_M released at the end of eruption reaches the ground, $t \leq t_M + t_{src}$, then the maximum size a_1 in the deposits equals the largest size a_M at the source, where

t_M is the travel time of the largest particle size with a radius a_M. On the contrary, if $t_M + t_{src} \leq t \leq t_m + t_{src}$, where t_m is the travel time of the smallest particle with a radius a_m, then the maximum size decreases with time, which is determined by the settling velocity $v_t(a)$ and available time $t - t_{src}$; that is, $t - t_{src} = H/v_t(a)$. The minimum size decreases with time because smaller sized particles reach the ground at a later time.

From Equation (2.11), we give simple TFV as power–law function of the particle size:

$$v_t(a) = ca^p, \tag{3.33}$$

where c and p are constants which are determined by the particle Reynolds number. Thus, we have

$$a_1(t) = \begin{cases} a_M & \text{for } t_M \leq t \leq t_M + t_{src}, \\ a_M \left(\frac{t_M}{t - t_{src}}\right)^{\frac{1}{p}} & \text{for } t_M + t_{src} \leq t \leq t_m + t_{src}, \end{cases} \tag{3.34}$$

$$a_2(t) = \begin{cases} a_M \left(\frac{t_M}{t}\right)^{\frac{1}{p}} & \text{for } t_M \leq t \leq t_m, \\ a_m & \text{for } t_m \leq t \leq t_m + t_{src}, \end{cases} \tag{3.35}$$

$$t_M = \frac{H}{v_t(a_M)}, \tag{3.36}$$

$$t_m = \frac{H}{v_t(a_m)}. \tag{3.37}$$

From Equation (3.10), the volume flux of settling particles is expressed by the CS case as

$$J_v(z = 0, t) = \frac{4}{3}\pi c \int_{a_2(t)}^{a_1(t)} a^{p+3} f_{src}^{CS}(a)\, da, \tag{3.38}$$

with the use of Equation (3.31). Equation (3.38) indicates that when f_{src}^{CS}, H, and t_{src} are given, the volume flux of settling particles is obtained. The dependence of $J_v(z = 0, t)$ on H and t_{src} are induced in a_1 and a_2 through Equations (3.34) to (3.35). The temporal variation of the sediment thickness is also calculated from Equations (3.12) and (3.38), then

$$\frac{dh(t)}{dt} = \frac{1}{\varphi_{PF}(t)} J_v(z = 0, t)$$

$$= \frac{4}{3}\pi c \frac{1}{\varphi_{PF}(t)} \int_{a_2(t)}^{a_1(t)} a^{p+3} f_{src}^{CS}(a)\, da, \tag{3.39}$$

$$\begin{aligned} h(t) &= \int_{t_M}^{t} \frac{dh(t)}{dt} dt \\ &= \int_{t_M}^{t} \frac{1}{\varphi_{PF}(t)} J_v(z=0,t)\, dt \\ &= \frac{4}{3}\pi c \int_{t_M}^{t} \frac{1}{\varphi_{PF}(t)} \int_{a_2(t)}^{a_1(t)} a^{p+3} f_{src}^{CS}(a)\, da dt. \end{aligned} \tag{3.40}$$

The case of the power–law source GSDs

GSDs of pyroclasts may by determined as a power–law distribution (Hartmann, 1969; Turcotte, 1968; Alibidirov and Dingwell, 1996; Kaminski and Jaupart, 1998; Kueppers et al., 2006):

$$f_{cum}(R \geq a) \propto a^{-D}, \tag{3.41}$$

where $f_{cum}(R \geq a)$ is the number of particles with a radius larger than a, R is a radius of particle larger than a , and D is the power–law exponent of the TGSD. The value of D in TGSD of pyroclasts is usually $3 \leq D \leq 4$ (Kaminski and Jaupart, 1998; Girault et al., 2014). As an application of the CS model, we formulate the case of the power–law distribution as the source GSD function:

$$\begin{aligned} f_{src}^{CS}(a) &= na^{-q} \\ &\propto \frac{\partial f_{cum}(R \geq a)}{\partial a}, \end{aligned} \tag{3.42}$$

where q (> 0) is the power–law exponent of the source GSD function corresponding to $q = D + 1$, and n is constant. The value of q in TGSD of pyroclasts is usually $4 \leq q \leq 5$ from the realistic D value. The size range of particles is given between the largest particle size a_M to the smallest particle size a_m. From Equations (3.39) and (3.42), the volume flux of settling particles is given by

$$J_v(z=0,t) = \frac{4}{3}\pi c n \int_{a_2(t)}^{a_1(t)} a^{p-q+3} da. \tag{3.43}$$

We give constant packing fraction, then

$$\varphi_{PF}(t) = \varphi_{PF} = \text{const.}, \tag{3.44}$$

$$\begin{aligned} \frac{dh(t)}{dt} &= \frac{1}{\varphi_{PF}} J_v(z=0,t) \\ &= \frac{4\pi cn}{3\varphi_{PF}} \int_{a_2(t)}^{a_1(t)} a^{p-q+3} da \\ &= \begin{cases} \frac{C}{A}\left[\{a_1(t)\}^A - \{a_2(t)\}^A\right] & \text{for } A \neq 0, \\ C \ln\left(\frac{a_1(t)}{a_2(t)}\right) & \text{for } A = 0, \end{cases} \end{aligned} \tag{3.45}$$

$$A \equiv p - q + 4, \tag{3.46}$$

$$B \equiv \frac{-q+4}{p}, \tag{3.47}$$

$$C \equiv \frac{4\pi cn}{3\varphi_{PF}}, \tag{3.48}$$

where constants A, B, and C are related to characteristics of the power–law source GSD function, TFV, the particle volume, and packing fraction. The accumulation rate is obtained depending on the time as follows:

I) $t_M + t_{src} \leq t_m$

1) $t_M \leq t \leq t_M + t_{src}$

$$\frac{dh(t)}{dt} = \begin{cases} \frac{C}{A} {a_M}^A \left[1 - \left(\frac{t_M}{t}\right)^{B+1}\right] & \text{for } A \neq 0, \\ \frac{C}{p} \ln\left(\frac{t}{t_M}\right) & \text{for } A = 0, \end{cases} \tag{3.49}$$

2) $t_M + t_{src} \leq t \leq t_m$

$$\frac{dh(t)}{dt} = \begin{cases} \frac{C}{A} {a_M}^A {t_M}^{B+1} \left[\left(\frac{1}{t-t_{src}}\right)^{B+1} - \left(\frac{1}{t}\right)^{B+1}\right] & \text{for } A \neq 0, \\ \frac{C}{p} \ln\left(\frac{t}{t-t_{src}}\right) & \text{for } A = 0, \end{cases} \tag{3.50}$$

3) $t_m \leq t \leq t_m + t_{src}$

$$\frac{dh(t)}{dt} = \begin{cases} \frac{C}{A} {a_M}^A \left[\left(\frac{1}{t-t_{src}}\right)^{B+1} - {\alpha_m}^A\right] & \text{for } A \neq 0, \\ \frac{C}{p} \ln\left[\frac{1}{{\alpha_m}^p}\left(\frac{t_M}{t-t_{src}}\right)\right] & \text{for } A = 0, \end{cases} \tag{3.51}$$

II) $t_m \leq t_M + t_{src}$

1) $t_M \leq t \leq t_m$

$$\frac{dh\,(t)}{dt} = \begin{cases} \frac{C}{A} {a_M}^A \left[1 - \left(\frac{t_M}{t}\right)^{B+1}\right] & \text{for } A \neq 0, \\ \frac{C}{p} \ln\left(\frac{t}{t_M}\right) & \text{for } A = 0, \end{cases} \tag{3.52}$$

2) $t_m \leq t \leq t_M + t_{src}$

$$\frac{dh\,(t)}{dt} = \begin{cases} \frac{C}{A} {a_M}^A \left(1 - {\alpha_m}^A\right) & \text{for } A \neq 0, \\ C \ln\left(\frac{1}{\alpha_m}\right) & \text{for } A = 0, \end{cases} \tag{3.53}$$

3) $t_M + t_{src} \leq t \leq t_m + t_{src}$

$$\frac{dh\,(t)}{dt} = \begin{cases} \frac{C}{A} {a_M}^A \left[\left(\frac{1}{t - t_{src}}\right)^{B+1} - {\alpha_m}^A\right] & \text{for } A \neq 0, \\ \frac{C}{p} \ln\left[\frac{1}{{\alpha_m}^p}\left(\frac{t_M}{t - t_{src}}\right)\right] & \text{for } A = 0, \end{cases} \tag{3.54}$$

$$\alpha_m = \frac{a_m}{a_M}, \tag{3.55}$$

where α_m is dimensionless size of the smallest particle scaled by the radius of the largest particle.

From Equations (3.34) to (3.37), (3.40), and (3.45) to (3.54), the total thickness of the sediment h_{tot} is given by

$$\begin{aligned} h_{tot} &= \int_{t_M}^{t_m + t_{src}} \frac{dh\,(t)}{dt} dt \\ &= \begin{cases} \frac{C}{A} {a_M}^A t_{src} \left(1 - {\alpha_m}^A\right) & \text{for } A \neq 0, B \neq 0, \\ C t_{src} \ln\left(\frac{1}{\alpha_m}\right) & \text{for } A = 0, \\ \frac{C}{p} {a_M}^p t_{src} \left(1 - {\alpha_m}^p\right) & \text{for } B = 0. \end{cases} \end{aligned} \tag{3.56}$$

Total thickness h_{tot} corresponds to the total amount of particles supplied at the source position $\int_0^{t_{src}} \int_{a_m}^{a_M} f_{src}^{CS}\,(a) \sqcap (\tau')\, v_t\,(a)\, V^*\,(a)\, da dt'$. The above result can be interpreted in terms of the volume fraction at the source, φ_{src} given by:

$$\begin{aligned} \varphi_{src} &= \int_{a_m}^{a_M} f_{src}^{CS}\,(a)\, V^*\,(a)\, da \\ &= \begin{cases} \frac{4\pi n}{3(-q+4)} a_M^{-q+4} \left(1 - {\alpha_m}^{-q+4}\right) & \text{for } q \neq 4, \\ \frac{4\pi n}{3} \ln\left(\frac{1}{\alpha_m}\right) & \text{for } q = 4. \end{cases} \end{aligned} \tag{3.57}$$

Thus, we have

$$h_{tot} = \phi_{src} h_{eff}, \tag{3.58}$$

$$h_{eff} = \begin{cases} v_t\left(a_M\right) t_{src} \frac{pB}{A\varphi_{PF}} \frac{1-{\alpha_m}^A}{1-{\alpha_m}^{pB}} & \text{for } A \neq 0, B \neq 0, \\ v_t\left(a_M\right) t_{src} \frac{pB}{\varphi_{PF}} \frac{1}{1-{\alpha_m}^{-p}} & \text{for } A = 0, \\ v_t\left(a_M\right) t_{src} \frac{1}{p\varphi_{PF}} \frac{1-{\alpha_m}^p}{\ln\left(\frac{1}{\alpha_m}\right)} & \text{for } B = 0, \end{cases} \tag{3.59}$$

where h_{eff} is the characteristic length which indicates the effective thickness of total supplied particles at the source position.

It should be noted that particles with size a can exist only within the limited stratigraphic interval represented by the settling time interval t given by Equation (3.32). The stratigraphic interval can be calculated from of Equation (3.45) for the time interval in which particles with a radius a settle on the transient sedimentation surface. The time interval begins from the time at which the first–released particles with size a reach the sedimentation surface, to the time at which particles released last with the size a reach the sedimentation surface. The former time t_a equals the travel time of the size a given by Equation (3.4). The latter time is given by $t_a + t_{src}$. Thus, the stratigraphic interval in which size a particles are present, h_a is given depending on the time relationship among t_M, t_a, t_m, and t_{src} as follows:

$$h_a = \int_{t_a}^{t_a + t_{src}} \frac{dh\left(t\right)}{dt} dt, \tag{3.60}$$

i) $t_M < t_M + t_{src} < t_a < t_a + t_{src} < t_m < t_m + t_{src}$

$$h_a = \begin{cases} \frac{C}{AB} {a_M}^A t_M \left\{ \left(\frac{t_M}{t_a + t_{src}}\right)^B + \left(\frac{t_M}{t_a - t_{src}}\right)^B - 2\left(\frac{t_M}{t_a}\right)^B \right\} & \text{for } A \neq 0, B \neq 0, \\ \frac{C}{p}\left[t_a \ln\left\{ 1 - \left(\frac{t_{src}}{t_a}\right)^2 \right\} + t_{src} \ln\left(\frac{t_a + t_{src}}{t_a - t_{src}}\right) \right] & \text{for } A = 0, \\ \frac{C}{p} {a_M}^p t_M \ln\left(\frac{{t_a}^2}{{t_a}^2 - {t_{src}}^2}\right) & \text{for } B = 0, \end{cases} \tag{3.61}$$

ii) $t_M < t_a < t_M + t_{src} < t_a + t_{src} < t_m < t_m + t_{src}$

$$h_a = \begin{cases} \frac{C}{A} {a_M}^A \left[(t_M + t_{src} - t_a) + \frac{t_M}{B}\left\{ 1 + \left(\frac{t_M}{t_a + t_{src}}\right)^B - 2\left(\frac{t_M}{t_a}\right)^B \right\} \right] & \text{for } A \neq 0, B \neq 0, \\ \frac{C}{p}\left[(t_a - t_M - t_{src}) + t_a \ln\left\{ \frac{t_M(t_a + t_{src})}{{t_a}^2} \right\} + t_{src} \ln\left(\frac{t_a + t_{src}}{t_M}\right) \right] & \text{for } A = 0, \\ \frac{C}{p}\left[(t_M + t_{src} - t_a) + t_a \ln\left\{ \frac{{t_a}^2}{t_M(t_a + t_{src})} \right\} \right] & \text{for } B = 0, \end{cases} \tag{3.62}$$

iii) $t_M < t_a < t_M + t_{src} < t_m < t_a + t_{src} < t_m + t_{src}$,

iv) $t_M < t_a < t_m < t_M + t_{src} < t_a + t_{src} < t_m + t_{src}$

$$h_a = \begin{cases} \dfrac{C}{A} {a_M}^A \left[t_{src} \left(1 - {\alpha_m}^A\right) + (t_M - t_a) + {\alpha_m}^A (t_m - t_a) \right. & \\ \quad \left. + \dfrac{t_M}{B} \left\{ 1 + \left(\dfrac{t_M}{t_m}\right)^B - 2\left(\dfrac{t_M}{t_a}\right)^B \right\} \right] & \text{for } A \neq 0, B \neq 0, \\ \dfrac{C}{p} \left[(t_{src} + t_a - t_m)\, p \ln\left(\dfrac{1}{\alpha_m}\right) + (2t_a - t_M - t_m) \right. & \\ \quad \left. + 2t_a \ln\left(\dfrac{t_M}{t_a}\right) + t_m \ln\left(\dfrac{t_m}{t_M}\right) \right] & \text{for } A = 0, \\ \dfrac{C}{p} {a_M}^p \left\{ t_{src} \left(1 - {\alpha_m}^p\right) + (t_M - t_a) + {\alpha_m}^p (t_m - t_a) \right. & \\ \quad \left. + t_M \ln\left(\dfrac{{t_a}^2}{t_m t_M}\right) \right\} & \text{for } B = 0, \end{cases} \tag{3.63}$$

v) $t_M < t_M + t_{src} < t_a < t_m < t_a + t_{src} < t_m + t_{src}$

$$h_a = \begin{cases} \dfrac{C}{A} {a_M}^A \left[{\alpha_m}^A (t_m - t_a - t_{src}) \right. & \\ \quad \left. + \dfrac{t_M}{B} \left\{ \left(\dfrac{t_M}{t_a - t_{src}}\right)^B + \left(\dfrac{t_M}{t_m}\right)^B - 2\left(\dfrac{t_M}{t_a}\right)^B \right\} \right] & \text{for } A \neq 0, B \neq 0, \\ \dfrac{C}{p} \left[(t_{src} + t_a - t_m)\, p \ln\left(\dfrac{1}{\alpha_m}\right) + (t_a + t_{src} - t_m) \right. & \\ \quad + t_a \ln\left\{ \dfrac{t_M (t_a - t_{src})}{{t_a}^2} \right\} + t_m \ln\left(\dfrac{t_m}{t_M}\right) & \text{for } A = 0, \\ \quad \left. + t_{src} \ln\left(\dfrac{t_M}{t_a - t_{src}}\right) \right] & \\ \dfrac{C}{p} {a_M}^p \left[{\alpha_c}^p (t_m - t_a - t_{src}) + t_M \ln\left\{ \dfrac{{t_a}^2}{t_m (t_a - t_{src})} \right\} \right] & \text{for } B = 0. \end{cases} \tag{3.64}$$

The thickness ratio of h_a to h_{tot} defined as γ_a is obtained as follows:

$$\gamma_a = \frac{h_a}{h_{tot}}, \tag{3.65}$$

i) $t_M < t_M + t_{src} < t_a < t_a + t_{src} < t_m < t_m + t_{src}$

$$\gamma_a = \begin{cases} \frac{{\varepsilon_0}^{B+1}}{B(1-{\alpha_m}^A)} \left\{ \left(\frac{1}{\varepsilon_a + 1}\right)^B + \left(\frac{1}{\varepsilon_a - 1}\right)^B - 2\left(\frac{1}{\varepsilon_a}\right)^B \right\} & \text{for } A \neq 0, B \neq 0, \\ \frac{1}{p ln\left(\frac{1}{\alpha_m}\right)} \left[\varepsilon_a \ln\left\{ 1 - \left(\frac{1}{\varepsilon_a}\right)^2 \right\} + \ln\left(\frac{\varepsilon_a + 1}{\varepsilon_a - 1}\right) \right] & \text{for } A = 0, \\ \frac{\varepsilon_0}{1 - {\alpha_m}^p} \ln\left(\frac{{\varepsilon_a}^2}{{\varepsilon_a}^2 - 1}\right) & \text{for } B = 0, \end{cases} \tag{3.66}$$

ii) $t_M < t_a < t_M + t_{src} < t_a + t_{src} < t_m < t_m + t_{src}$

$$\gamma_a = \begin{cases} \frac{1}{1-{\alpha_m}^A}\left[(1+\varepsilon_M-\varepsilon_a)\right. & \\ \qquad \left. +\frac{{\varepsilon_M}^{B+1}}{B}\left\{\left(\frac{1}{\varepsilon_M}\right)+\left(\frac{1}{\varepsilon_a+1}\right)^B-2\left(\frac{1}{\varepsilon_a}\right)^B\right\}\right] & \text{for } A\neq 0, B\neq 0, \\ \frac{1}{pln\left(\frac{1}{\alpha_m}\right)}\left[(\varepsilon_a-\varepsilon_M-1)+\varepsilon_a\ln\left\{\frac{\varepsilon_M(\varepsilon_a+1)}{{\varepsilon_a}^2}\right\}+\ln\left(\frac{\varepsilon_a+1}{\varepsilon_M}\right)\right] & \text{for } A=0, \\ \frac{1}{1-{\alpha_m}^p}\left[(1+\varepsilon_M-\varepsilon_a)+\varepsilon_a\ln\left\{\frac{{\varepsilon_a}^2}{\varepsilon_M(\varepsilon_a+1)}\right\}\right] & \text{for } B=0, \end{cases} \tag{3.67}$$

iii) $t_M < t_a < t_M + t_{src} < t_m < t_a + t_{src} < t_m + t_{src}$,

iv) $t_M < t_a < t_m < t_M + t_{src} < t_a + t_{src} < t_m + t_{src}$

$$\gamma_a = \begin{cases} 1+\frac{1}{1-{\alpha_m}^A}\left[(\varepsilon_M-\varepsilon_a)+{\alpha_m}^A(\varepsilon_m-\varepsilon_a)\right. & \\ \qquad \left. +\frac{{\varepsilon_M}^{B+1}}{B}\left\{\left(\frac{1}{\varepsilon_M}\right)^B+\left(\frac{1}{\varepsilon_m}\right)^B-2\left(\frac{1}{\varepsilon_a}\right)^B\right\}\right] & \text{for } A\neq 0, B\neq 0, \\ (1+\varepsilon_a-\varepsilon_m)+\frac{1}{pln\left(\frac{1}{\alpha_m}\right)}\left\{(2\varepsilon_a-\varepsilon_M-\varepsilon_m)\right. & \\ \qquad \left. +2\varepsilon_a\ln\left(\frac{\varepsilon_M}{\varepsilon_a}\right)+\varepsilon_m\ln\left(\frac{\varepsilon_m}{\varepsilon_M}\right)\right\} & \text{for } A=0, \\ 1+\frac{1}{1-{\alpha_m}^p}\left\{(\varepsilon_M-\varepsilon_a)+{\alpha_m}^p(\varepsilon_m-\varepsilon_a)+\varepsilon_M\ln\left(\frac{{\varepsilon_a}^2}{\varepsilon_m\varepsilon_M}\right)\right\} & \text{for } B=0, \end{cases} \tag{3.68}$$

v) $t_M < t_M + t_{src} < t_a < t_m < t_a + t_{src} < t_m + t_{src}$

$$\gamma_a = \begin{cases} \frac{1}{1-{\alpha_m}^A}\left[{\alpha_m}^A(\varepsilon_m-\varepsilon_a-1)\right. & \\ \qquad \left. +\frac{{\varepsilon_M}^{B+1}}{B}\left\{\left(\frac{1}{\varepsilon_a-1}\right)^B+\left(\frac{1}{\varepsilon_m}\right)^B-2\left(\frac{1}{\varepsilon_a}\right)^B\right\}\right] & \text{for } A\neq 0, B\neq 0, \\ (1-+\varepsilon_a\varepsilon_m)+\frac{1}{pln\left(\frac{1}{\alpha_m}\right)}\left[(1+\varepsilon_a-\varepsilon_m)\right. & \\ \qquad \left. +\varepsilon_a\ln\left\{\frac{\varepsilon_M(\varepsilon_a-1)}{{\varepsilon_a}^2}\right\}+\varepsilon_m\ln\left(\frac{\varepsilon_m}{\varepsilon_M}\right)+\ln\left(\frac{\varepsilon_M}{\varepsilon_a-1}\right)\right] & \text{for } A=0, \\ \frac{1}{1-{\alpha_m}^p}\left[{\alpha_m}^p(\varepsilon_m-\varepsilon_a-1)+\varepsilon_M\ln\left\{\frac{{\varepsilon_a}^2}{\varepsilon_m(\varepsilon_a-1)}\right\}\right] & \text{for } B=0, \end{cases} \tag{3.69}$$

$$\varepsilon_M \equiv \frac{t_M}{t_{src}}, \tag{3.70}$$

$$\varepsilon_a \equiv \frac{t_a}{t_{src}}, \tag{3.71}$$

$$\varepsilon_m \equiv \frac{t_m}{t_{src}}, \tag{3.72}$$

where dimensionless parameters ε_M, ε_a, and ε_m which include the source parameters (H and t_{src}) and TFV of specific particle size are the time scales of the travel times for the particles with largest size a_M and arbitrary size a normalized by the source duration t_{src}, respectively.

The stratigraphic interval in which particles with size a_M exist, h_M is given by

$$h_M = \int_{t_M}^{t_M+t_{src}} \frac{dh\,(t)}{dt} dt. \tag{3.73}$$

It can be applied the results of Equations (3.62) and (3.63) corresponding to $t_a \leq t_M + t_{src}$, then

I) $t_M + t_{src} \leq t_c$

$$h_M = \begin{cases} \frac{C}{A} {a_M}^A \left[t_{src} + \frac{t_M}{B} \left\{ \left(\frac{t_M}{t_M + t_{src}} \right)^B - 1 \right\} \right] & \text{for } A \neq 0, \\ \frac{C}{p} \left\{ -t_{src} + (t_M + t_{src}) \ln \left(1 + \frac{t_{src}}{t_M} \right) \right\} & \text{for } A = 0, \\ \frac{C}{p} {a_M}^p \left\{ t_{src} + t_M \ln \left(\frac{t_M}{t_M + t_{src}} \right) \right\} & \text{for } B = 0, \end{cases} \tag{3.74}$$

II) $t_m \leq t_M + t_{src}$

$$h_M = \begin{cases} \frac{C}{A} {a_M}^A \left[t_{src} \left(1 - {\alpha_m}^A \right) + {\alpha_m}^A \left(t_m - t_M \right) \right. & \\ \qquad \left. + \frac{t_M}{B} \left\{ \left(\frac{t_M}{t_m} \right)^B - 1 \right\} \right] & \text{for } A \neq 0, \\ \frac{C}{p} \left\{ \left(t_{src} + t_M - t_m \right) p \ln \left(\frac{1}{\alpha_m} \right) + \left(t_M - t_m \right) + t_m \ln \left(\frac{t_m}{t_M} \right) \right\} & \text{for } A = 0, \\ \frac{C}{p} {a_M}^p \left\{ t_{src} \left(1 - {\alpha_m}^p \right) + {\alpha_m}^p \left(t_m - t_M \right) + t_M \ln \left(\frac{t_M}{t_m} \right) \right\} & \text{for } B = 0, \end{cases} \tag{3.75}$$

The thickness ratio of h_M to h_{tot} defined as γ_M is given by

$$\gamma_M = \frac{h_M}{h_{tot}}, \tag{3.76}$$

I) $t_M + t_{src} \leq t_m$

$$\gamma_M = \begin{cases} \frac{1}{1 - {\alpha_m}^A} \left[1 + \frac{\varepsilon_M}{B} \left\{ \left(\frac{\varepsilon_M}{\varepsilon_M + 1} \right)^B - 1 \right\} \right] & \text{for } A \neq 0, \\ \frac{1}{p \ln \left(\frac{1}{\alpha_m} \right)} \left\{ -1 + (1 + \varepsilon_M) \ln \left(1 + \frac{1}{\varepsilon_M} \right) \right\} & \text{for } A = 0, \\ \frac{1}{1 - {\alpha_m}^p} \left\{ 1 + \varepsilon_M \ln \left(\frac{\varepsilon_M}{\varepsilon_M + 1} \right) \right\} & \text{for } B = 0, \end{cases} \tag{3.77}$$

II) $t_m \leq t_M + t_{src}$

$$\gamma_M = \begin{cases} 1 + \frac{1}{1-{\alpha_m}^A}\left[{\alpha_m}^A(\varepsilon_m - \varepsilon_M) + \frac{\varepsilon_M}{B}\left\{\left(\frac{\varepsilon_M}{\varepsilon_m}\right)^B - 1\right\}\right] & \text{for } A \neq 0, \\ (1 + \varepsilon_M - \varepsilon_m) + \frac{1}{p\ln\left(\frac{1}{\alpha_m}\right)}\left\{(\varepsilon_M - \varepsilon_m) + \varepsilon_m \ln\left(\frac{\varepsilon_m}{\varepsilon_M}\right)\right\} & \text{for } A = 0, \\ 1 + \frac{1}{1-{\alpha_m}^p}\left\{{\alpha_m}^p(\varepsilon_m - \varepsilon_M) + \varepsilon_M \ln\left(\frac{\varepsilon_M}{\varepsilon_m}\right)\right\} & \text{for } B = 0. \end{cases} \tag{3.78}$$

It is possible to approximate $a_m = 0$ when the case $A > 0$ and $t_a + t_{src} \leq t_m$, then

$$h_{tot} = \frac{C}{A}{a_M}^A t_{src} \quad \text{for } A > 0, a_m = 0, \tag{3.79}$$

$$h_a = \begin{cases} \frac{C}{A}a_M^A\left[(t_{src} + t_M - t_a)\right. \\ \quad \left. + \frac{t_M}{B}\left\{1 + \left(\frac{t_M}{t_{src}+t_a}\right)^B - 2\left(\frac{t_M}{t_a}\right)^B\right\}\right] & \text{for } A > 0, t_a \leq t_M + t_{src}, \\ \frac{C}{AB}a_M^A t_M\left\{\left(\frac{t_M}{t_{src}+t_a}\right)^B - \left(\frac{t_M}{t_{src}-t_a}\right)^B - 2\left(\frac{t_M}{t_a}\right)^B\right\} & \text{for } A > 0, t_a \geq t_M + t_{src}, \end{cases} \tag{3.80}$$

$$\gamma_a = \begin{cases} 1 + \varepsilon_M - \varepsilon_a + \frac{\varepsilon_M}{B}\left\{1 - 2\left(\frac{\varepsilon_M}{\varepsilon_a}\right)^B + \left(\frac{\varepsilon_M}{1+\varepsilon_a}\right)^B\right\} & \text{for } A > 0, t_a \leq t_M + t_{src}, \\ \frac{\varepsilon_M^{B+1}}{B}\left\{\left(\frac{1}{1+\varepsilon_a}\right)^B - \left(\frac{1}{1-\varepsilon_a}\right)^B - 2\left(\frac{1}{\varepsilon_a}\right)^B\right\} & \text{for } A > 0, t_a \geq t_M + t_{src}, \end{cases} \tag{3.81}$$

$$h_M = \frac{C}{A}{a_M}^A\left[t_{src} + \frac{t_M}{B}\left\{\left(\frac{t_M}{t_M + t_{src}}\right)^B - 1\right\}\right] \quad \text{for } A > 0, a_m = 0. \tag{3.82}$$

The characteristic ratio γ_M can be defined as the ratio of the thickness where the largest particle size are present, h_M, to the total thickness of the sediment h_{tot} as follows:

$$\gamma_M = 1 + \frac{\varepsilon_M}{B}\left(\frac{\varepsilon_M}{1+\varepsilon_M} - 1\right)^B \quad \text{for } A > 0, a_m = 0. \tag{3.83}$$

That is, the value of $1 - \gamma_M$ represents the thickness of the layer in which the largest particles are absent to the total thickness. Figure 3.8 shows γ_M as a function of power–law exponent q of the source GSD for $p = 2$ (Stokes sedimentation) and ε_M. This suggests that the time scale ratio ε_M can be estimated from the observation for the thickness ratio γ_M and the power–law exponent q from the grain–size analysis for the pyroclastic fall deposits.

Figure 3.8 illustrated the effects of q and ε_M on γ_M to determine the correlations among γ_M, q and ε_M. The power–law exponent q in the source GSD is a measure of the abundance of coarser particles in all particles, whereas the thickness h_M indicates the fraction of coarser particles. Thus, for large q value, which corresponds to a steep slope in GSD plot, coarse–poor particles create a relatively thin h_M thickness, leading to a small γ_M value. γ_M is positively correlated with q for a given ε_M.

On the other hand, ε_M and γ_M exhibit a negative correlation. Large ε_M values implies large t_M values (or correspond to large H values, small $v_t\,(a_M)$ (or small a_M) values), or small t_{src} values. As shown in Equation (3.32), the dimensionless parameter ε_M relates to the duration corresponding to the formation of the h_M sediment. Large values of ε_M corresponds to small values of the duration corresponding to the formation of the interval of the thickness h_M relatively, which results in a decrease in γ_M values.

Extension of the CS Model: Numerical Approach

Here, we extend the CS model to more realistic settling velocities, in which TFV depends on the particle Reynolds number Re as a function of particle radius and atmospheric conditions surrounding particles (density and viscosity) as follows:

$$p = \begin{cases} 2 & \text{for } Re < 6, \\ 1 & \text{for } 6 \leq Re < 500, \\ 0.5 & \text{for } 500 \leq Re < 200,000, \end{cases} \tag{3.84}$$

$$c = \begin{cases} \frac{2g(\rho_p - \rho_a)}{9\mu} & \text{for } Re < 6, \\ 2\left[\frac{4g^2(\rho_p - \rho_a)^2}{225\rho_a\mu}\right]^{\frac{1}{3}} & \text{for } 6 \leq Re < 500, \\ \left[\frac{6.2g(\rho_p - \rho_a)}{\rho_a}\right]^{\frac{1}{2}} & \text{for } 500 \leq Re < 200,000. \end{cases} \tag{3.85}$$

Figure 3.10 shows the results of calculations when constants c are given as 2.3×10^8 for $Re < 6$, 1.3×10^4 for $6 \leq Re < 500$, and 3.0×10^2 for $500 \leq Re < 200,000$, assuming atmospheric conditions at sea level (Bonadonna and Phillips, 2003; Folch, 2012; Fig. 3.9). In calculation, we give the smallest particle size $a_m = 10 \times 10^{-6}$ m as the cut–off particle size.

As shown in Figure 3.10, the behavior of γ_M as a function of q with the parameter ε_M in numerical result is essentially similar to the simplified analytical result with a use of a single TFV trend with $p = 2$ and $a_m = 0$. As shown in Equation (3.83), in cases of analytical results, terms corresponding to the largest particle size a_M are included in the parameter ε_M. On the contrary, in cases of numerical results, additional terms correspond to the given largest particle size a_M in the calculation, which gives different γ_M values even if the ε_M values are the same.Small a_M values show similar γ_M values to analytical results because of the use of a single TFV trend in calculation. However, values are different here owing to the cut–off effect of the smallest particle in calculation (Fig. 3.10).

In cases of numerical results, for a given q value, the γ_M value decreases with an increase in the largest particle size a_M. When the largest particle size a_M increases, the slope TFV trend of coarser particles becomes more gradual than finer particles owing to the particle Reynolds number, which decreases the size range composing the interval of the thickness h_M. Decreasing the size range in h_M results in the decrease in the γ_M value.

Quantitative relations among γ_M, q, and ε_M are used to estimate one of unknown parameters from other observed values. Details of the application methods are described in the following section.

An application to the virtual pyroclastic fall deposit: Estimation of the source duration

In this section, we illustrate the application of the CS model results to GSD data of deposits by using a virtual example. By giving hypothetical data which is obtained from geological survey (a_M, q, and γ_M), we explain the application process of the CS model to the estimations of the unknown parameter ε_M and the source duration t_{src}. Actual methods for obtaining geological data and an example of the practical application are described in Part Ⅱ.

Let us suppose that we have $a_M = 1.0 \times 10^{-2}$ m and $q = 4.5$ as geological data in the entire sediment GSD at a certain sampling locality. In addition, we have a γ_M

value, which was also obtained by geological survey. To obtain the γ_M value, we first need to measure the disappearance point h_M of the largest particles a_M by analyzing the stratigraphic variation of maximum pumice (MP) a_1 (Fig. 3.7). Then we calculate the thickness ratio $\gamma_M = h_M/h_{tot}$ from these observed data. As a virtual example, we give $\gamma_M = 0.5$.

By using these values of the pyroclastic fall deposit ($a_M = 1.0 \times 10^{-2}$, $q = 4.5$, and $\gamma_M = 0.5$), we can estimate the value of ε_M as approximately 0.2 (Fig. 3.11) when the TFV constants c in Equation (3.85) are given as 2.3×10^8 for $Re < 6$, 1.3×10^4 for $6 \leq Re < 500$, and 3.0×10^2 for $500 \leq Re < 200,000$, which are given as atmospheric constants at sea level. Giving the eruption column height estimated by using the method of Carey and Sparks (1986), which we regarded as the source height H in our CS model, we calculate the settling time for the largest particle, t_M, and estimated the source duration $t_{src} = t_M/\varepsilon_M$ in Equation (3.70). If we give the value of the source height H as 10^4 m, then the source duration t_{src} is estimated as 1.6×10^3 s from the value of $\varepsilon_M \approx 0.2$ as shown in Figure 3.11.

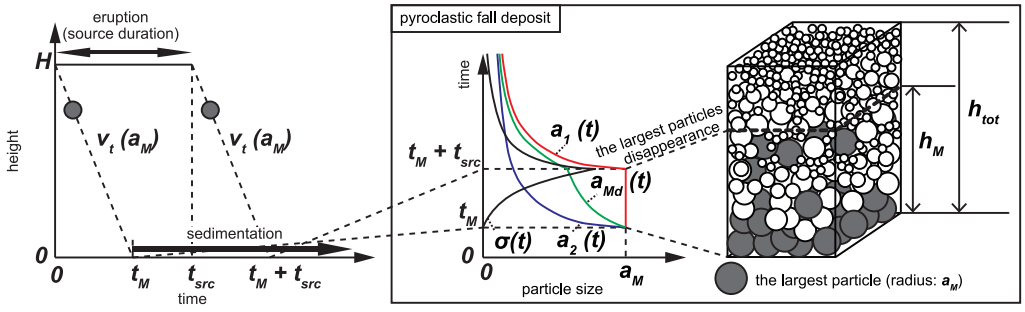

Figure 3.7: A schematic illustration of the constant source (CS) model. Particles are supplied during eruption from height H. The duration of the particle supply is t_{src}. The sedimentation process begins from the first arrival of the largest particles with size a_M. The t_M is the travel time of the largest particle from the source height to the ground. The time interval in which particles with size a_M exist is from t_M to $t_M + t_{src}$. *Red line*: Maximum particle size, *Blue line*: Minimum particle size, *Green line*: Median particle size, *Black line*: Sorting parameter.

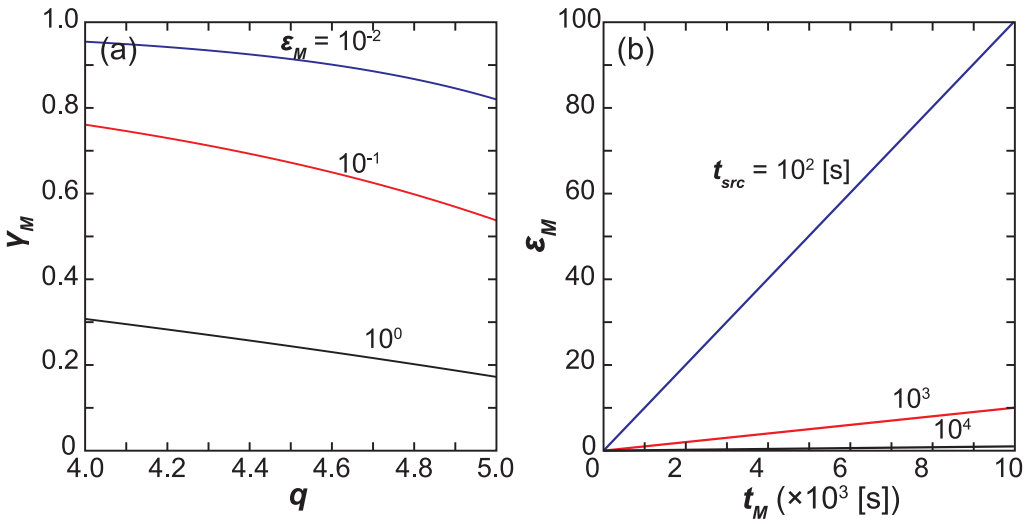

Figure 3.8: (a) Analytical results of the relationship between the power law exponent of the source GSD q and the thickness ratio of the largest particles existing layer to the total thickness, γ_M. The ε_M is the dimensionless parameter defined by t_M/t_{src}. *Blue lines*: $\varepsilon_M = 10^{-2}$, *Red lines*: $\varepsilon_M = 10^{-1}$, *Black lines*: $\varepsilon_M = 10^{0}$. (b) Plots of t_M and t_{src} related by ε_M.

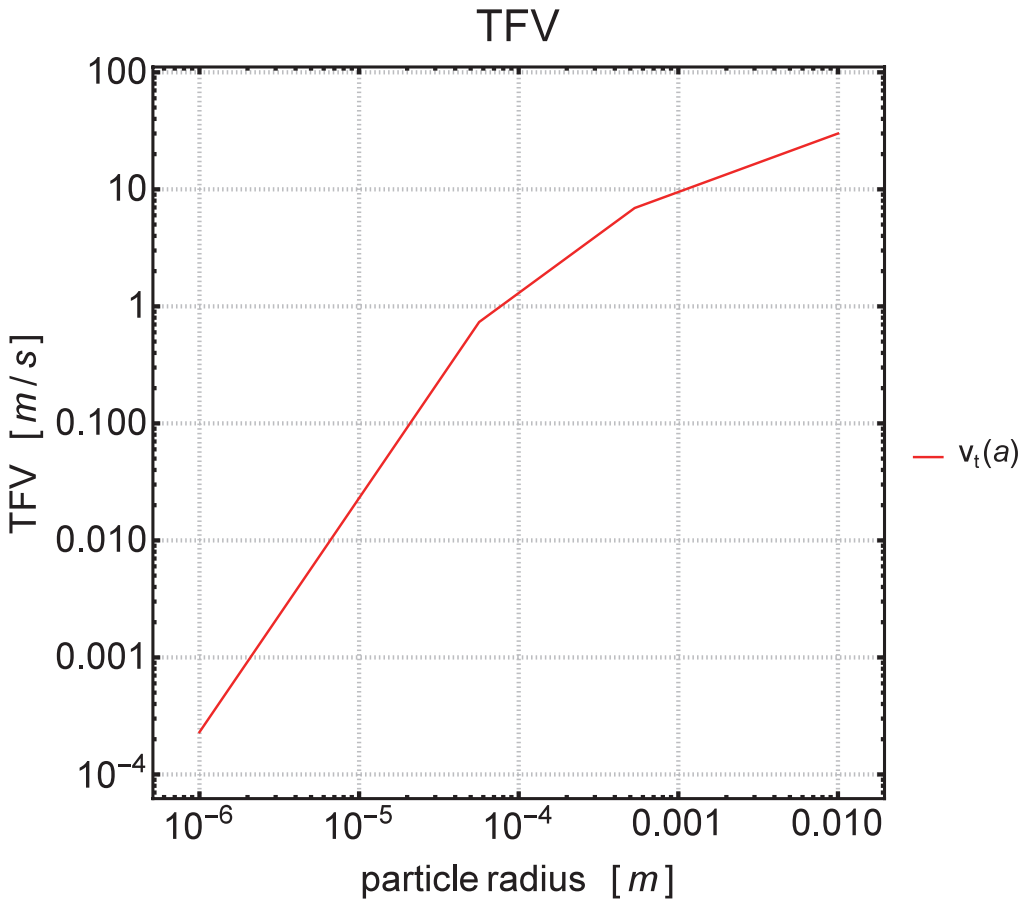

Figure 3.9: The terminal fall velocity (TFV) with a radius a at sea level. Constants p in Equation (3.84) are given as 2 for $Re < 6$, 1 for $6 \leq Re < 500$, and 0.5 for $500 \leq Re < 200,000$, assuming atmospheric conditions at sea level (Bonadonna and Phillips, 2003; Folch, 2012). Constants c in Equation (3.85) are given as 2.3×10^8 for $Re < 6$, 1.3×10^4 for $6 \leq Re < 500$, and 3.0×10^2 for $500 \leq Re < 200,000$, assuming atmospheric conditions at sea level (Bonadonna and Phillips, 2003; Folch, 2012).

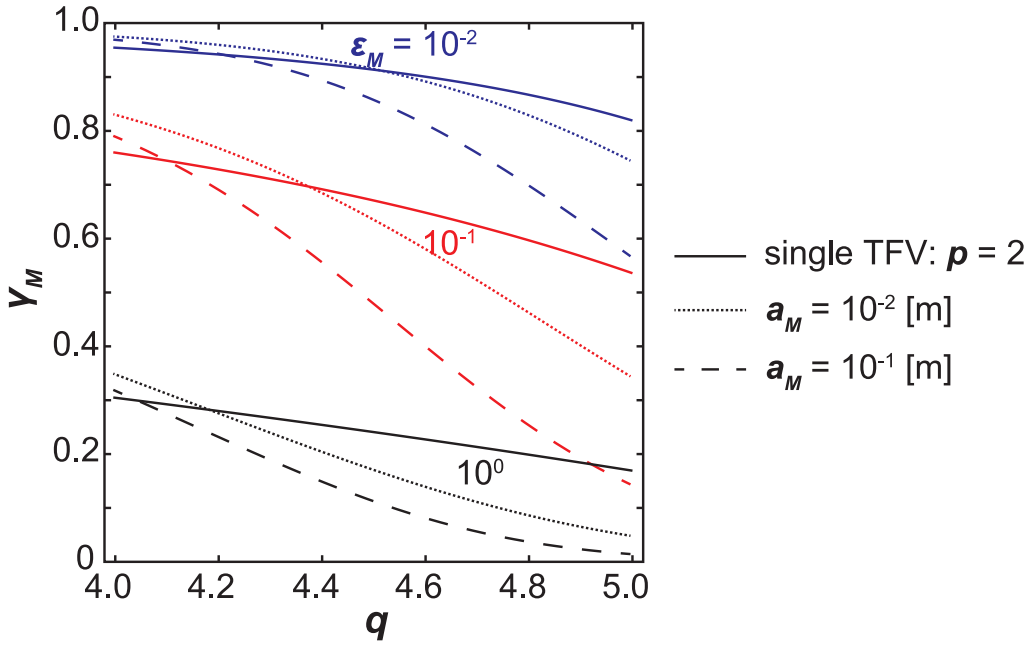

Figure 3.10: Analytical and numerical results of the relationship between the power–law exponent of the source GSD q and the thickness ratio of the largest particles existing layer to the total thickness, γ_M. The a_M is the radius of the largest particle, and ε_M is defined by t_M/t_{src}. *Blue lines*: $\varepsilon_M = 10^{-2}$, *Red lines*: $\varepsilon_M = 10^{-1}$, *Black lines*: $\varepsilon_M = 10^{0}$, *solid lines*: analytical results, *dotted lines*: results of calculation for $a_M = 10^{-2}$ m, *dashed lines*: results of calculation for $a_M = 10^{-1}$ m.

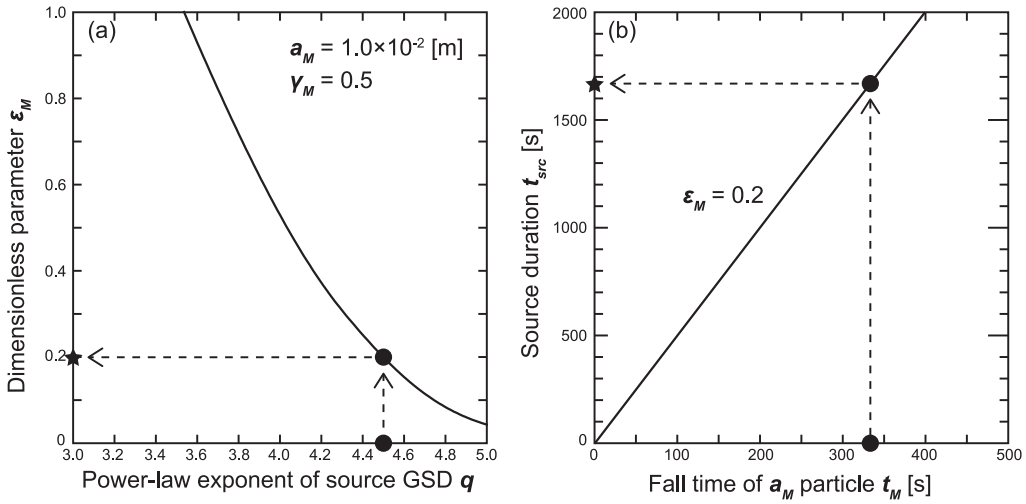

Figure 3.11: A result of the virtual application of the CS model. (a) Estimation of the parameter ε_M as approximately 0.2 (values of $a_M = 1.0 \times 10^{-3}$ m, $q = 4.5$, and $\gamma_M = 0.5$, which are given as assumptions of geological data, are used). (b) Estimation of the source duration t_{src} as 1.6 $\times 10^3$ s (the estimated values of the γ_M and fall time of the particle $a_M = 1.0 \times 10^{-2}$ m from the source height $H = 10^4$ m with TFV at sea level, t_M are used).

Chapter 4

Two–dimensional models

In this section, we provide two–dimensional theories which are spatially expanded from one–dimensional theories. We define the horizontal distance from the vent as r corresponding to the x or y axes in chapter 2.

Assumptions of the physical processes in two–dimensional theories

Plume dynamics of ash cloud depend on the source mass flux, GSD of particles at the vent, geometry of the vent, and atmospheric properties. Trajectory of the ash cloud is different depending on the eruption intensity and the horizontal wind speed. When the eruption intensity is strong and/or horizontal wind speed is low, a volcanic plume rises vertically and spreads radially at the neutral buoyancy level (NBL) to form an umbrella cloud (e.g., Sparks, 1986; Woods, 1988). On the other hand, when the eruption intensity is weak and wind speed is high, a volcanic plume is bent by the wind (Bonadonna et al., 2005). Plume dynamics is characterized as two regions: vertical rise up from the vent as an eruption column and horizontal expansion. In the case of the strong eruption intensity, it is easy to distinguish these two regions. In the case of the weak eruption intensity and high wind speed, it is difficult to separate bent-over plume into two regions, but it may be possible to distinguish the bent-over region and the horizontal expanding region. In the proximal area from the vent, the effects of the geometry of the plume and the unsteady property of the volcanic eruption are large from the point of view of the spatiotemporal scale of the transportation. In the distal area from the vent, on the other hand, it may be

possible to neglect the effect of the transportation from the eruption column or bent-over plume. We establish two–dimensional models to evaluate the spatiotemporal variation of the GSDs and to understand the relationship between the source conditions and the sedimentary features assuming the particle supply from the horizontally expanding ash cloud.

In the two–dimensional transportation and sedimentation theory, we give additional assumptions to the one–dimensional theory about the dynamics of ash cloud expansion to determine the relationship among physical parameters of the eruption such as the source height and magma discharge rate, the temporal variation of the source GSD, and the spatial distribution of the sediment (Fig. 4.1):

(1) The "source" position is given as the top of the eruption column at distance $r' = 0$ where r' is the horizontal distance from the vent at the source height.

(2) Ash cloud spreads horizontally on the height of the NBL at height $z = H_b(r', t')$.

(3) Particles are fractionated from the bottom of the current (ash cloud) at height $z = H_{cb}(r', t')$ corresponding to $H_b(r', t')$.

(4) Fractionated particles fall through the atmosphere and are advected by the wind.

(5) Particles settle on the ground surface.

To describe the temporal and spatial variations of GSD in the ash cloud, we give the GSD function in unit area in the ash cloud. We assume that the particles in the current is homogeneously distributed at distance r' and time t', then the GSD function in the ash cloud at a distance r' and time t' with a radius a is given as $F_{AC}(a, r', t')$ no./(m$^2\cdot$ m). We give the GSD function at the source height $z = H_{cb}$ and a distance $r' = 0$ as $F_{src}(a, t')$ as the "source" in the two–dimensional transportation and sedimentation theory, then

$$F_{src}(a, t') = F_{AC}(a, r' = 0, t'). \tag{4.1}$$

We assume that ash cloud spreads horizontally at NBL fractionating particles from the bottom of the ash cloud to the underlying atmosphere. We give the height at the top of the current at distance r' and time t' as $z = H_{ct}(r', t')$, then the thickness of the ash cloud at distance r' and time t', $L(r', t')$ is

$$L(r', t') = H_{ct}(r', t') - H_{cb}(r', t'). \tag{4.2}$$

We assume that the vertical distribution of the particles in the ash cloud at distance r' and time t' is homogeneous. The expansion velocity u_b is defined by the giving model.During the horizontal transportation process in the ash cloud, we assume that the efficiency of the fractionation depends on the fall velocity of a particle corresponding to the particle radius a and the duration existing in the ash cloud corresponding to the travel distance from the source r'. We define the GSD function of the fractionated particles at distance r', height $H_{cb}(r', t')$ and time t' as the fractionated GSD function f_{frc}, then

$$\left| \frac{dF_{AC}(a, r', t')}{dt'} \right| = f_{frc}(a, r', t') \times v_t(a), \tag{4.3}$$

$$f_{frc}(a, r', t') = f(a, r', z' = H_{cb}(r', t'), t'), \tag{4.4}$$

which corresponds to the source GSD function in the one–dimensional theory.

As shown in Equation (2.7), the settling GSD function is defined in the two–dimensional descriptions as

$$f_{stl}(a, r, t) = f(a, r, z = h(t), t). \tag{4.5}$$

As shown in Equation (2.37), the settling GSD function is approximated as

$$f_{stl}(a, r, t) = f(a, r, z = 0, t). \tag{4.6}$$

As shown in Equations (2.26) to (2.28), in the two–dimensional theory, we give the wind velocity which has only component of r axis from the assumptions in chapter 2, then

$$\boldsymbol{v}(r, z, t)\, \hat{\boldsymbol{r}} = \bar{u} = \text{const.}, \tag{4.7}$$

$$\boldsymbol{v}\left(r,z,t\right)\hat{\boldsymbol{z}}=\bar{w}=0, \tag{4.8}$$

where $\hat{\boldsymbol{r}}$ is unit vectors of r–coordinate. As shown in Equation (2.25), we define the absolute value of the TFV as $v_t\left(a\right)$ in the two–dimensional theory, as same as the definition in the one–dimensional model.

Fluxes of falling particles with a radius a shown in Equations (2.18) to (2.20) in two–dimensional models are

$$\boldsymbol{j_n}\left(a,r,z,t\right)=f\left(a,r,z,t\right)\times\left(\bar{u}\hat{\boldsymbol{r}}-v_t\left(a\right)\hat{\boldsymbol{z}}\right), \tag{4.9}$$

$$\boldsymbol{j_v}\left(a,r,z,t\right)=f\left(a,r,z,t\right)\times\left(\bar{u}\hat{\boldsymbol{r}}-v_t\left(a\right)\hat{\boldsymbol{z}}\right)\times V^*\left(a\right), \tag{4.10}$$

$$\boldsymbol{j_m}\left(a,r,z,t\right)=f\left(a,r,z,t\right)\times\left(\bar{u}\hat{\boldsymbol{r}}-v_t\left(a\right)\hat{\boldsymbol{z}}\right)\times V^*\left(a\right)\times\rho_s\left(a\right). \tag{4.11}$$

Similarly, fluxes of falling particles shown in Equations (2.21) to (2.23) are

$$\boldsymbol{J_n}\left(r,z,t\right)=\int_0^\infty f\left(a,r,z,t\right)\times\left(\bar{u}\hat{\boldsymbol{r}}-v_t\left(a\right)\hat{\boldsymbol{z}}\right)da, \tag{4.12}$$

$$\boldsymbol{J_v}\left(r,z,t\right)=\int_0^\infty f\left(a,r,z,t\right)\times\left(\bar{u}\hat{\boldsymbol{r}}-v_t\left(a\right)\hat{\boldsymbol{z}}\right)\times V^*\left(a\right)da, \tag{4.13}$$

$$\boldsymbol{J_m}\left(r,z,t\right)=\int_0^\infty f\left(a,r,z,t\right)\times\left(\bar{u}\hat{\boldsymbol{r}}-v_t\left(a\right)\hat{\boldsymbol{z}}\right)\times V^*\left(a\right)\times\rho_s\left(a\right)da. \tag{4.14}$$

The accumulation rate of the sediment in Equation (2.24) is

$$\begin{aligned}\frac{dh\left(r,t\right)}{dt} &= \frac{1}{\varphi_{PF}\left(z=h\left(r,t\right),t\right)}J_v\left(z=h\left(r,t\right),t\right)\\ &\approx \frac{1}{\varphi_{PF}\left(r,z=0,t\right)}J_v\left(r,z=0,t\right)\\ &= \frac{1}{\varphi_{PF}\left(r,z=0,t\right)}\int_0^\infty f_{stl}\left(a,r,t\right)v_t\left(a\right)V^*\left(a\right)da.\end{aligned} \tag{4.15}$$

As shown in Equation (2.30), the fall time from the source height with departure time t' to the sedimentation surface with the arrival time t with a radius a particles, t_a is

$$t_a\left(a,r',t'\right)=\frac{H_{cb}\left(r',t'\right)}{v_t\left(a\right)}, \tag{4.16}$$

then the relationship between the departure time and the arrival time in Equation (2.34) is

$$\begin{aligned} t &= t' + t_a\left(a, r', t'\right) \\ &= t' + \frac{H_{cb}\left(r', t'\right)}{v_t\left(a\right)}. \end{aligned} \tag{4.17}$$

As shown in Equations (2.31) and (2.32), the advection distance Δr is

$$\begin{aligned} \Delta r &= r - r' \\ &= \bar{u} t_a\left(a, r', t'\right) \\ &= \bar{u}\frac{H_{cb}\left(r', t'\right)}{v_t\left(a\right)}. \end{aligned} \tag{4.18}$$

We obtain the GSD relationship between f_{stl} and F_{src} by giving assumptions in the following section (Fig. 4.2).

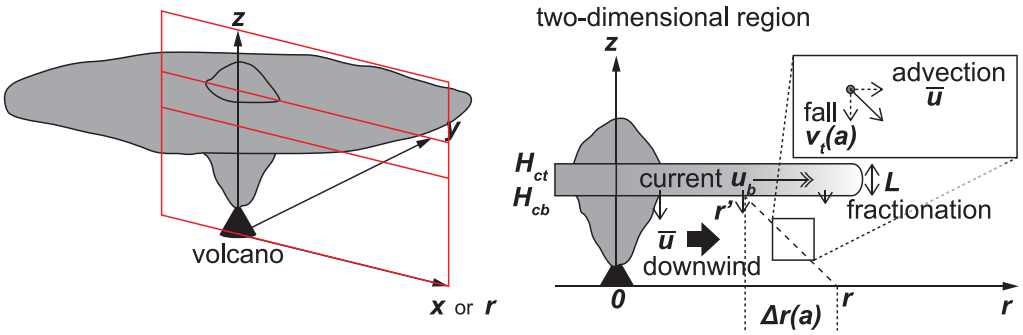

Figure 4.1: A schematic illustration of the two–dimensional transportation and sedimentation processes.

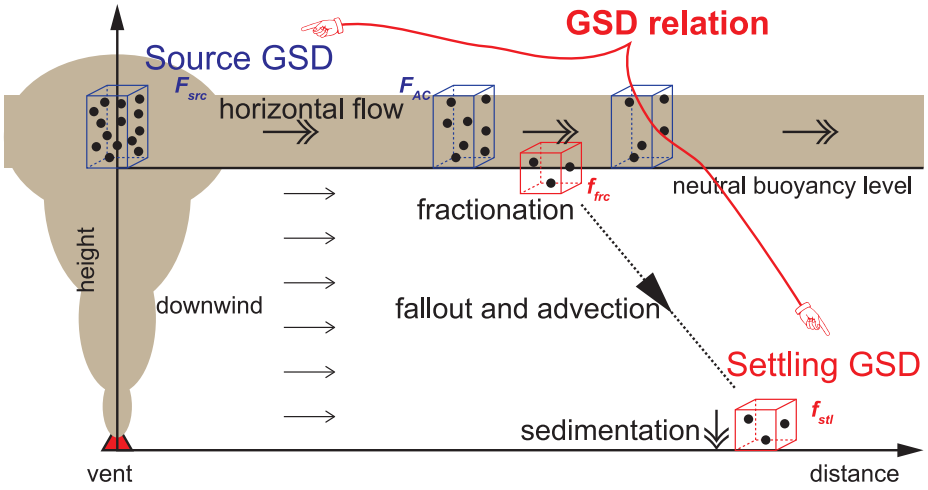

Figure 4.2: A schematic illustration of the GSD variation during the two–dimensional transportation and sedimentation processes. In the two–dimensional case, the "source" is defined as the position at the top of the eruption column. An ash cloud spreads as a current at the neutral buoyancy level reducing the number of particles. Fractionated particles fall through the atmosphere below the ash cloud advected by downwind, then settle on the ground surface. The settling GSD is related to the source GSD by giving the settings corresponding to the current of the ash cloud.

4.1 Constant height (CH) model

In the Constant height (CH) case, we give constants as follows:

$$H_{cb}(r', t') = H_{cb} = \text{const.}, \tag{4.19}$$

$$H_{ct}(r', t') = H_{ct} = \text{const.}, \tag{4.20}$$

then the thickness of the current is also given as constant, then

$$\begin{aligned} L(r', t') &= H_{ct} - H_{cb} \\ &= L = \text{const.} \end{aligned} \tag{4.21}$$

According to the Martin and Nokes' theory (1988), the fractionation of particles at the bottom of the ash cloud is defined as

$$\frac{dF_{AC}(a, t^*)}{dt^*} = -\frac{v_t(a)}{L} F_{AC}(a, t^*), \tag{4.22}$$

where t^* is the residence time in the ash cloud, then Equation (4.22) is

$$F_{AC}(a, t^*) = F_{AC}(a, t^* = 0)\, exp\left(-\frac{v_t(a)\, t^*}{L}\right). \tag{4.23}$$

In the two–dimensional theory, residence time t^* depends on the system of the spread of the ash cloud. If we give the velocity of the current spread at a distance r', $u_b(r')$, then

$$\frac{dr'}{dt_h} = u_b(r'), \tag{4.24}$$

where t_h is the horizontal travel time from the source to a distance r'. $u_b(r')$ may corresponds to the volumetric flow rate of the ash cloud, shape of the ash cloud, and wind velocity around the current. t_h is given as a function of a distance r', which indicates that residence time t^* is converted into the horizontal travel time $t_h(r')$, then Equations (4.22) and (4.23) are rewritten as

$$\frac{dF_{AC}(a, t_h(r'))}{dt_h(r')} = -\frac{v_t(a)}{L} F_{AC}(a, t_h(r')), \tag{4.25}$$

$$F_{AC}\left(a, t_h\left(r'\right)\right) = F_{AC}\left(a, t_h\left(r'\right) = 0\right) exp\left(-\frac{v_t\left(a\right) t_h\left(r'\right)}{L}\right). \tag{4.26}$$

Considering the relationship between the distance from the vent r' and the time t', Equation (4.26) is

$$F_{AC}\left(a, r', t'\right) = F_{src}\left(a, t' - t_h\left(r'\right)\right) exp\left(-\frac{v_t\left(a\right) t_h\left(r'\right)}{L}\right), \tag{4.27}$$

$$f_{frc}\left(a, r', t'\right) = \frac{1}{L} F_{src}\left(a, t' - t_h\left(r'\right)\right) exp\left(-\frac{v_t\left(a\right) t_h\left(r'\right)}{L}\right). \tag{4.28}$$

As shown in Equation (4.16), the fall time from the source height to the sedimentation surface with a radius a, t_a is

$$t_a\left(a\right) = \frac{H_{cb}}{v_t\left(a\right)}, \tag{4.29}$$

then the relationship between the departure time t' and the arrival time t in Equation (4.17) is

$$\begin{aligned} t &= t' + t_a\left(a\right) \\ &= t' + \frac{H_{cb}}{v_t\left(a\right)}. \end{aligned} \tag{4.30}$$

As shown in Equation (4.18), the advection distance Δr is

$$\begin{aligned} \Delta r &= r - r' \\ &= \bar{u} t_a\left(a\right) \\ &= \bar{u} \frac{H_{cb}}{v_t\left(a\right)}. \end{aligned} \tag{4.31}$$

The GSD relationship between at the source position and at the sedimentation surface at a distance r is

$$f_{stl}\left(a, r, t\right) = \frac{1}{L} F_{src}\left(a, t - t_{tot}\left(a, r\right)\right) exp\left(-\frac{v_t\left(a\right) t_h\left(r - \Delta r\right)}{L}\right), \tag{4.32}$$

$$\begin{aligned} t_{tot}\left(a, r\right) &= t_h\left(r'\right) + t_a\left(a\right) \\ &= t_h\left(r - \Delta r\left(a\right)\right) + t_a\left(a\right), \end{aligned} \tag{4.33}$$

where t_{tot} is the total travel time of the particle with a radius a from the source position $r' = 0$ to the arrival position with a distance r. By using Equations (4.15) and (4.32), the accumulation rate dh/dt is given by the source GSD function F_{src}, then

$$\begin{aligned}\frac{dh\left(r,t\right)}{dt} &= \frac{1}{\varphi_{PF}\left(r,t\right)}\int\frac{1}{L}F_{src}\left(a,t-t_a\left(a\right)-t_h\left(r-\Delta r\right)\right)\\ &\quad\times exp\left(-\frac{v_t\left(a\right)t_h\left(r-\Delta r\right)}{L}\right)v_t\left(a\right)V^*\left(a\right)da. \end{aligned} \tag{4.34}$$

As shown in Equation (4.34), the temporal and spatial variation of the sediment thickness is calculated by using giving the temporal variation of the source GSD function F_{src} and surrounding conditions. We give specific setting about the ash cloud expansion in the following section.

4.1.1 Constant current model

In this section, we assume the spread of the ash cloud with constant current velocity referred as the constant current model (Fig. 4.3). The constant current model is available when the current velocity strongly depends on the wind velocity at the height of the ash cloud and the observation locality is enough farther than the horizontal spatial scale of the bent-over region. In the constant current model, the current velocity u_b is given as constant during expansion, then

$$\frac{dr'}{dt_h} = u_b = \text{const.}, \tag{4.35}$$

then

$$t_h\left(r'\right) = \frac{r'}{u_b}, \tag{4.36}$$

$$r'\left(t_h\right) = u_b t_h. \tag{4.37}$$

From Equations (4.27) and (4.36), the horizontal variation of the GSD function in the ash cloud F_{AC} is given by

$$F_{AC}\left(a,r',t'\right) = F_{src}\left(a,t'-\frac{r'}{u_b}\right)exp\left(-\frac{v_t\left(a\right)}{u_b L}r'\right). \tag{4.38}$$

The GSD function of the fractionated particles form the ash cloud is represented from Equations (4.28) and (4.36), then

$$f_{frc}\left(a,r',t'\right)=\frac{1}{L}F_{src}\left(a,t'-\frac{r'}{u_b}\right)exp\left(-\frac{v_t\left(a\right)}{u_bL}r'\right). \tag{4.39}$$

From Equations (4.32) and (4.36), the settling GSD function at a distance r' and time t with a radius a is given by

$$\begin{aligned} f_{stl}\left(a,r,t\right) &= \frac{1}{L}F_{src}\left(a,t-\frac{H_{cb}}{v_t\left(a\right)}-\frac{r-\bar{u}\frac{H_{cb}}{v_t(a)}}{u_b}\right) \\ &\quad \times exp\left(-\frac{v_t\left(a\right)}{u_bL}\left(r-\bar{u}\frac{H_{cb}}{v_t\left(a\right)}\right)\right). \end{aligned} \tag{4.40}$$

The accumulation rate of the sediment at a distance r and time t is

$$\begin{aligned} \frac{dh\left(r,t\right)}{dt} &= \frac{1}{L\varphi_{PF}\left(t\right)}\int F_{src}\left(a,t-\frac{H_{cb}}{v_t\left(a\right)}-\frac{r-\bar{u}\frac{H_{cb}}{v_t(a)}}{u_b}\right) \\ &\quad \times exp\left(-\frac{v_t\left(a\right)}{u_bL}\left(r-\bar{u}\frac{H_{cb}}{v_t\left(a\right)}\right)\right)v_t\left(a\right)V^*\left(a\right)da, \end{aligned} \tag{4.41}$$

and the total travel time t_{tot} is

$$t_{tot}\left(a,r\right)=\frac{H_{cb}}{v_t\left(a\right)}+\frac{r-\bar{u}\frac{H_{cb}}{v_t(a)}}{u_b}. \tag{4.42}$$

Equation (4.41) suggests that the accumulation rate and the thickness of the sediment is calculated by giving initial conditions.

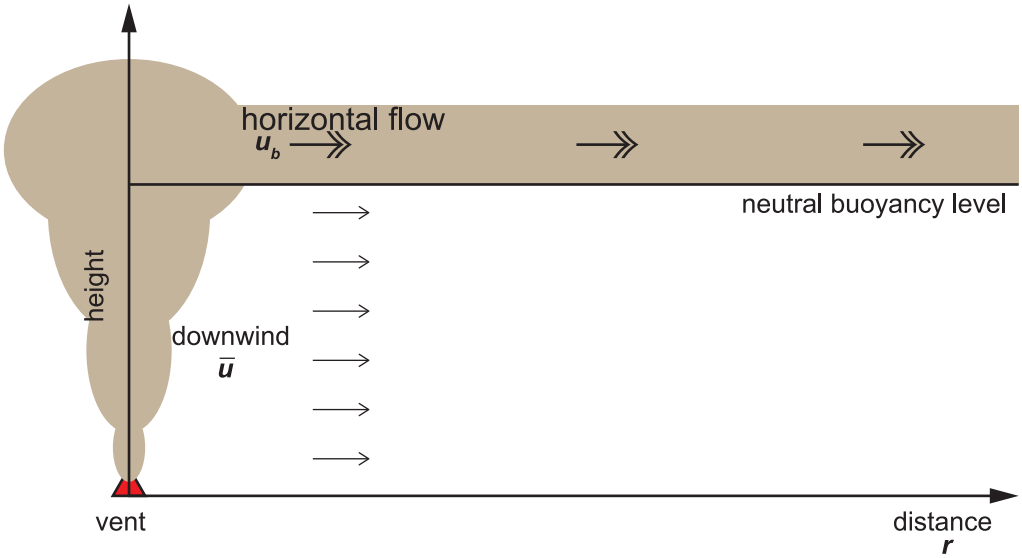

Figure 4.3: A schematic illustration of the constant current model. In the constant current model, the current velocity of the ash cloud is constant with a distance from the vent.

4.1.2 Another models

In this section, we give another models which depend on the style of the ash cloud expansion: cylinder model, fan model, and gravity current model (Fig. 4.4).

Cylinder model

The cylinder model is assumed as an umbrella cloud in the strong Plinian eruprion, which is based on the model in Koyaguchi (1994). When we assume the ash cloud as a cylinder, the volume of the columnar is given by

$$V^C = \pi r'^2 L, \tag{4.43}$$

where V^C is the volume of the cylinder. The volumetric flow rate Q is approximated as

$$Q = \frac{dV^c}{dt_h} \sim 2\pi r' \frac{dr'}{dt_h} L, \tag{4.44}$$

then the current velocity in the ash cloud u_b is

$$\begin{aligned} u_b &= \frac{dr'}{dt_h} \\ &= \frac{Q}{2\pi L} r'^{-1} = \frac{1}{2}\left(\frac{Q}{\pi L}\right)^{\frac{1}{2}} {t_h}^{-\frac{1}{2}}, \end{aligned} \tag{4.45}$$

$$t_h\left(r'\right) = \frac{\pi L}{Q} r'^2, \tag{4.46}$$

$$r'\left(t_h\right) = \left(\frac{Q}{\pi L}\right)^{\frac{1}{2}} {t_h}^{\frac{1}{2}}. \tag{4.47}$$

From Equations (4.27) and (4.46), the horizontal variation of the GSD function in the ash cloud F_{AC} is given by

$$F_{AC}\left(a, r', t'\right) = F_{src}\left(a, t' - \frac{\pi L}{Q} r'^2\right) exp\left(-\frac{\pi v_t\left(a\right)}{Q} r'^2\right). \tag{4.48}$$

The GSD function of the fractionated particles form the ash cloud is represented from Equations (4.28) and (4.46), then

$$f_{frc}\left(a, r', t'\right) = \frac{1}{L} F_{src}\left(a, t' - \frac{\pi L}{Q} r'^2\right) exp\left(-\frac{\pi v_t\left(a\right)}{Q} r'^2\right). \tag{4.49}$$

From Equations (4.32) and (4.46), the settling GSD function at a distance r' and time t with a radius a is given by

$$\begin{aligned} f_{stl}(a,r,t) &= \frac{1}{L}F_{src}\left(a, t-\frac{H_{cb}}{v_t(a)}-\frac{\pi L}{Q}\left\{r-\bar{u}\frac{H_{cb}}{v_t(a)}\right\}^2\right) \\ &\quad \times exp\left(-\frac{\pi v_t(a)}{Q}\left\{r-\bar{u}\frac{H_{cb}}{v_t(a)}\right\}^2\right). \end{aligned} \tag{4.50}$$

The accumulation rate of the sediment at a distance r and time t is

$$\begin{aligned} \frac{dh(r,t)}{dt} &= \frac{1}{L\varphi_{PF}(t)}\int F_{src}\left(a, t-\frac{H_{cb}}{v_t(a)}-\frac{\pi L}{Q}\left\{r-\bar{u}\frac{H_{cb}}{v_t(a)}\right\}^2\right) \\ &\quad \times exp\left(-\frac{\pi v_t(a)}{Q}\left\{r-\bar{u}\frac{H_{cb}}{v_t(a)}\right\}^2\right) v_t(a) V^*(a)\, da, \end{aligned} \tag{4.51}$$

and the total travel time t_{tot} is

$$t_{tot}(a,r) = \frac{H_{cb}}{v_t(a)}+\frac{\pi L}{Q}\left\{r-\bar{u}\frac{H_{cb}}{v_t(a)}\right\}^2. \tag{4.52}$$

Fan model

The fan model is assumed as a weak plume with strong wind velocity around the ash cloud. When we assume an umbrella ash cloud as a fan, the volume of the ash cloud is given by

$$V^F = \frac{\theta L}{2}r'^2, \tag{4.53}$$

where V^F is the volume of the fan, and θ is angle of the fan. The volumetric flow rate Q is approximated as

$$Q = \frac{dV^F}{dt_h} \sim r'\theta L\frac{dr'}{dt_h}, \tag{4.54}$$

then the current velocity in the ash cloud u_b is

$$\begin{aligned} u_b &= \frac{dr'}{dt_h} \\ &= \frac{Q}{\theta L}r'^{-1} = \left(\frac{Q}{2\theta L}\right)^{\frac{1}{2}} {t_h}^{-\frac{1}{2}}, \end{aligned} \tag{4.55}$$

$$t_h(r') = \frac{\theta L}{2Q}r'^2, \tag{4.56}$$

$$r'(t_h) = \left(\frac{2Q}{\theta L}\right)^{1/2} {t_h}^{\frac{1}{2}}. \tag{4.57}$$

From Equations (4.27) and (4.56), the horizontal variation of the GSD function in the ash cloud F_{AC} is given by

$$F_{AC}(a, r', t') = F_{src}\left(a, t' - \frac{\theta L}{2Q} r'^2\right) exp\left(-\frac{v_t(a)\,\theta}{2Q} r'^2\right). \tag{4.58}$$

The GSD function of the fractionated particles form the ash cloud is represented from Equations (4.28) and (4.56), then

$$f_{frc}(a, r', t') = \frac{1}{L} F_{src}\left(a, t' - \frac{\theta L}{2Q} r'^2\right) exp\left(-\frac{v_t(a)\,\theta}{2Q} r'^2\right). \tag{4.59}$$

From Equations (4.32) and (4.56), the settling GSD function at a distance r' and time t with a radius a is given by

$$\begin{aligned} f_{stl}(a, r, t) &= \frac{1}{L} F_{src}\left(a, t - \frac{H_{cb}}{v_t(a)} - \frac{\theta L}{2Q}\left\{r - \bar{u}\frac{H_{cb}}{v_t(a)}\right\}^2\right) \\ &\quad \times exp\left(-\frac{v_t(a)\,\theta}{2Q}\left\{r - \bar{u}\frac{H_{cb}}{v_t(a)}\right\}^2\right). \end{aligned} \tag{4.60}$$

The accumulation rate of the sediment at a distance r and time t is

$$\begin{aligned} \frac{dh(r,t)}{dt} &= \frac{1}{L\varphi_{PF}(t)} \int F_{src}\left(a, t - \frac{H_{cb}}{v_t(a)} - \frac{\theta L}{2Q}\left\{r - \bar{u}\frac{H_{cb}}{v_t(a)}\right\}^2\right) \\ &\quad \times exp\left(-\frac{v_t(a)\,\theta}{2Q}\left\{r - \bar{u}\frac{H_{cb}}{v_t(a)}\right\}^2\right) v_t(a)\, V^*(a)\, da, \end{aligned} \tag{4.61}$$

and the total travel time t_{tot} is

$$t_{tot}(a, r) = \frac{H_{cb}}{v_t(a)} + \frac{\theta L}{2Q}\left(r - \bar{u}\frac{H_{cb}}{v_t(a)}\right)^2. \tag{4.62}$$

Gravity current model

The gravity current model is assumed as more realistic expansion of an umbrella cloud during the large Plinian eruption, which is based on the existing model (Sparks et al., 1997).

$$u_b = \frac{dr'}{dt_h}$$

$$= \frac{2}{3} C^{GC\frac{1}{2}} r'^{-\frac{1}{2}} = \frac{2}{3} C^{GC\frac{1}{3}} {t_h}^{-\frac{1}{3}}, \tag{4.63}$$

$$t_h(r') = C^{GC^{-\frac{1}{2}}} r'^{\frac{3}{2}}, \tag{4.64}$$

$$r'(t_h) = C^{GC\frac{1}{3}} r'^{\frac{2}{3}}, \tag{4.65}$$

$$C^{GC} \equiv \frac{3\lambda NQ}{2\pi}, \tag{4.66}$$

where λ is an empirical constant, N is Brunt-Väisälä frequency, and C^{GC} is a constant. From Equations (4.27) and (4.64), the horizontal variation of the GSD function in the ash cloud F_{AC} is given by

$$F_{AC}(a, r', t') = F_{src}\left(a, t' - C^{GC^{-\frac{1}{2}}} r'^{\frac{3}{2}}\right) exp\left(-\frac{v_t(a)}{L} C^{GC^{-\frac{1}{2}}} r'^{\frac{3}{2}}\right). \tag{4.67}$$

The GSD function of the fractionated particles form the ash cloud is represented from Equations (4.28) and (4.64), then

$$f_{frc}(a, r', t') = \frac{1}{L} F_{src}\left(a, t' - C^{GC^{-\frac{1}{2}}} r'^{\frac{3}{2}}\right) exp\left(-\frac{v_t(a)}{L} C^{GC^{-\frac{1}{2}}} r'^{\frac{3}{2}}\right). \tag{4.68}$$

From Equations (4.32) and (4.64), the settling GSD function at a distance r' and time t with a radius a is given by

$$\begin{aligned} f_{stl} &= \frac{1}{L} F_{src}\left(a, t - \frac{H_{cb}}{v_t(a)} - C^{GC^{-\frac{1}{2}}}\left\{r - \bar{u}\frac{H_{cb}}{v_t(a)}\right\}^{\frac{3}{2}}\right) \\ &\quad \times exp\left(-\frac{v_t(a)}{L} C^{GC^{-\frac{1}{2}}}\left\{r - \bar{u}\frac{H_{cb}}{v_t(a)}\right\}^{\frac{3}{2}}\right). \end{aligned} \tag{4.69}$$

The accumulation rate of the sediment at a distance r and time t is

$$\begin{aligned} \frac{dh(r,t)}{dt} &= \frac{1}{L\varphi_{PF}(t)} \int F_{src}\left(a, t - \frac{H_{cb}}{v_t(a)} - C^{GC^{-\frac{1}{2}}}\left\{r - \bar{u}\frac{H_{cb}}{v_t(a)}\right\}^{\frac{3}{2}}\right) \\ &\quad \times exp\left(-\frac{v_t(a)}{L} C^{GC^{-\frac{1}{2}}}\left\{r - \bar{u}\frac{H_{cb}}{v_t(a)}\right\}^{\frac{3}{2}}\right) v_t(a) V^*(a)\, da, \end{aligned} \tag{4.70}$$

and the total travel time t_{tot} is

$$t_{tot}(a, r) = \frac{H_{cb}}{v_t(a)} + C^{GC^{-\frac{1}{2}}}\left\{r - \bar{u}\frac{H_{cb}}{v_t(a)}\right\}^{\frac{3}{2}}. \tag{4.71}$$

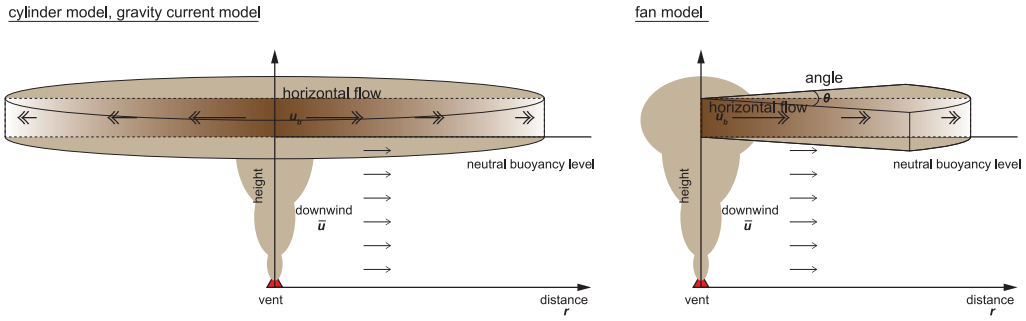

Figure 4.4: Schematic illustrations of the cylinder model and the gravity current model (left) and the fan model (right). In these models, the volumetric flow rate Q is given. Thus, the current velocity of the ash cloud u_b decreases with a distance from the vent owing to the geometry of the ash cloud.

4.2 Constant source (CS) model

In this section, we give the constant source GSD function and the constant source height during the particle supply, then

$$F_{src}\left(a,t'\right)=F_{src}^{CS}\left(a\right)\times\sqcap\left(\tau'\right), \tag{4.72}$$

$$H_{cb}\left(r',t'\right)=H_{cb}=\text{const.}, \tag{4.73}$$

$$H_{ct}\left(r',t'\right)=H_{ct}=\text{const.}, \tag{4.74}$$

where $F_{src}^{CS}\left(a\right)$ is the source GSD function in the two–dimensional constant source (CS) model. The thickness of the current is also given as constant, then

$$\begin{aligned} L\left(r',t'\right) &= H_{ct}-H_{cb} \\ &= L=\text{const.}, \end{aligned} \tag{4.75}$$

In the two–dimensional CS model, we give constant size range of the source GSD function as

$$a_m\leq a\leq a_M, \tag{4.76}$$

As shown in Equation (4.33), the total travel time of particles with a radius a which arrive at a distance r, $t_{tot}\left(a,r\right)$ is

$$\begin{aligned} t_{tot}\left(a,r\right) &= t_h\left(r'\right)+t_a\left(a\right) \\ &= t_h\left(r-\bar{u}t_a\left(a\right)\right)+t_a\left(a\right). \end{aligned} \tag{4.77}$$

In the two–dimensional CS model, the difference of the travel time corresponds to the grading structure of the sediment (Fig. 4.5). The grading structures are characterized as

$$\begin{cases} \left(\frac{\partial t_{tot}(a=a_M,r)}{\partial a}\right)_r<0 & \text{: normal grading,} \\ \left(\frac{\partial t_{tot}(a=a_M,r)}{\partial a}\right)_r>0 & \text{: reverse grading.} \end{cases} \tag{4.78}$$

Here after, we regard the value of the TFV as a particle size for the sake of simplicity, the Equation (4.77) is rewritten as

$$\begin{aligned} t_{tot}\left(v_t, r\right) &= t_h\left(r'\right) + t_{v_t}\left(v_t\right) \\ &= t_h\left(r - \bar{u}t_{v_t}\left(v_t\right)\right) + t_{v_t}\left(v_t\right). \end{aligned} \tag{4.79}$$

$$t_a\left(v_t\right) = \frac{H_{cb}}{v_t}. \tag{4.80}$$

$$\begin{cases} \left(\frac{\partial t_{tot}(v_t = v_t(a_M), r)}{\partial v_t}\right)_r < 0 & : \text{normal grading}, \\ \left(\frac{\partial t_{tot}(v_t = v_t(a_M), r)}{\partial v_t}\right)_r > 0 & : \text{reverse grading}. \end{cases} \tag{4.81}$$

We search the boundary condition of the normal grading structure and the reverse grading structure in the following section.

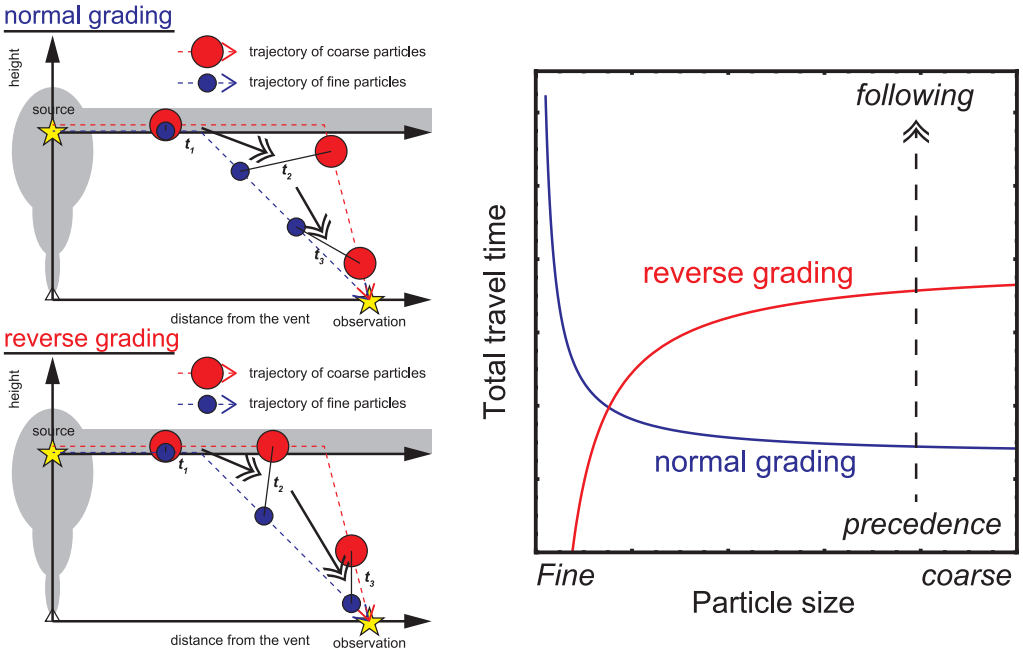

Figure 4.5: Schematic illustrations of the transportation (left) and the plot of the total travel time vs. particle size which arrives at a certain observation locality (right). Normal grading structure is achieved by the precedence of the coarse particles at a sedimentation surface. On the contrary, reverse grading is achieved by the precedence of the fine particles at a sedimentation surface.

4.2.1 Constant current model

In the constant current model, the total travel time is given as shown in Equation (4.42). The difference of the total travel time to the TFV at a distance r is

$$\left(\frac{\partial t_{tot}\left(v_t, r\right)}{\partial v_t}\right)_r = \left(\frac{\bar{u}}{u_b} - 1\right)\frac{H_{cb}}{{v_t}^2}. \tag{4.82}$$

As shown in Equation (4.82), grading structures depend on the ratio of $\bar{u}$ to u_b, then

$$\begin{cases} \bar{u} < u_b & : \text{normal grading,} \\ \bar{u} > u_b & : \text{reverse grading.} \end{cases} \tag{4.83}$$

By using the restrictions in Equation (4.83), it is possible to identify the cause of the grading structures in the pyroclastic fall deposit owing to whether the transportation or the original temporal variation of the eruption.

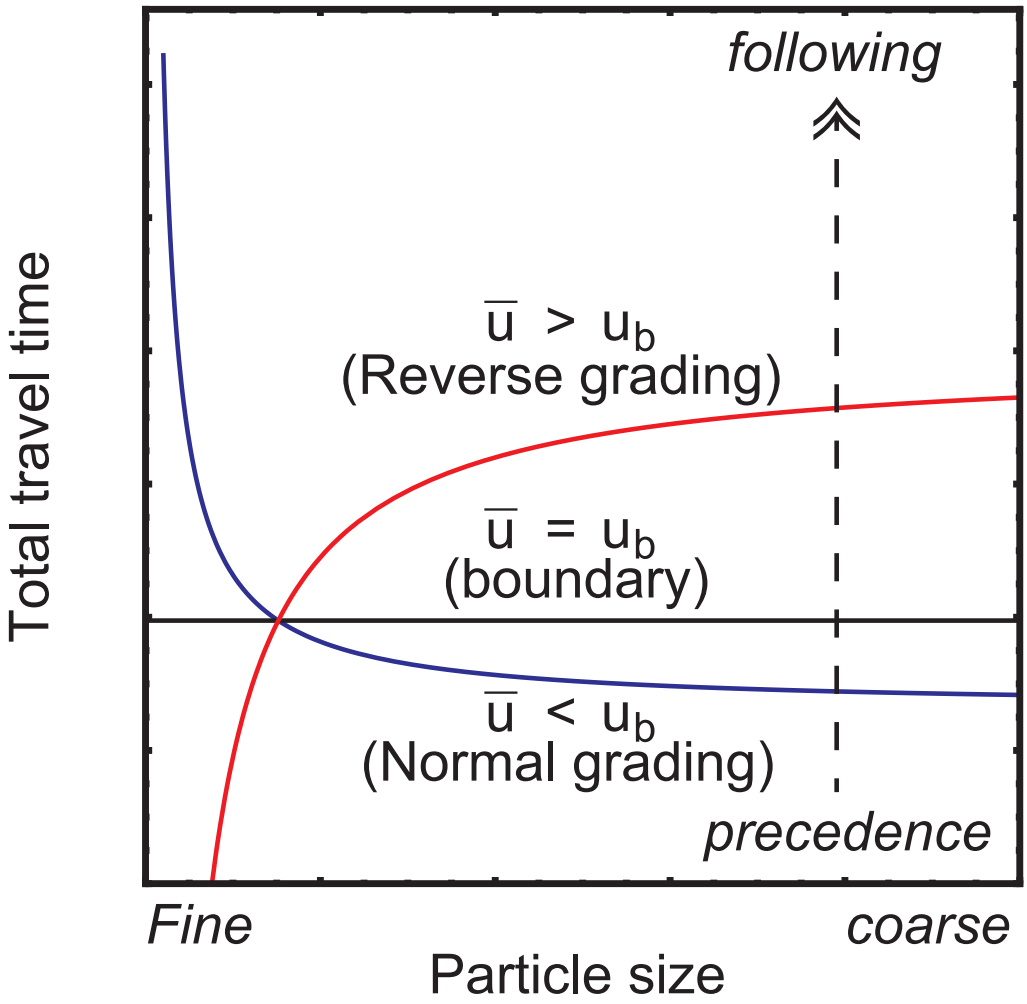

Figure 4.6: Plots of the total travel time vs. particle size which arrives at a certain observation locality in the constant current model. Normal grading structure is achieved when the downwind velocity is smaller than the current velocity. On the contrary, reverse grading is achieved when the downwind velocity is larger than the current velocity.

4.2.2 Another models

Cylinder model

In the cylinder model, the total travel time is given as shown in Equation (4.52). The difference of the total travel time to the TFV at a distance r is

$$\left(\frac{\partial t_{tot}\left(v_t, r\right)}{\partial v_t}\right)_r = -\frac{H_{cb}}{{v_t}^2} + \frac{2\pi L\bar{u}H_{cb}}{Q{v_t}^2}\left(r - \bar{u}\frac{H_{cb}}{v_t}\right). \tag{4.84}$$

Similarly, the difference of the total travel time to a distance r with TFV v_t is

$$\left(\frac{\partial t_{tot}\left(v_t, r\right)}{\partial r}\right)_{v_t} = \frac{2\pi L}{Q}\left(r - \bar{u}\frac{H_{cb}}{v_t}\right). \tag{4.85}$$

From Equations (4.84) and (4.85), grading structures depend on the characteristic distance from the vent:

$$\begin{cases} r_M \leq r < r_c & : \text{normal grading,} \\ r_c \leq r & : \text{reverse grading,} \end{cases} \tag{4.86}$$

$$r_c \equiv r_M + \frac{Q}{2\pi L\bar{u}}, \tag{4.87}$$

$$r_M \equiv \bar{u}\frac{H_{cb}}{v_t\left(a_M\right)}, \tag{4.88}$$

where r_M is the advection distance of the particle from the source height to the sedimentation surface with a radius a_M, and r_c is a characteristic distance giving the boundary of the grading structure. From Equation (4.85), the TFV of the first arrival particles at distance r, v_c is

$$v_c\left(r\right) = \bar{u}H_{cb}\left(r - \frac{Q}{2\pi L\bar{u}}\right)^{-1} \quad \text{for } r \geq r_c. \tag{4.89}$$

The characteristic distance at the source height in which the largest particle with a radius a_M arrive at distance r_c, ${r'}_c$ is

$${r'}_c \equiv \frac{Q}{2\pi L\bar{u}}. \tag{4.90}$$

As shown in Equation (4.45), the current velocity at a distance ${r'}_c$ is

$$u_b\left(r' = {r'}_c\right) = \frac{dr'\left(r' = {r'}_c\right)}{dt_h}$$

$$= \bar{u}. \tag{4.91}$$

Equation (4.91) implies the critical distance at which gives the superiority of the efficiency during the transportation between in the ash cloud and in the atmosphere.

Fan model

In the fan model, the total travel time is given as shown in Equation (4.62). The difference of the total travel time to the TFV at a distance r is

$$\left(\frac{\partial t_{tot}\left(v_t, r\right)}{\partial v_t}\right)_r = -\frac{H_{cb}}{{v_t}^2} + \frac{\theta L \bar{u} H_{cb}}{Q {v_t}^2}\left(r - \bar{u}\frac{H_{cb}}{v_t}\right). \tag{4.92}$$

Similarly, the difference of the total travel time to a distance r with TFV v_t is

$$\left(\frac{\partial t_{tot}\left(v_t, r\right)}{\partial r}\right)_{v_t} = \frac{\theta L}{Q}\left(r - \bar{u}\frac{H_{cb}}{v_t}\right). \tag{4.93}$$

From Equations (4.92) and (4.93), grading structures depend on the characteristic distance from the vent:

$$\begin{cases} r_M \leq r < r_c & : \text{normal grading,} \\ r_c \leq r & : \text{reverse grading,} \end{cases} \tag{4.94}$$

$$r_c \equiv r_M + \frac{Q}{\theta L \bar{u}}. \tag{4.95}$$

From Equation (4.93), the TFV of the first arrival particles at distance r, v_c is

$$v_c\left(r\right) = \bar{u} H_{cb}\left(r - \frac{Q}{\theta L \bar{u}}\right)^{-1} \quad \text{for } r \geq r_c. \tag{4.96}$$

The characteristic distance at the source height in which the largest particle with a radius a_M arrive at distance r_c, ${r'}_c$ is

$${r'}_c \equiv \frac{Q}{\theta L \bar{u}}. \tag{4.97}$$

As shown in Equation (4.55), the current velocity at a distance ${r'}_c$ is

$$\begin{aligned} u_b\left(r' = {r'}_c\right) &= \frac{dr'\left(r' = {r'}_c\right)}{dt_h} \\ &= \bar{u}. \end{aligned} \tag{4.98}$$

Equation (4.98) implies the critical distance at which gives the superiority of the efficiency during the transportation between in the ash cloud and in the atmosphere.

Gravity current model

In the gravity current model, the total travel time is given as shown in Equation (4.71). The difference of the total travel time to the TFV at a distance r is

$$\left(\frac{\partial t_{tot}\left(v_t, r\right)}{\partial v_t}\right)_r = -\frac{H_{cb}}{{v_t}^2} + \frac{3}{2}\frac{\bar{u}H_{cb}}{{v_t}^2}C^{-\frac{1}{2}}\left(r - \bar{u}\frac{H_{cb}}{v_t}\right)^{\frac{1}{2}}. \tag{4.99}$$

Similarly, the difference of the total travel time to a distance r with TFV v_t is

$$\left(\frac{\partial t_{tot}\left(v_t, r\right)}{\partial r}\right)_{v_t} = \frac{3}{2}C^{-\frac{1}{2}}\left(r - \bar{u}\frac{H_{cb}}{v_t}\right)^{\frac{1}{2}}. \tag{4.100}$$

From Equations (4.99) and (4.100), grading structures depend on the characteristic distance from the vent:

$$\begin{cases} r_M \leq r < r_c & : \text{normal grading,} \\ r_c \leq r & : \text{reverse grading,} \end{cases} \tag{4.101}$$

$$r_c \equiv r_M + \frac{4}{9}\frac{C}{\bar{u}^2}. \tag{4.102}$$

From Equation (4.100), the TFV of the first arrival particles at distance r, v_c is

$$v_c\left(r\right) = \bar{u}H_{cb}\left(r - \frac{4}{9}\frac{C}{\bar{u}^2}\right)^{-1} \quad \text{for } r \geq r_c. \tag{4.103}$$

The characteristic distance at the source height in which the largest particle with a radius a_M arrive at distance r_c, ${r'}_c$ is

$${r'}_c \equiv \frac{4}{9}\frac{C}{\bar{u}^2}. \tag{4.104}$$

As shown in Equation (4.63), the current velocity at a distance ${r'}_c$ is

$$\begin{aligned} u_b\left(r' = {r'}_c\right) &= \frac{dr'\left(r' = {r'}_c\right)}{dt_h} \\ &= \bar{u}. \end{aligned} \tag{4.105}$$

Equation (4.105) implies the critical distance at which gives the superiority of the efficiency during the transportation between in the ash cloud and in the atmosphere.

Effect of the wind around the current

To consider more realistic expansion of the ash cloud at the NBL, we assess the effect of the wind on the current velocity. Here we give wind velocity at NBL as u_w. Costa et al. (2013) gives the ratio of the current velocity u_b to the wind velocity at NBL u_w as the Richardson number Ri:

$$Ri \equiv \frac{{u_b}^2}{{u_w}^2}. \tag{4.106}$$

Based on the atmospheric observations, Costa et al. (2013) considered the three transportation regimes; the density transportation regime for $Ri > 1$, substantially passive transportation regime for $Ri < 0.25$, and the intermediate transportation regime for $0.25 \leq Ri \leq 1$. Based on these regimes, we redefine current velocities u_b in two–dimensional CS models, then

$$u_b^{CC} = \begin{cases} u_b & \text{for } 1 < Ri \\ u_w & \text{for } Ri \leq 1 \end{cases}, \tag{4.107}$$

$$u_b^{C} = \begin{cases} \frac{Q}{2\pi L} r'^{-1} & \text{for } 1 < Ri \\ u_w & \text{for } Ri \leq 1 \end{cases}, \tag{4.108}$$

$$u_b^{F} = \begin{cases} \frac{Q}{\theta L} r'^{-1} & \text{for } 1 < Ri \\ u_w & \text{for } Ri \leq 1 \end{cases}, \tag{4.109}$$

$$u_b^{GC} = \begin{cases} \frac{2}{3} C^{GC\,\frac{1}{2}} r'^{-\frac{1}{2}} & \text{for } 1 < Ri \\ u_w & \text{for } Ri \leq 1 \end{cases}, \tag{4.110}$$

where u_b^{CC}, u_b^{C}, u_b^{F}, u_b^{GC} are current velocities which include the effect of the wind velocity at NBL in the constant current model, the cylinder model, the fan mode, and the gravity current model, respectively. We define characteristic distances as

$$r'^{C}_{b} \equiv \frac{Q}{2\pi L u_w}, \tag{4.111}$$

$$r'^{F}_{b} \equiv \frac{Q}{\theta L u_w}, \tag{4.112}$$

$$r'^{GC}_{b} \equiv \frac{4}{9}\frac{C}{{u_w}^2}, \tag{4.113}$$

where r'^{C}_{b}, r'^{F}_{b}, r'^{GC}_{b} are characteristic distances which satisfy $Ri = 1$ in the cylinder model, the fan mode, and the gravity current model, respectively.

Comparison among downwind velocity during the fallout process $\bar{u}$, the wind velocity at NBL u_w, and the current velocity u_b provides us a restriction about the grading structure. The current velocity u_b at the boundary distance for the grading structure ${r'}_c$ satisfies

$$u_b\left(r' = {r'}_c\right) = \bar{u}. \tag{4.114}$$

In the cylinder model, the fan model, and the gravity current model, the current velocities decrease monotonically with the distance from the vent. According to the Richardson number, the current velocity u_b converge on the wind velocity at NBL u_b. Thus reverse grading structure is achieved when $\bar{u} > u_w$ is satisfied, which corresponds to ${r'}_c < {r'}_b$. On the contrary, when the atmospheric condition satisfies $\bar{u} < u_w$, the structure of the sediment is always normal grading (upward fining) in two–dimensional CS models. Based on these results, on observation of the reverse grading structure (upward coarsening) under the situation of the normal grading region in two–dimensional CS models implies the temporal variation of the volcanic activities, such as the source GSD, the eruption column height, and magma discharge rate.

Part II

Application to the 2011 Shinmoe–dake eruption

Chapter 5

Settings of the 2011 Shinmoe–dake eruptions

5.1 Overview of the 2011 Shinmoe–dake eruptions

We apply our models developed in the preceding chapters to the 2011 Shinmoe–dake subplinian eruption. Shinmoe–dake is an andesitic stratovolcano which belongs to the Kirishima volcano complex, south of Kyushu, southwest of Japan (the elevation is 1,421 m asl) (Fig. 5.1). Since August 2008, there had been several small phreatic eruptions at Shinmoe–dake. The sequence of the 2011 Shinmoe–dake eruptions has been reported as following (Fukuoka District Meteorological Observatory and Kagoshima Local Meteorological Observatory, 2012).

On January 19, a small phreatomagmatic eruption occurred, and made weak ash plume which was elongated to SE from the vent. An ash–fall deposit up to 0.5 cm thick was observed about 7 km SE of the vent, and extended to Nichinan City, 60 km SE from the vent (Miyabuchi et al. 2013). On January 22, a small ash emission occurred. A milky white plume rose up to about 200 m above the vent which was elongated to SE from the vent. From January 22 to 25, white plumes which extended from the rim of the vent up to about 200 m above the vent were sometimes observed.

At 07 h 31 min (Japan Standard Time; JST) on January 26, a phreatomagmatic eruption started from 14 h 49 min corresponding to a cock's tail jet with about 3,500 m asl high plume. Then it shifted to a subplinian eruption with a grayish white tephra

plume from 16 h 10 min, and the maximum height of the plume reached about 7,500 m asl (Shimbori et al. 2013). After the beginning of the eruption on January 26, the Fukuoka District Meteorological Observatory (FDMO) of the Japan Meteorological Agency (JMA) changed the volcanic alert level of Volcanic Warning (near-crater warning) from level 2 to level 3. The first subplinian eruption lasted until around 19 h on January 26.

After the first subplinian eruption, weak plume continued to rise, and the height of the plume was about 2,000 m asl. Around 22 h on January 26, the plume rose up about 4,000 asl, which continued to about 02 h on January 27. Then the plume height increased up to about 7,500 asl during the eruption from 02 h to 05 h on January 27, which corresponds to the second subplinian eruption.

At 15 h 41 min on January 27, an explosion occurred and ash was released with strong plume which reached about 6,000 m asl. After the explosion, a large amount of ash emission occurred from 16 h 22 min to 17 h 40 min, which corresponds to the third subplinian eruption. The maximum plume height was about 7,000 m asl during the third subplinian eruption.

After the third subplinian eruption, volcanic activity shifted to lava intrusion stage from January 28 in the morning, and started to fill the summit crater. At 12 h 47 min on January 28, the second explosion occurred and ejected ballistics up to 1.3 km the SW flank from the vent. On January 30, lava in the summit crater extended to approximately 500 m in diameter. Vulcanian eruptions continues from January 27 intermittently during lava emission stage, and the number of the vulcanian eruption decreased after February 9.

The largest vulcanian explosion occurred on March 13 and the plume height reached about 4,000 m above the crater rim. Small eruptions occurred intermittently until the end of August 2011. The last eruption occurred on August 31, and it continued to September 7.

The total amounts of ejecta produced by subplinian eruptions have been estimated

from geological data. The total amount of ejecta is 15–34 $\times 10^6$ m^3 for the sum of the first and the second subplinian eruption and 5.0–7.6 $\times 10^6$ m^3 for the third subplinian eruption (Maeno et al., 2014).

The total amount of ejecta is also estimated from geodetic data and the numerical study (Kozono et al., 2013). DRE volumes ejected by each subplinian eruptions are 4.06–5.07 $\times 10^6$ m^3 for the first subplinian eruption, 5.34–6.67 $\times 10^6$ m^3 for the second subplinian eruption, and 3.04–3.79 $\times 10^6$ m^3 (Kozono et al., 2013).

During the 2011 Shinmoe–dake eruptions, various geophysical observations were carried out such as the height of the plume observed by the ground-based weather radar network and meteorological satellites (Shimbori et al., 2013; Fig. 5.2), the geodetic change (Ueda et al., 2013; Fig. 5.3), SAR (Ozawa and Kozono, 2013), etc. The trajectory of the plume was bent owing to the weak eruption intensity and the high wind speed. The bent–over plume region was a few kilometers SE from the vent. We assume that, at the proximal area farther than a few kilometer, particle supply from the bent–plume was negligible and particles were supplied only from the horizontally expanding ash cloud.

As shown in Figure (5.2), rapid changes in the eruption column height during the first subplinian eruption occurred at the beginning of the eruption and the ending of the eruption in a short time scale compared to the eruption duration. We assume that the height of the ash cloud, which corresponds to the source height in the established models, were constant during the eruption. Thus, it is possible to apply one–dimensional and two–dimensional constant height models and to compare the temporal variations of geophysical data and the temporal variations of GSDs of ejected pyroclasts by using our model. We identify the stratigraphy of pyroclastic fall deposits produced by the 2011 Shinmoe–dake eruptions in the following section.

5.2 Stratigraphy of pyroclastic fall deposits produced by the 2011 Shinmoe–dake eruptions

The stratigraphy of pyroclastic fall deposits produced by the 2011 Shinmoe–dake eruptions has been reported (Nakada et al., 2013; Miyabuchi et al., 2013; Maeno et al., 2014; Iriyama and Toramaru, 2015). As the lowermost part of the deposit in a series of the 2011 Shinmoe–dake eruptions, a light yellow, thin layer exists, which is assumed as a materials produced by the phreatomagmatic eruption on January 19 and/or the morning of the January 26 corresponding to Layer 1 in Nakada et al. (2013) and unit 1 in Miyabuchi et al. (2013).

Above the layer of the phreatomagmatic products, pumice lapilli layer follows, which includes the coarsest particles in the sequence of the 2011 Shinmoe–dake eruptions in the upper part of this layer corresponding to the Layer 2–4 in Nakada et al. (2013), unit 2 in Miyabuchi et al. (2013), and Unit S1 and S2 in Maeno et al. (2014). This layer is assumed as the compositions of ejecta produced by the first and the second subplinian eruptions. This part shows upward coarsening (reverse grading) in the lower part, and also shows upward fining (normal grading) in the upper part. The relatively finer part in the lower part of this layer corresponds to the lower part of Layer 3 in Nakada et al. (2013) and unit 2L in Miyabuchi et al. (2013). The coarsest part in this layer corresponds to Layer 3 in Nakada et al. (2013) and unit 2M in Miyabuchi et al. (2013). The relatively finer par in the upper part of this layer corresponds to Layer 4 in Nakada et al. (2013) and unit 2U in Miyabuchi et al. (2013). Maeno et al. (2014) reported that there was a boundary of products of the first and the second subplinian eruptions in the middle part of the coarsest part of this layer corresponding to the lower part of Layer 3 in Nakada et al. (2013) and unit 2L in Miyabuchi et al. (2013) based on the stratigraphic variation of the bulk density of pumice. Thus, the lower part of this layer defined as Unit S1 and the upper part of this layer as Unit S2 corresponding to the first and the second subplinian eruption (Maeno et al., 2014).

Above the pumice lapilli layer, there is black lithic sand follows corresponding to the boundary of Layer 4/5 in Nakada et al. (2013), unit 2/3 in Miyabuchi et al. (2013), and Unit S2/S3 in Maeno et al. (2014). This layer corresponds to the explosion at 15 h 41 min on January 27 based on the local observation at Takachihogawara (2.8 km SE) reported in Miyabuchi et al. (2013).

Above the black lithic sand layer, pumiceous lapilli layer follows again corresponding to the ejecta of the third subplinian eruption. This layer corresponds to Layer 5 in Nakada et al. (2013), unit 3 in Miyabuchi et al. (2013), and Unit S3 in Maeno et al. (2014). There are following layers composed by ash and/or pumice, which are produced by ejecta of vulcanian eruptions after January 28.

Iriyama and Toramaru (2015) reported the stratigraphic variations of GSDs in pyroclastic fall deposits produced by the first and the second subpinian eruptions corresponding to the Layer 2–4 in Nakada et al. (2013), unit 2 in Miyabuchi et al. (2013), and Unit S1 and S2 in Maeno et al. (2014). They identified correspondence between the stratigraphic intervals of pyroclastic fall deposits and the eruption events based on the existence of the black lithic sand layer corresponding to the ejecta of vulcanian eruption at 15 h 41 min on January 27. They carried out the geological survey at three localities along the dispersal axis (NE from the vent) of the deposit; Tg (2.7 km SE), Mk (7.9 km SE) and Nt (11.3 km). The stratigraphic variations showed two sets of upward coarsening–fining variation in deposits, which is assumed to correspond to the eruption events of the first and the second subplinian eruption.

We explain the details about materials used in practical applications in the following chapters.

5.3 Materials

We focus on the pyroclastic fall deposits produced by subplinian eruptions. As applications of our theoretical models about transportation of sedimentation, we used pyroclastic

fall deposits at locality Mk produced by the first subplinian eruption reported in Iriyama and Toramaru (2015) (Fig. 5.1). The stratigraphic variations of the median pumice size Md_ϕ and the sorting σ_ϕ are shown in Figures 5.4 and 5.5. We also obtain stratigraphic variations of GSDs and the maximum pumice size MP shown in Figure 5.5.

Figure 5.1: Index map of Shinmoe–dake volcano at Kirishima volcanoes, Japan, and sampling sites of the 26–27 January 2011 pyroclastic fall deposits. Mk: Miike elementary school (7.9 km SE from the vent).

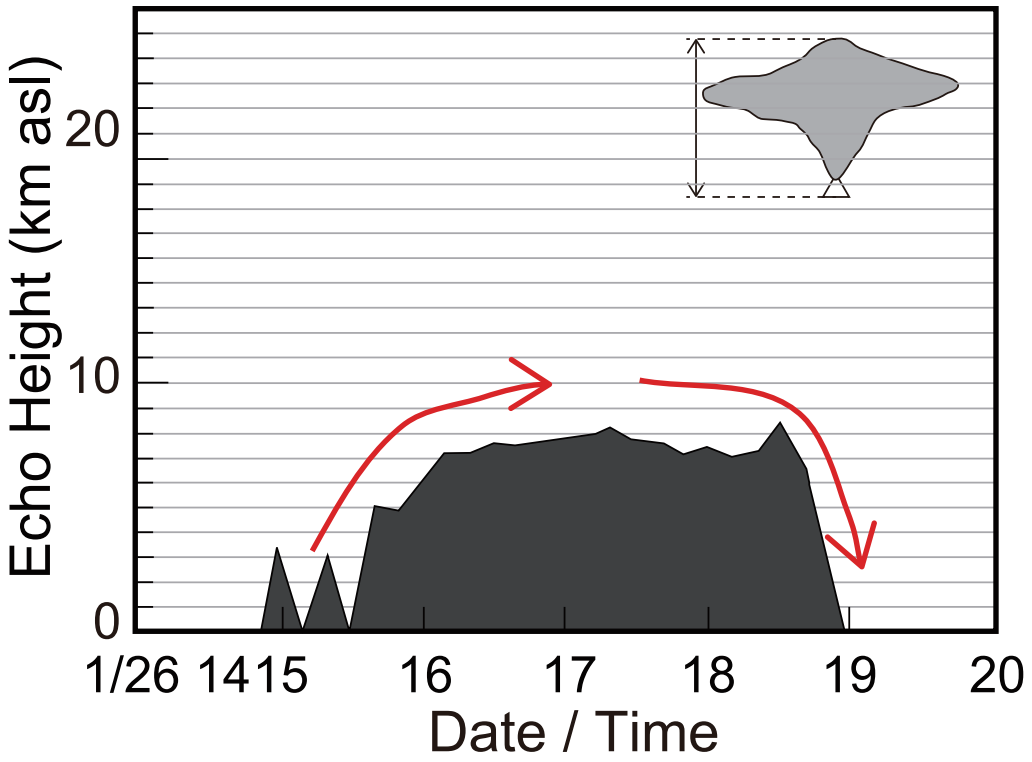

Figure 5.2: The temporal variation of the echo height during the first subplinian eruption (Shimbori et al., 2013).

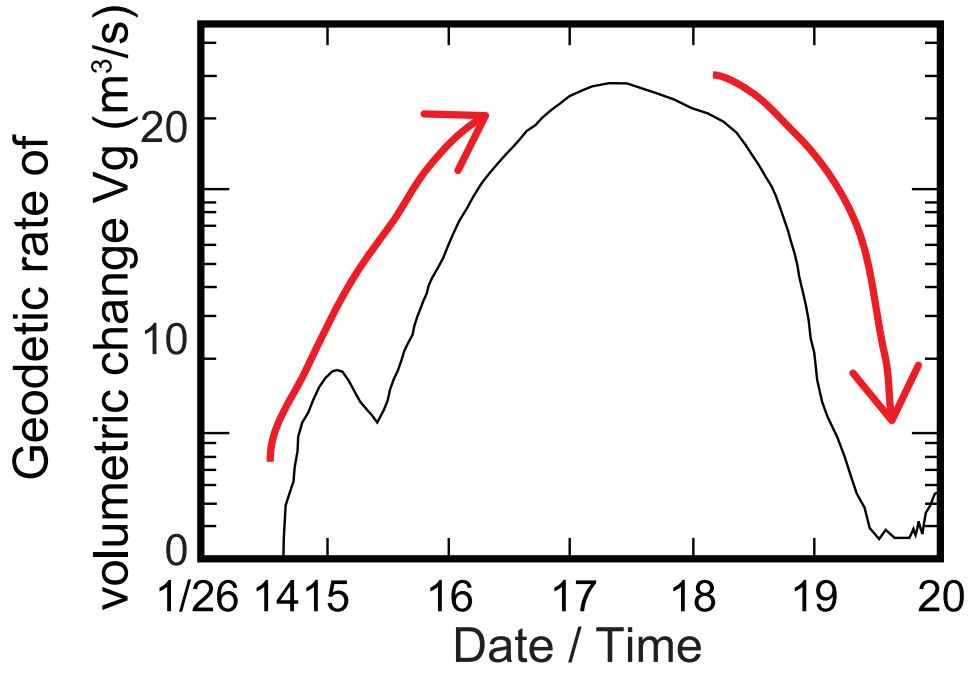

Figure 5.3: The temporal variation of geodetic rate of volumetric change during the first subplinian eruption (Ueda et al., 2013; Ichihara, 2016).

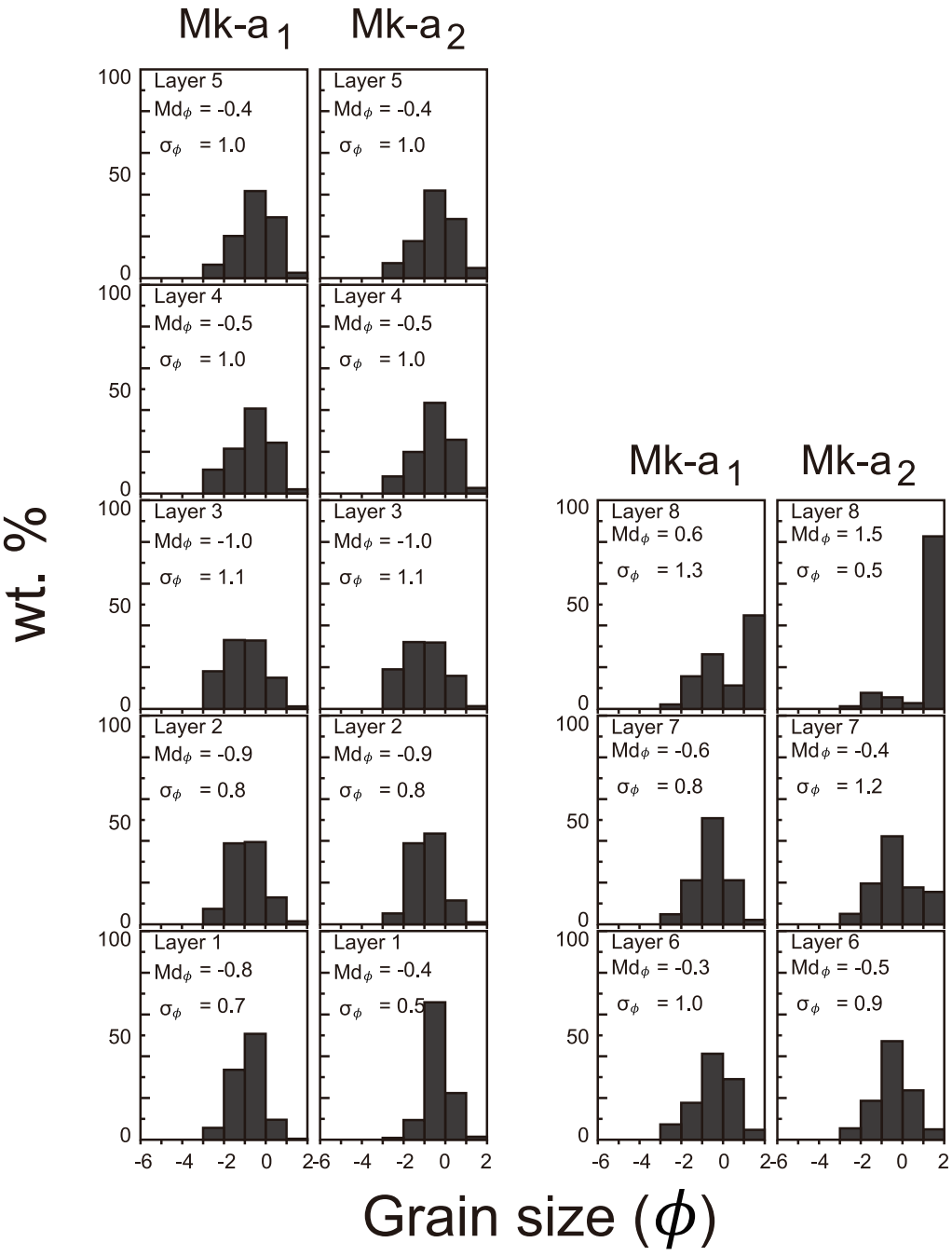

Figure 5.4: Grain–size histograms coarser than $\phi = 2$ of respective samples from the 2011 Shinmoe–dake deposits reported in Iriyama and Toramaru (2015).

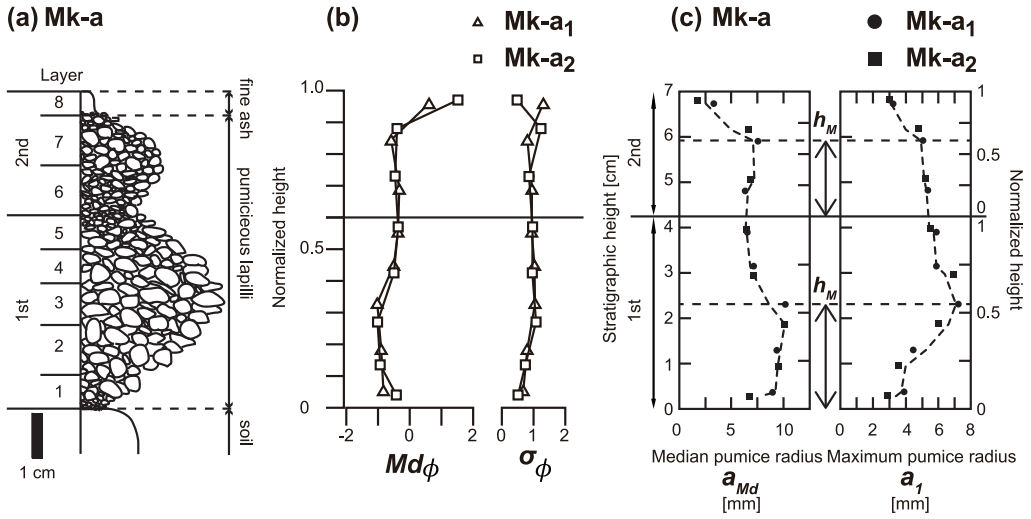

Figure 5.5: (a) A sketch of the pyroclastic fall deposit composed by ejecta of the first and the second subplinian eruptions. (b) Stratigraphic variations of Md_ϕ and σ_ϕ of the 2011 Shinmoe–dake eruption deposits (data from Iriyama and Toramaru, 2015). (c) Stratigraphic variations of the median pumice radius (a_{Md}; left) and the maximum pumice radius (a_1; right). *Dashed lines*: Stratigraphic variations of the median and the maximum pumice radius corresponding to the upper boundary of the thickness h_M in the one–dimensional CS model.

Chapter 6

Application of one–dimensional models

In this chapter, we apply one–dimensional models to the 2011 Shinmoe–dake subplinian eruptions. In section 6.1, we apply the constant source (CS) model and estimate the source duration t_{src} from the sedimentary structure and the GSD of the sediment. And section 6.2, we apply the conservation of the number and estimate the temporal variation of the source GSD $f_{src}(a, t')$ from the stratigraphic variation of the sediment GSD.

6.1 Estimation of the source duration

As an application of the CS model, according to the method illustrated in the preceding section, we estimated the dimensionless parameter ε_M and the source duration t_{src} from geological data of the first subplinian eruptions. Then, we compared the estimated and observed values of t_{src} because the duration t_{src} has been previously reported, and we discuss the factors affecting the discrepancy.

First, we summarized geological data of the 2011 Shinmoe–dake eruptions (Iriyama and Toramaru, 2015), which are used in this section. Iriyama and Toramaru (2015) conducted geological survey on January 29 and 30, soon after the eruption, and obtained two sets of samples, Mk–a1 and a2, with a short sampling time interval of one day from the same locality 7.9 km southeast from the vent (Fig. 5.5). The locality and the timing

of sampling were the same between Mk–a1 and a2; therefore, the two sets of samples were used to check the similarity of the observed data. Iriyama and Toramaru (2015) divided sediment 7 cm thick into eight layers with intervals of approximately 1 cm for both sets of samples. According to the stratigraphic variation of Md_ϕ in Iriyama and Toramaru (2015), the lower part of the sediment (Layers 1–5) is composed of ejecta of the first eruption, and the upper part (Layers 6–8) are composed of the ejecta of the second eruption. In this study, we regard the 60 % position from the base of the sediment as the boundary of the first and the second eruption on the basis of previous studies (Maeno et al., 2014; Iriyama and Toramaru, 2015) (Fig. 5.5).

Second, we describe the observation methods for obtaining a_M, q, and γ_M values as geological data. Figure 5.5 shows the stratigraphic variations of the maximum pumice radius corresponding to a_1, and the median particle radius a_{Md}. a_1 is defined as the average of the five largest particles in a layer, and a_{Md} is defined as the converted value from the value of Md_ϕ in Iriyama and Toramaru (2015) to a linear scale. In this study, we regard peak values of a_1 in a single eruption as observed values of a_M in the CS model. We obtained $a_M = 7.2$ mm for the first eruption.

The q value was obtained from the GSD plot of the entire sediment, which is composed by a single eruption as q_{obs}. We give constant density of the particles ρ_s as 1,200 kg/m^3 reported by Miyabuchi et al. (2013). The GSD of the entire sediment in a single eruption was obtained from the combination of the GSD data in each layer. The values of power–law exponent q were estimated by fitting the slope of GSD in the log–log plot of size versus population density (Fig. 6.1). For the entire range of sizes, we obtained $q_{obs} = 3.8$ for the first eruption (Fig. 6.1).

We describe a method for obtaining the values of a characteristic sedimentary structure γ_M. Regarding the peak position of a_M value through the stratigraphic variation as the top of the thickness h_M, we calculated the γ_M value ($\gamma_M = h_M/h_{tot}$). We obtained $\gamma_M = 0.54$ for the first eruption (Fig. 5.5).

We estimated the unknown dimensionless parameter ε_M of known geological data (a_M, q_{obs}, and γ_M), as illustrated in the preceding section. Eruption column heights observed by radar echo data are approximately 7,000 m for both the first (Shimbori et al., 2013). We regarded the eruption column heights observed by radar echo data as the source height H in the CS model. As shown as in Figure 3.9, we assumed TFV at sea level, which depends on the particle size and Reynolds number. As a result, we obtained ε_M values of 0.62 for the first eruption (Fig. 6.2).

From the observed values a_M and H, the fall times of the largest particle from the source height to the ground t_M were obtained as 270 s for the first eruption. By using the estimated ε_M value and the calculated t_M value, we estimated the source duration t_{src} in the CS model. As a result, we determined t_{src} values of approximately 440 s for the first eruption (Fig. 6.2).

In the case of the Shinmoe–dake 2011 eruptions, we obtained data for the eruption duration by geophysical observation (Shimbori et al., 2013). Therefore, we can check the applicability of our method by comparing the estimated and actual source durations or deposit characteristics.

Eruption durations have been reported as 2.5 h (approximately 9,000 s) for the first eruption (e.g., Shimbori et al., 2013). Thus, we assumed the observed eruption duration as the source duration in the CS model. For comparison, we show in in Figure 6.2 that the observed value of t_{src} is approximately 9×10^3 s for the first eruption. In addition, the estimated values of t_{src} are given as approximately 440 s for the first eruption. It was determined that estimated source durations t_{src} are underestimated. Thus, we examined the factors causing the difference in t_{src} values between estimation and observation. Underestimation of the source duration t_{src} was caused by underestimation of the non-dimensional parameter ε_M. As reported in previous studies, the GSD of all ejecta is close to the power–law distribution (e.g., Kaminski and Jaupart, (1998); Girault et al., 2014). However, as shown in Figure 6.1, the GSD plots convex upward. This suggests that the

procedure of automatic power–law fitting is not appropriate. If we assume that source GSDs have power–law distributions, the values for the finer particles may become incorrect owing to transportation effects. Two physical effects are assumed for the difference in the GSD plot: the fractionation effect during the expansion of the umbrella cloud and advection effect owing to the downwind movement during the fall process.

As a result of the particle fractionation from the expanding umbrella cloud, coarser particles generally settle in the proximal area, and fine particles settle in the distal area (Koyaguchi, 1994). This effect likely causes the GSDs to differ somewhat from the power–law distribution.

In addition, the advection effect owing to downwind movement appears to enhance the depletion of fine particles and to induce underestimation of fine particles at the ground compared with the source GSD.

On the basis of the aforementioned argument, we neglected the data of the finer particles and reobtained the power–law exponent q from the GSD plot by cutting off the plot range (Fig. 6.1). We define the cut–off power–law exponent as q_{c1} for that of $-2 \leq \phi \leq 1$ and q_{c2} for the size range $-2 \leq \phi \leq 0$. For the first eruption, we obtained $q_{c1} = 4.5$ and $q_{c2} = 5.1$ and estimated the source durations t_{src} as approximately 1,560 s and 9,750 s from the obtained ε_M as 0.18 and 0.03, respectively (Figs. 6.1 and 6.2). Therefore, we argue that the estimated source durations are in good agreement with the observed source durations within error if we consider the depletion of finer particle in estimating power–law exponents such as q_{c1} and q_{c2}. Thus, it is shown that the method of the CS model is useful when selecting the appropriate value of the power–law exponent q after considering the transportation mechanism of ejecta.

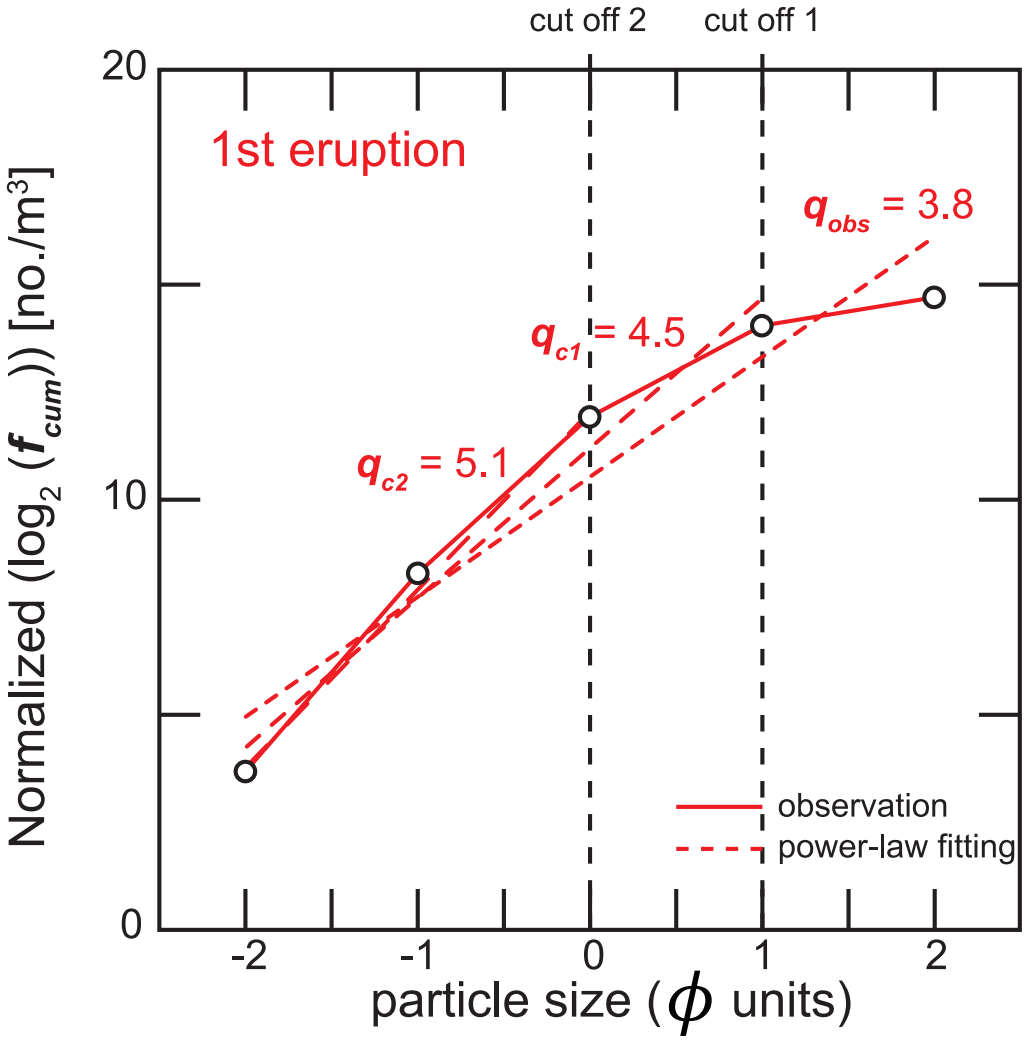

Figure 6.1: GSD plots of pyroclastic fall deposits produced by the first subplinian eruption of the Shinmoe–dake 2011 eruptions. *Mk-a* data reported in Iriyama and Toramaru (2015), 7.9 km southeast from the vent, are used. *Dashed lines*: Lines of power–law fittings. The Slope corresponds to the power–law exponent of cumulative GSD D (Kaminski and Jaupart, 1998), which is related as $q = D + 1$. q_{obs} is the power–law exponent which is obtained by the power law fitting for the GSD from the entire range of sizes. q_{c1} and q_{c2} are the power–law exponents which are obtained by the power–law fitting for the GSD within the size range of $-2 \leq \phi \leq 1$ and $-2 \leq \phi \leq 0$, respectively.

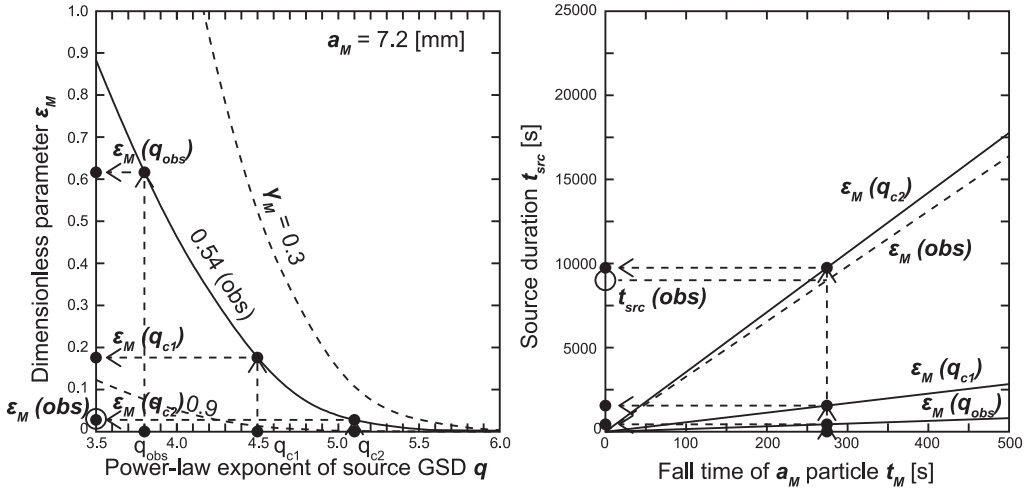

Figure 6.2: Results of the application of the CS model to the first subplinian eruption of the 2011 Shinmoe-dake eruptions. (left) Estimation of the parameter ε_M by using geological data a_M, q, and γ_M. (right) Estimation of the source duration. Closed circles represent the observed and estimated values from geological survey. Open circles represent the values which are obtained from geophysical observation.

6.2 Estimation of the temporal variation of the one–dimensional source GSD

As an application of the conservation of the number in the one–dimensional theory, we estimate the temporal variation of the source GSD $f_{src}(a, t')$. We assume that the source height $H(t')$ is constant during the eruption,

$$H(t') = H = \text{const.}, \tag{6.1}$$

then the conservation on the number in Equation (3.23) is

$$f_{stl}(a, t) = f_{src}(a, t'), \tag{6.2}$$

$$\left(\frac{\partial t'}{\partial t}\right)_a = 1. \tag{6.3}$$

The observed GSDs shown in Figure 6.3 are different to the f_{stl} because the volumetric fraction of the particles are different before settling and after settling, then

$$\varphi_s(z = 0, t) = \int_0^\infty f_{stl}(a, t) V^*(a) da, \tag{6.4}$$

$$\varphi_{PF}(t) = \int_0^\infty f_{sdm}(a, t) V^*(a) da, \tag{6.5}$$

where f_{sdm} is the GSD function of the sediment obtained by grain–size analysis. The relationship between f_{stl} and f_{sdm} is given by

$$f_{stl}(a, t) = f_{sdm}(a, t) \frac{\varphi_s(z = 0, t)}{\varphi_{PF}(t)}. \tag{6.6}$$

As an assumption, we give constant volumetric fraction of settling particles,

$$\varphi_s(z = 0, t) = \varphi_{stl} = \text{const.}, \tag{6.7}$$

where φ_{stl} is constant volumetric fraction of the settling particles. As an assumption, we give constant value of the volumetric fraction of the settling particles as $\varphi_{stl} = 10^{-6}$ based on the volumetric fraction of rain drop.The temporal variation of the settling GSD function is obtained shown in Figure 6.4.

We apply the conservation of the number as shown in Equation (6.2), and the the source GSDs is estimated as shown in Figure 6.5. We apply the result of the estimation of the source GSDs in the one–dimensional theory to the two–dimensional theories in the following chapter.

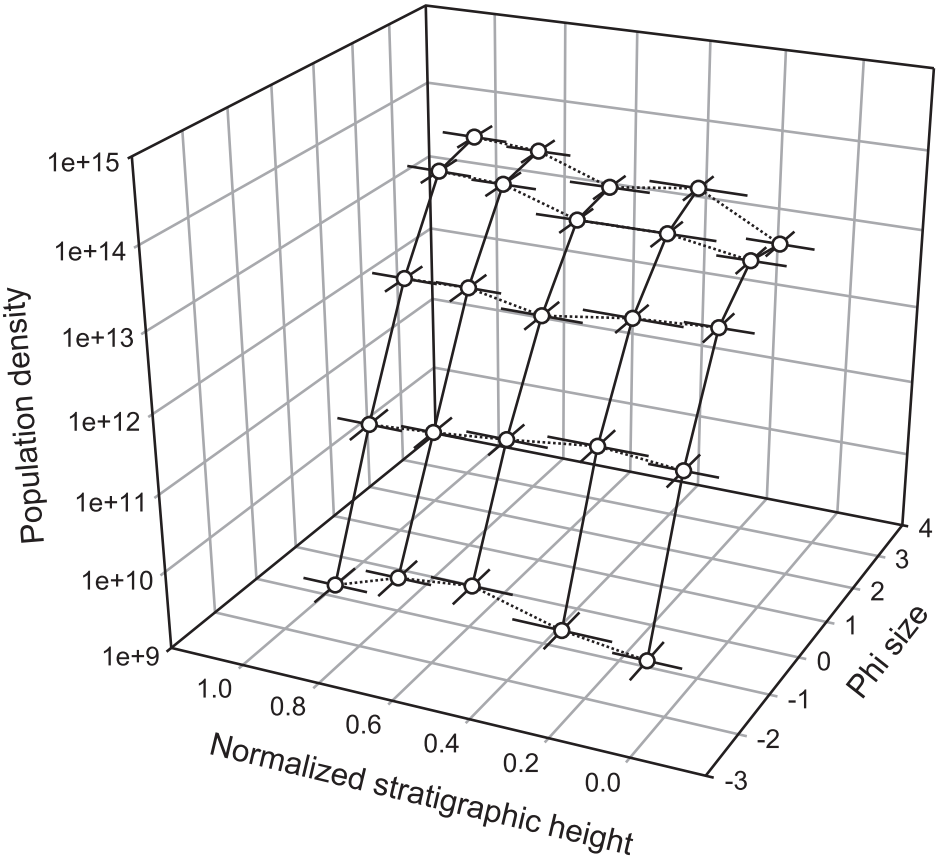

Figure 6.3: GSD plots of particles in the sediment converted from GSD data corresponding to the fraction of mass reported in Iriyama and Toramaru (2015)

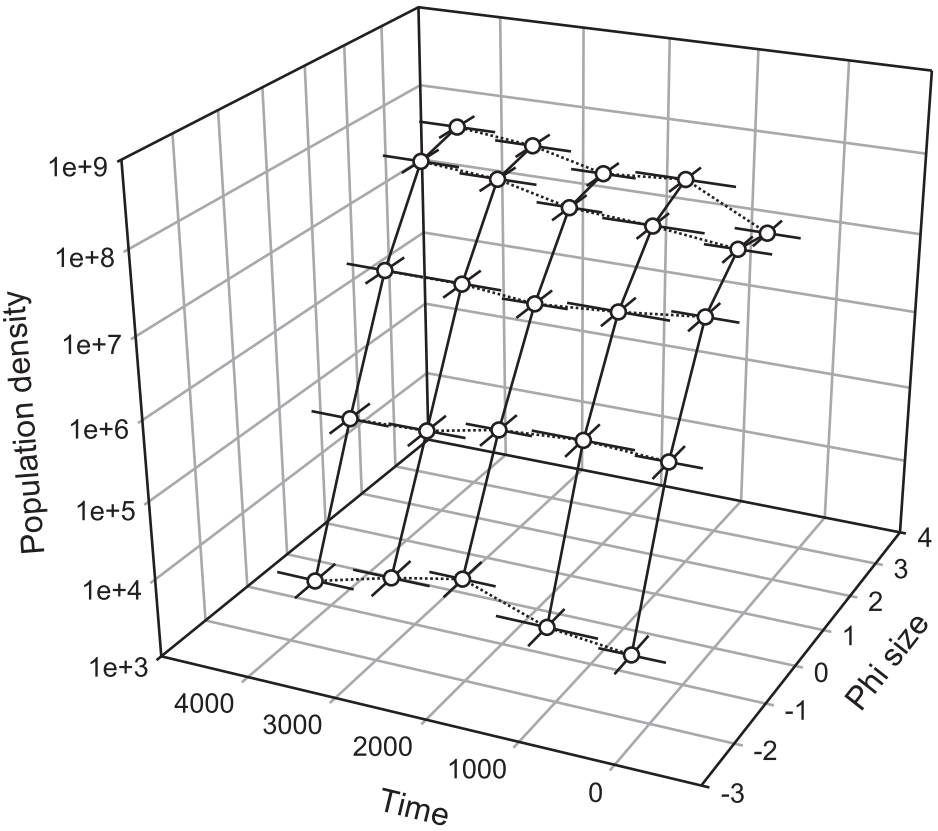

Figure 6.4: GSD plots of the settling particles estimated from GSD data of the sediment in Figure 6.3. The axis of normalized stratigraphic height in Figure 6.3 is converted to the time from the beginning of the sedimentation.

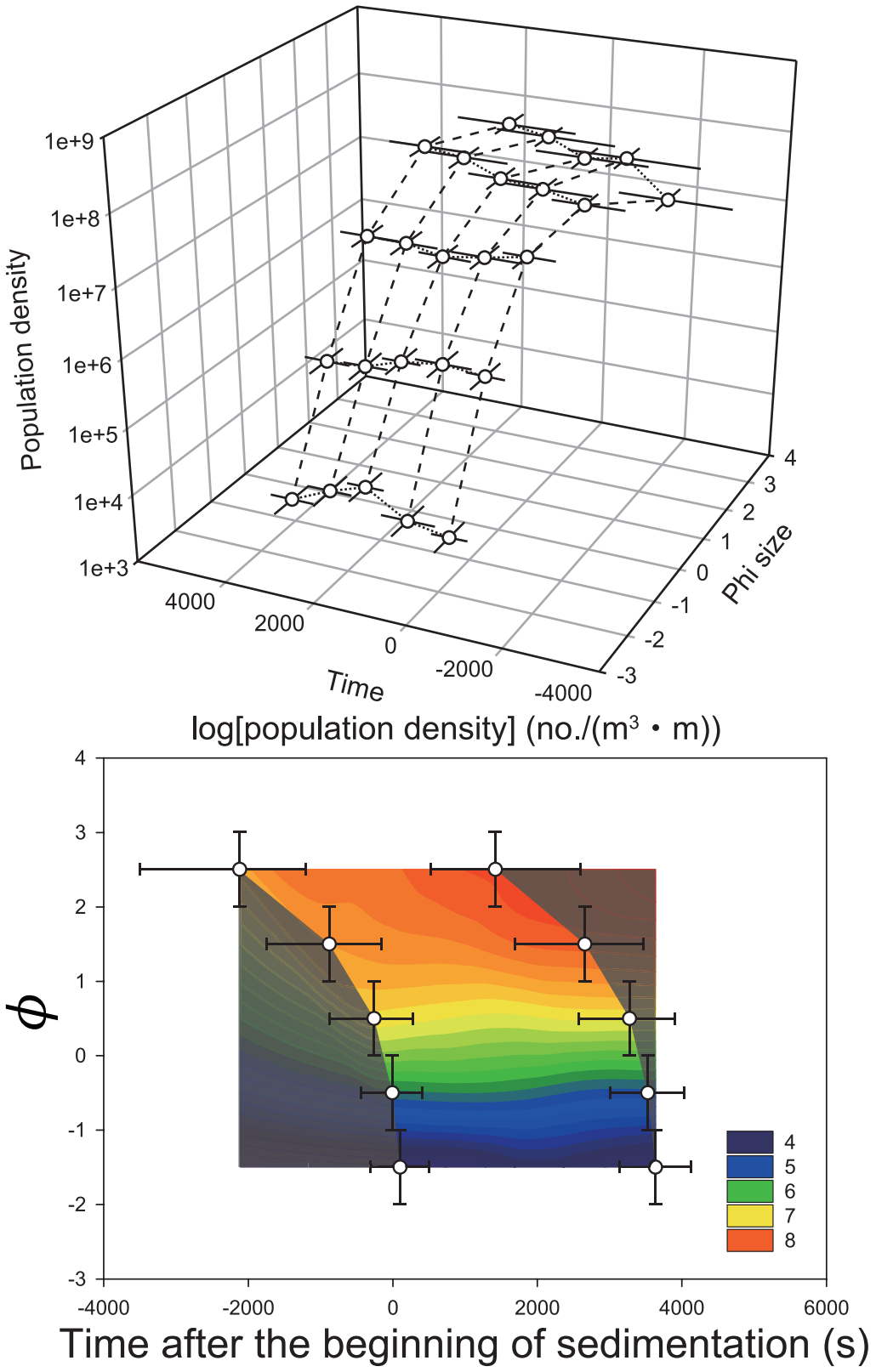

Figure 6.5: GSD plots of particles at the one–dimensional source position. The time zero corresponds to the beginning of the sedimentation.

Chapter 7

Application of two–dimensional models

In this chapter, we apply two–dimensional models to the 2011 Shinmoe–dake subplinian eruption. As an application of the constant source (CS) model, we identify the cause of the grading structure. And as an application of the constant height (CH) model, we estimate the temporal variation of the source GSD at the top of the eruption column $F_{src}(a, t')$.

7.1 Identification of the cause of the reverse grading structure

To identify the cause of the grading structure of the pyroclastic fall deposit, we applied the two–dimensional constant source (CS) model to the 2011 Shinmoe–dake subplinian eruption. According to eye–witness observation and satellite images of the ash cloud during the 2011 Shinmoe–dake subplinian eruption, the ash cloud spreads with a constant current velocity owing to the weak plume and strong velocity during the eruption. Thus, it seems that the constant current model is available. Available data are the wind profile $\bar{u}$ and u_b (Hashimoto et al., 2012), and heights of the ash cloud H_{cb} and H_{ct} including the thickness of the current L (Shimbori et al., 2013; Suzuki and Koyaguchi, 2013). We give constants as $\bar{u} = 10$ m/s, $u_b = 30$ m/s, $H_{cb} = 3,000$ m, $H_{ct} = 7,000$ m, and $L = 4,000$ m. Using these observed parameters, it is possible to identify the cause of the reverse grading

structure of the pyroclastic fall deposit at locality Mk by using the CS model.

In the constant current model, the grading structure depends on the ratio of $\bar{u}$ to u_b shown in Equation (4.83). In comparison, it satisfies $\bar{u} < u_b$ during the eruption. Thus, it is expected that the pyroclastic fall deposit with the normal grading structure by the constant supply. However, the reverse grading structure was reported, which suggests that the grading structure was formed owing not to the effect of the transportation in the constant supply, but to the effect of the temporal variation of the volcanic activity during the eruption.

Here, we estimate the temporal variation of the two–dimensional source GSD at the top of the eruption column during the 2011 Shinmoe–dake subplinian eruption in the following section.

7.2 Estimation of the temporal variation of the two–dimensional source GSD

By using observed data in chapter 7.1, we estimate the temporal variation of the two–dimensional source GSD. By using Equation (4.31), we obtain the relationship between the particle size a and the fractionation distance r' from which the particles arrive at the locality Mk (black line in Fig. 7.1). As shown in Figure 7.1, the larger particle size is, the closer the distance from the locality Mk to the fractionation distance is, which corresponds to the size dependence on the advection distance Δr. However, the fractionation distance of the $\phi \geq 1$ particles is estimated as $r' < 0$, which suggests that the particles are supplied from the upwind side of the current. In case of the 2011 Shiinmoe–dake subplinian eruption, however, there is no ash cloud in the upwind side. Therefore, it is not realistic to give the supply from the upwind side.

In consideration for the realistic transportation of ejecta, it is possible to occur the aggregation process. Recently, it has been reported that a large part of fine ash falls as aggregates (e.g., Taddeucci et al., 2011). Reported aggregates are composed by the

particles which are finer than 0.5 mm in diameter corresponding to $\phi = 1$ and the TFV of aggregates becomes larger than fall in individual particles composing the aggregates (Taddeucci et al., 2011). Assuming that particles which are finer than 0.5 mm in diameter make aggregates with a diameter 1 mm, then the relationship between the particle size and the fractionation distance for the particles which settle on the locality Mk is reobtained (red line in Fig. 7.1).

By using Equations (4.40) and the result of the estimated GSD in the one–dimensional model (Fig. 6.5), the temporal variation of the two–dimensional source GSD at the top of the eruption column, F_{src} is estimated (Fig. 7.2). As shown in Figure 7.2, fine particles increase monotonically, middle sized particles are almost constant, and coarse particles increase in the early stage and decrease in the late stage. We also obtain the temporal variation of the power–law exponent of the source GSD $D\left(t'\right)$ by obtained from the power–law fitting (Fig. 7.3).The D value decreases in the early stage, and increases in the late stage.

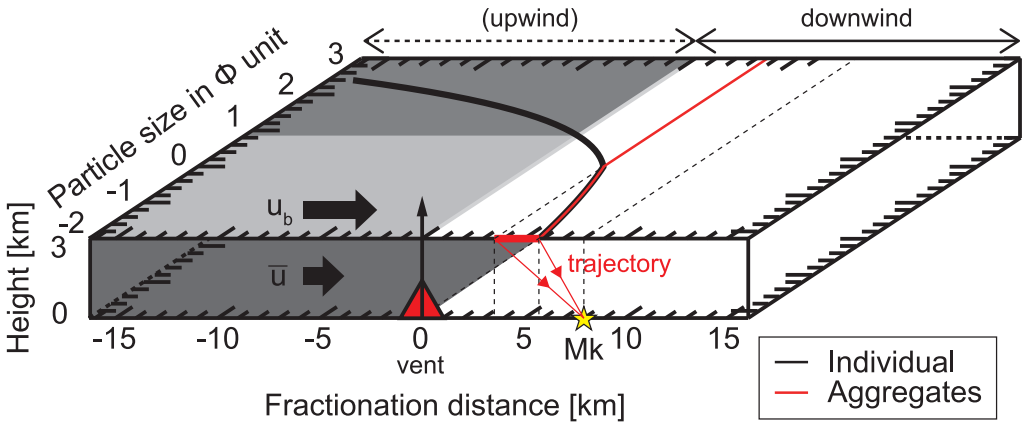

Figure 7.1: Plots of the relationship between the particle size and the fractionation distance at the source height. Black line indicates the individual fallout. Red line indicates aggregation fallout. The fall velocity of aggregates composed by fine particles with a size $\phi \geq 0$ is given as that with a size $\phi = 0$.

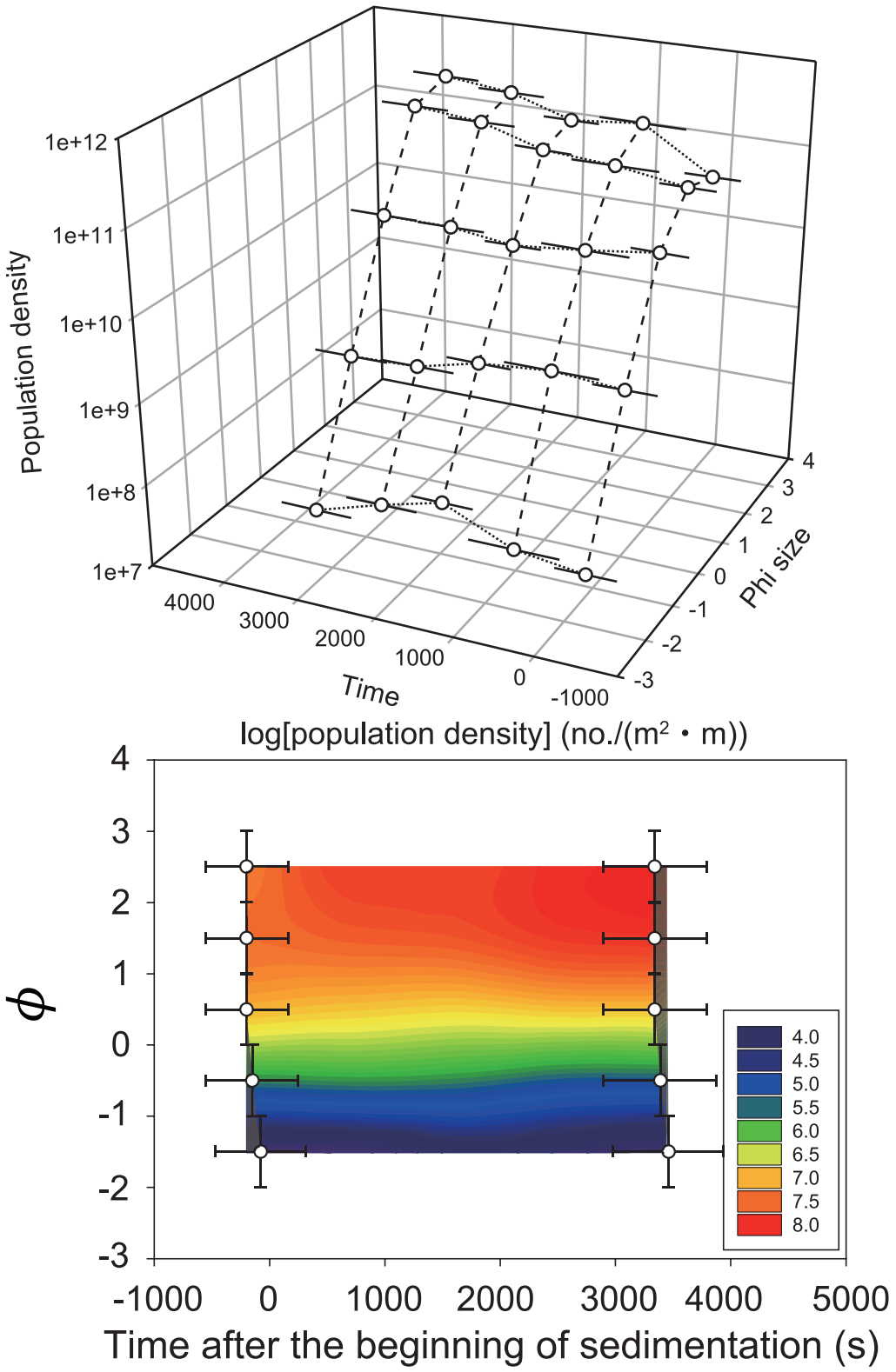

Figure 7.2: GSD plots of particles at the two–dimensional source position corresponding to the top of the eruption column.

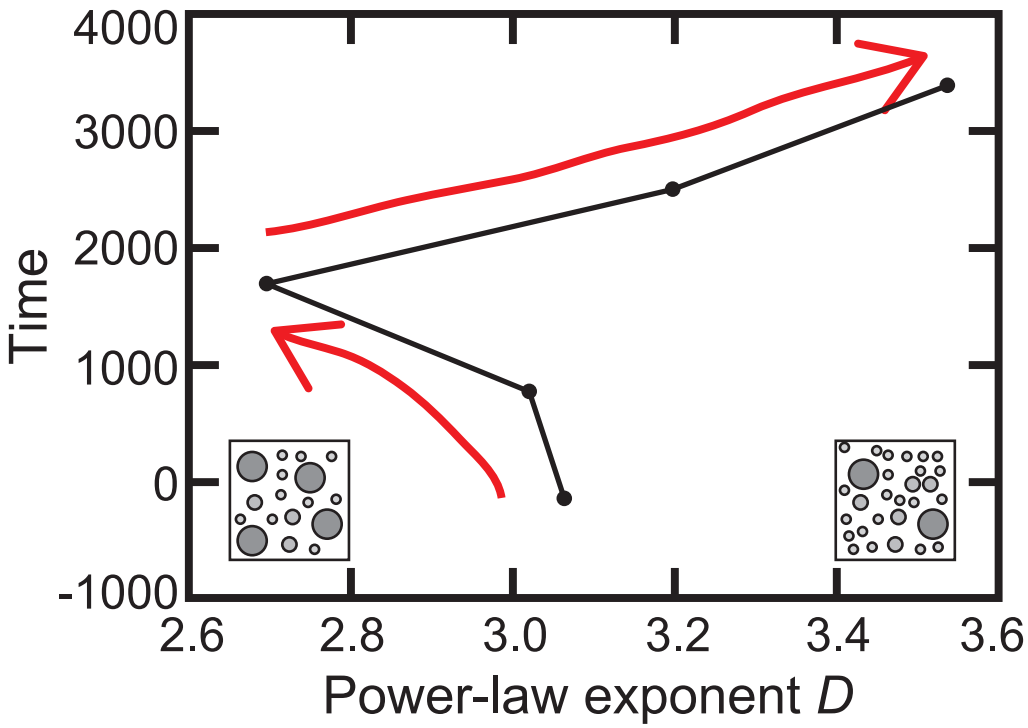

Figure 7.3: The temporal variation of the power–law exponent of the two–dimensional source GSD.

Chapter 8

Discussion

8.1 Comparison among the estimated source GSD and the observed data

In this section, we compare the temporal variations among the estimated GSD data in this study and observed data such as eruption column height and geodetic volume change. As shown in Figure 8.1, the D value have negative correlation to the eruption column height and the geodetic volume change. According to the results of the numerical study, the maximum height of the eruption column height H_t positively correlates to the power–law exponent D and the mass eruption rate under the steady-state calculation (Girault et al., 2014). If we assume that the steady–state was satisfied in any moment during the eruption, the mass eruption rate increased in the early stage according to the plots of the estimated D value and the observed H_t value (Fig. 8.1). The estimated temporal variation of mass eruption rate is consistent with that expected from the data of the geodetic volume change (Ueda et al., 2013). Thus, it seems that the estimation of the temporal variation of the source GSD during the eruption by using our theory is effective.

8.2 Summary of the 2011 Shinmoe–dake subplinian eruption

In this section, we summarize the volcanic activity during the 2011 Shinmoe–dake subplinian eruption (Fig. 8.2). In the early stage, the eruption began with a low mass eruption rate corresponding fine–rich particles, which made a low eruption column height. In the middle stage, the mass eruption rate reached a peak and coarse particles increased. The increase of the eruption column height was resulted not in the change of the GSD of ejecta but in the increase of the mass eruption rate. In the late stage, the mass eruption rate decreased and the GSD of ejecta become fine–rich decreasing the eruption column height.

Fine particles with a radius $\phi \geq 1$ composed aggregates during the fall process and enhance their transport efficiency. Owing to the temporal variation of the source GSD, the stratigraphy of the pyroclastic fall deposit at locality Mk showed the reverse grading structure in the lower part of the deposit and the normal grading structure in the upper part of the deposit.

8.3 Advantages of the models

In this section, we focus on the advantages of our models. It had been difficult to extract information on time from pyroclastic fall deposits in the past. The one–dimensional CS model enables us to estimate the source duration t_{src} by using geological data. We give a power–law source GSD as an assumption, but it is possible to apply similarity by giving various types of the source GSDs.

In the past, it had been significant question to identify the cause of the grading structure in the pyroclastic fall deposit. The two–dimensional CS model enables us to identify the cause of the grading structure owing whether to the transportation effect or to the temporal variation effect, which depends on the ratio of downwind velocity during the fall process $\bar{u}$ to the current velocity u_b in case of the constant current model.

In the past, it had been difficult to estimate the temporal variation of the source GSD quantitatively owing to the lack of the theory to reconstruction from the pyroclastic fall deposit. The conservation of the number in the one–dimensional theory and the two–dimensional CH model enable us to estimate the temporal variation of the source GSD from the point of view of the transportation and the sedimentation processes. Furthermore, the temporal variation of the source GSD suggests the temporal variation of the mass eruption rate. We need to check the temporal variation of textures in pyroclasts such as the bubble texture which is assumed to reflect physical the environment of fragmentation in the future.

8.4 Cautions in applying the CS model to natural plinian deposits

In this section, we discuss three limitations in applying the CS model. First, we address the selection of sampling locality. Two transportation styles occur in the formation of deposits from plinian eruptions: transportation from the margin of the eruption column and that from the bottom of the ash cloud (e.g., Koyaguchi and Ohno, 2001). In particular, particles are supplied from the margin of the eruption column in the proximal area (Class I fragments in Koyaguchi and Ohno, 2001), whereas they are supplied from the bottom of the NBL ash cloud in the distal area (Class Ⅱ fragments in Koyaguchi and Ohno, 2001). This difference in transportation style is supported by a kink in the plot of sediment thickness versus distance, or second root of area (e.g., Pyle, 1989; Fierstein and Nathenson, 1992; Bonadonna et al., 1998). Because we assumed particle supply from a constant height in the CS model, we selected geological data for distal sediments that correspond to Class Ⅱ fragments in Koyaguchi and Ohno (2001).

The second limitation is in the sampling method. When obtaining the γ_M value during the geological survey, caution must be taken with the spatial resolution of the sampling interval (Fig. 8.3). When the sampling interval is sufficiently smaller than $(h_{tot} - h_M)$,

we can obtain the true γ_M value from the stratigraphic variation of the maximum pumice radius a_1 (case 1 in Fig. 8.3). However, when the sampling interval is similar to or larger than $(h_{tot} - h_M)$, the disappearance point of a_M particles might not be detectable from the stratigraphic variation of a_1 (case 2 in Fig. 8.3). When the sampling interval is larger than $(h_{tot} - h_M)$, the a_1 becomes a_M for all sampling layers (Fig. 8.3). On the contrary, the a_{Md} value monotonically decreases from the bottom to the top of the sediment layer (Fig. 8.3). In particular, Md values change dramatically to the upper boundary of h_M (Fig. 8.3). In this case, the γ_M value can be estimated from the stratigraphic variations of a_{Md} (Fig. 8.3).

An additional indicator of γ_M is the sorting parameter σ. As shown in Figure (3.7), the sorting parameter σ in the CS model depends of the size range of the settling particles. Thus, the peak position of σ corresponds to the upper boundary of the h_M thickness, which becomes another key in obtaining γ_M as geological data.

8.5 Remaining problems

We estimated the temporal variation of the source GSD as a result of an application of the constant current model which is a kind of the two–dimensional theory. Then, the temporal variation of the mass eruption rate during the eruption is suggested accompanying the temporal variations of the source GSD and the eruption column height. However, the current velocity of the ash cloud u_b may depend on the mass eruption rate. It may be possible that the expansion of the ash cloud is regarded as constant current with a weak plume and a strong wind, even though the mass eruption rate temporally changes. Thus, we need to obtain the available range on the constant current model.

When the temporal variation of the mass eruption rate is important for the current velocity, our theory should be extended to unsteady cases. It is assumed that the temporal variation of the settling GSD becomes complex in such cases. Thus, to reconstruct the temporal variation of the source GSD from pyroclastic fall deposits, we need GSD data

of the sediment not only from a single locality, but also from multiple localities. Then, the source GSD would be estimated as an optimum solution in the future.

8.6 Future work

We provide a theory to estimate the temporal variation of the source GSD during the eruption. Following studies will also make clear the more detailed variation of the source GSD and its relationship to the plume dynamics. Estimated GSD variation will be helpful for the study of the volcanopetrology in which the temporal variation of the physical and chemical variations of magmatic processes will be estimated.

Furthermore, transportation and sedimentation processes are common mechanisms not only for the volcanology but also for various types of geology. Thus, our theory is applied to many kinds of sediments as a fundamental description.

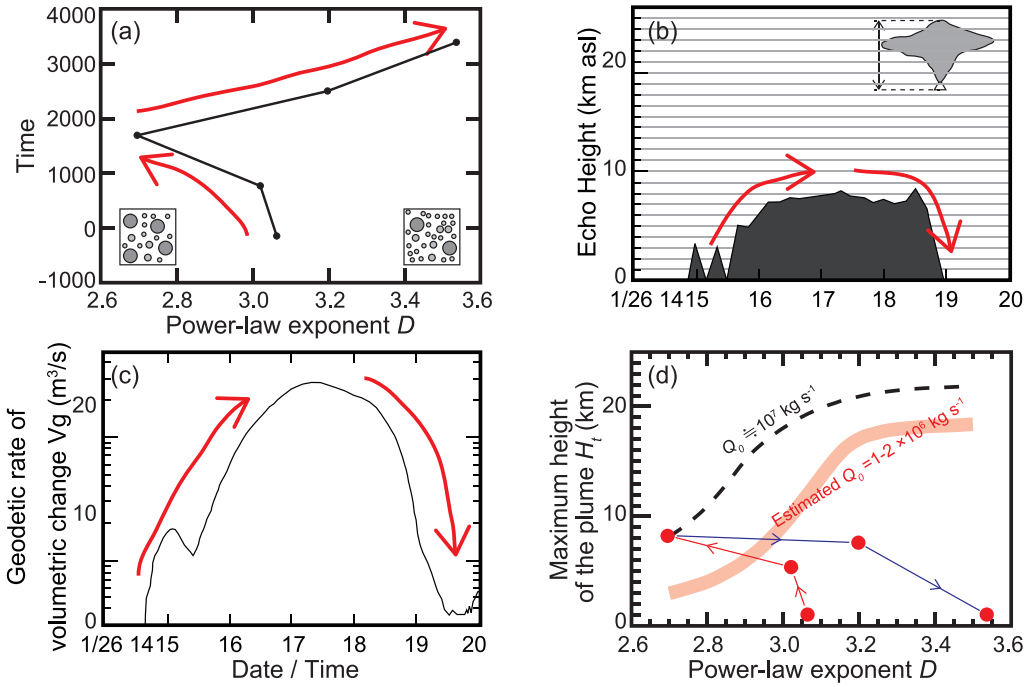

Figure 8.1: Temporal variations of (a) power–law exponent of the two–dimensional source GSD estimated in this study, (b) eruption column height observed by radar echo data (Shimbori et al., 2013), and (c) geodetic rate of volumetric change (Ueda et al., 2013; Ichihara, 2016). (d) Relationship among the maximum height of the plume, exponent of power–law source GSD, and mass eruption rate at the vent obtained from the steady–state calculation of the plume dynamics (Girault et al., 2014). Red circles indicate the temporal variation of estimated exponent and observed eruption column height. Expected change of the mass eruption rate is similar to geodetic rate of volumetric change in (c).

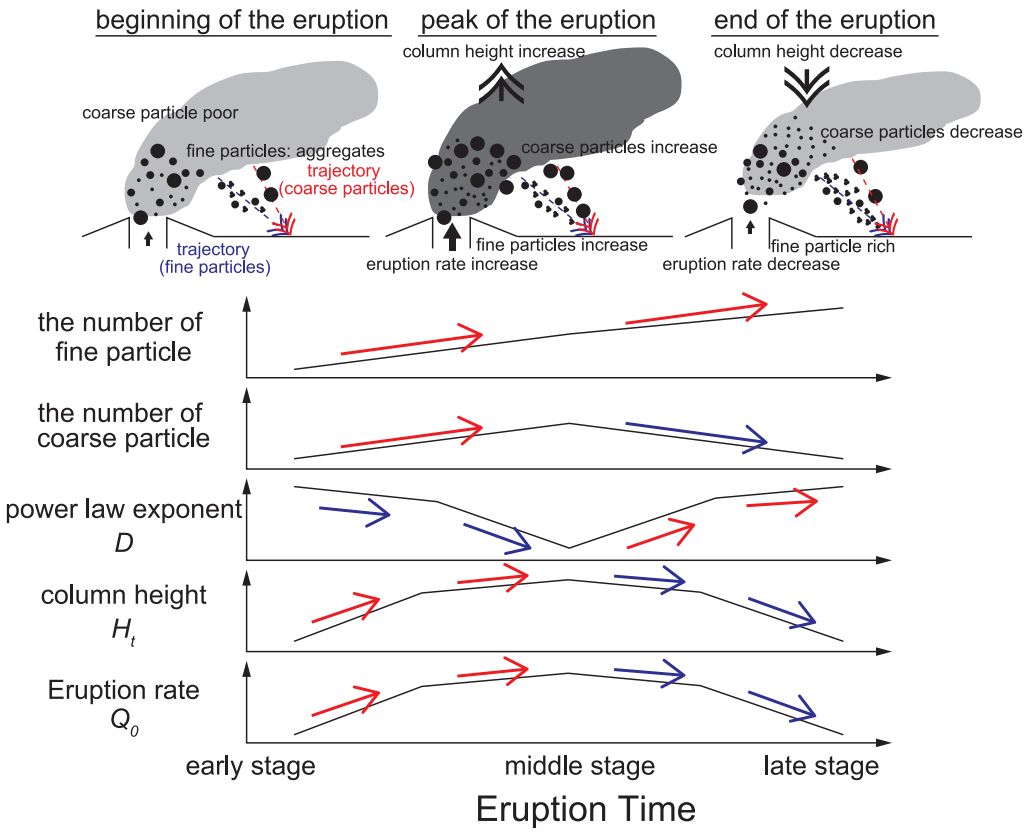

Figure 8.2: Summary of the first subplinian eruption of the 2011 Shinmoe–dake eruption.

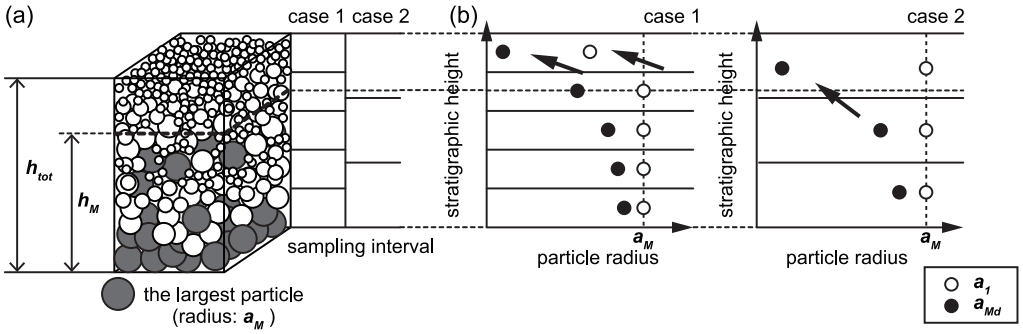

Figure 8.3: (a) A schematic illustration of the pyroclastic fall deposit produces by the CS model. Case 1 and 2 represent the difference of thickness of the sampling interval. (b) Expected results of the stratigraphic variations of the maximum pumice radius (a_1; open circles) and the median radius (a_{Md}, closed circles). When the thickness of the sampling interval is smaller than $(h_{tot} - h_M)$, rapid variations may be detectable in both of the a_1 and the a_{Md}. However, when the thickness of the sampling interval is larger than $(h_{tot} - h_M)$, the stratigraphic variation of a_1 may be constant and rapid variation may be detectable only in the a_{Md}.

Chapter 9

Conclusions

We developed a theory for the transportation and sedimentation during the volcanic eruption. We defined the GSD function and made it possible to the transportation and the sedimentation processes quantitatively. We first developed a methodology to reconstruct the unsteady change of the source GSD from the settling GSD in the one–dimensional case. In the one–dimensional CS model, we made it possible to estimate the source duration. The two–dimensional CS model enables us to identify the cause of the grading structure of the fall deposit. And the two–dimensional CH model enables us to estimate the temporal variation of the source GSD.

We applied our theories to the 2011 Shinmoe–dake subplinian eruption. As an application of the one–dimensional CS model, we estimated the source duration, which was reasonable value compared to the observed eruption duration. By using the two–dimensional CS model, the reverse grading structure in the pyroclastic fall deposit at locality Mk was made by the temporal variation of the volcanic activity. As an application of the two–dimensional CS model, we estimated the temporal variation of the source GSD at the top of the eruption column. Estimated source GSD suggests the relationship to the dynamics of the volcanic plume such as the values of the eruption column height and the mass eruption rate.

Acknowledgments

The author thanks Prof. Atsushi Toramaru (Dept. of Earth and Planetary Sciences, Fac. of Science, Kyushu Univ.) for giving chances to experience exciting discussion in the fields and the laboratory. The author also thanks Prof. Emeritus Tetsuo Yamamoto (Institute of Low Temperature Science, Hokkaido Univ.), Assoc. Prof. Mie Ichihara (Earthquake Research Institute, The University of Tokyo), Assist. Prof. Yujiro J. Suzuki (Earthquake Research Institute, The University of Tokyo), and Assist. Prof. Fukashi Maeno (Earthquake Research Institute, The University of Tokyo) for discussions and helpful comments; and Assoc. Prof. Takeshi Ikeda (Dept. of Earth and Planetary Sciences, Fac. of Science, Kyushu Univ.) and Assist. Prof. Tomoharu Miyamoto (Dept. of Earth and Planetary Sciences, Fac. of Science, Kyushu Univ.) for daily discussion and encouragements. This work was supported by JSPS KAKENHI grants 15J00926.

Notation

Latin letters

a	particle radius, [L].
a_m	cut off particle radius in calculation, [L].
a_M	the largest particle radius in whole particles, [L].
a_{Md}	median particle radius, [L].
a_1	the maximum particle radius of settling particles, [L].
a_2	the minimum particle radius of settling particles, [L].
A	constant in Equation, (3.46).

b	the increaseing rate of the source height in the Linear Height Increase (LHI) model.
B	constant in equation, (3.47).
c	constant of terminal fall velocity in Equations (3.33) and (3.85).
C	constant in Equation (3.48).
C_d	drag coefficient.
C^{GC}	constant in the gravity current model in Equation (4.66).
D	power–law exponent in Equation (3.41).
f	GSD function for unit volume $[N/(L^3 \cdot L)]$.
f_{cum}	cumulative GSD function of particles per unit volume $[N/L^3]$.
f_{frc}	GSD function of fractionated particles from the ash cloud per unit volume $[N/(L^3 \cdot L)]$.
f_{sdm}	GSD function of particles in deposit per unit volume $[N/(L^3 \cdot L)]$.
f_{src}	GSD function particles at the source height per unit volume $[N/(L^3 \cdot L)]$.
f_{src}^{CS}	GSD function particles at the source height in the CS model per unit volume $[N/(L^3 \cdot L)]$.
f_{stl}	GSD function of settling particles per unit volume $[N/(L^3 \cdot L)]$.
f_{tot}	total number of particles per unit volume $[N/(L^3)]$.
F	GSD function particles per unit area $[N/(L^2 \cdot L)]$.
F_{src}	GSD function particles at the top of the eruption column per unit area $[N/(L^2 \cdot L)]$.
F_{tot}	total number of particles per unit area $[N/(L^2)]$.
F_{AC}	GSD function particles in the ash cloud per unit area $[N/(L^2 \cdot L)]$.
G	time relation function $[T]$.
g	acceleration of gravity $[L/T^2]$.
h	stratigraphic height $[L]$.
h_a	stratigraphic interval existing size a particles $[L]$.
h_{eff}	effective thickness in Equation (3.59) $[L]$.
h_{tot}	total thickness of sediment $[L]$.
h_M	stratigraphic interval which includes size a_M particles $[L]$.
H	source height $[L]$.

H_b height of the bottom of the ash cloud which corresponds to neutral bouyancy level $[L]$.

H_{cb} height of the bottom of the current of the ash cloud $[L]$.

H_{ct} height of the top of the current of the ash cloud, $[L]$.

H_t height of the top of the eruption column, $[L]$.

H_0 initial height of the source in the Linear Height Increase (LHI) model, $[L]$.

$\boldsymbol{j_m}$ the mass flux of falling particles with size a $[M/(L^2 \cdot L \cdot T)]$.

j_m vertical component of the mass flux of falling particles with size a $[M/(L^2 \cdot L \cdot T)]$.

$\boldsymbol{j_n}$ the number flux of falling particles with size a $[N/(L^2 \cdot L \cdot T)]$.

j_n vertical component of the number flux of falling particles with size a $[N/(L^2 \cdot L \cdot T)]$.

$\boldsymbol{j_v}$ the volume flux of falling particles with size a $[L^3/(L^2 \cdot L \cdot T)]$.

j_v vertical component of the volume flux of falling particles with size a $[L^3/(L^2 \cdot L \cdot T)]$.

$\boldsymbol{J_m}$ the mass flux of falling particles $[M/(L^2 \cdot T)]$.

J_m vertical component of the mass flux of falling particles $[M/(L^2 \cdot T)]$.

$\boldsymbol{J_n}$ the number flux of falling particles $[N/(L^2 \cdot T)]$.

J_n vertical component of the number flux of falling particles, $[N/(L^2 \cdot T)]$.

$\boldsymbol{J_v}$ the volume flux of falling particles $[L^3/(L^2 \cdot T)]$.

J_v vertical component of the volume flux of falling particles $[L^3/(L^2 \cdot T)]$.

L the thickness of the current of the ash cloud, $[L]$

m the mass distribution, $[M/(L^3 \cdot L)]$.

Md_ϕ median particle size in ϕ scale.

n constant in Equation (3.42).

N Brunt-Väisälä frequency.

p constant in Equations (3.33) and (3.84).

q exponent of power–law source grain–size distribution in Equation (3.42).

q_{c1} exponent of power–law source grain–size distribution cut–offed $-2 \leq \phi \leq 1$.

q_{c2} exponent of power–law source grain–size distribution cut–offed $-2 \leq \phi \leq 0$.

q_{obs} exponent of power–law source grain–size distribution observed by grain-size analysis.

Q volumetric flow rate into the ash cloud, $[L^3/T]$.

Q_0 mass eruption rate, $[M/T]$.

r horizontal distance from the vent $[L]$.

r_c boundary distance between normal grading structure and reverse grading structure, $[L]$.

r_M advection distance of the largest particles with size a_M $[L]$.

r' horizontal distance from the vent at the source position $[L]$.

r'^C_b boundary distance which satisfies $Ri = 1$ in the cylinder model, $[L]$.

r'^F_b boundary distance which satisfies $Ri = 1$ in the fan model, $[L]$.

r'^{GC}_b boundary distance which satisfies $Ri = 1$ in the gravity current model, $[L]$.

r'_c boundary distance which equals to $r_c - r_M$, $[L]$.

$\hat{\boldsymbol{r}}$ unit vector with component r.

R particle radius, [L].

Re particle Raynolds number.

Ri Richardson number.

t time at an object height $[T]$.

t_a fall time of particles with size a from source height to the ground $[T]$.

t_h horizontal travel time in the ash cloud $[T]$.

t_m fall time of particles with size a_m from source height to the ground $[T]$.

t_{src} supply duration at the source, $[T]$.

t_{tot} total travel time from departure to arrival $[T]$.

t_{v_t} fall time of particles with TFV v_t from source height to the ground $[T]$.

t_M fall time of particles with size a_M from source height to the ground $[T]$.

t' time at the source height $[T]$.

t^* duration existing in a system $[T]$.

u x axis component of the wind velocity $\boldsymbol{v}$, $[L/T]$.

u_b current velocity of the ash cloud, $[L/T]$.

u^C_b current velocity of the ash cloud in the cylinder model, $[L/T]$.

u_b^{CC} current velocity of the ash cloud in the constant current model, $[L/T]$.

u_b^F current velocity of the ash cloud in the fan model, $[L/T]$.

u_b^{GC} current velocity of the ash cloud in the gravity current model, $[L/T]$.

u_w x or r axis component of average wind velocity at neutral buoyancy level, $[L/T]$.

$\bar{u}$ x or r axis component of average wind velocity, $[L/T]$.

$\boldsymbol{v}$ wind velocity, $[L/T]$.

v y axis component of the wind velocity $\boldsymbol{v}$, $[L/T]$.

v_t terminal fall velocity, $[L/T]$.

v_c terminal fall velocity of the critical particle size, $[L/T]$.

$\bar{v}$ y axis component of average wind velocity, $[L/T]$.

V volume distribution, $[L^3/\left(L^3 \cdot L\right)]$.

V^C volume of the ash cloud in the cylinder model, $[L^3]$.

V^F volume of the ash cloud in the fan model, $[L^3]$.

V^* volume of size a particle $[L^3/N]$.

w z axis component of the wind velocity $\boldsymbol{v}$, $[L/T]$.

$\bar{w}$ z axis component of average wind velocity, $[L/T]$.

x coordinate of the Cartesian coordinate system, $[L]$.

x' coordinate of the Cartesian coordinate system at the source position, $[L]$.

$\hat{\boldsymbol{x}}$ unit vector of x coordinate.

y coordinate of the Cartesian coordinate system, $[L]$.

y' coordinate of the Cartesian coordinate system at the source position, $[L]$.

$\hat{\boldsymbol{y}}$ unit vector of y coordinate.

z coordinate of the Cartesian coordinate system, $[L]$.

z' coordinate of the Cartesian coordinate system at the source position, $[L]$.

$\hat{\boldsymbol{z}}$ unit vector of z coordinate.

Greek letters

α_m	dimensionless particle radius of the smallest particles scaled by the largest radius.
γ_a	thickness ratio of h_a to h_{tot} in the constant source (CS) model.
γ_M	thickness ratio of h_M to h_{tot} in the constant source (CS) model.
δ	delta function.
ε_a	time scale ratio in Equation (3.71).
ε_m	time scale ratio in Equation (3.72).
ε_M	time scale ratio in Equation (3.70).
ζ	solution of the delta function in Equation (3.20).
θ	center angle of the fan-shaped ash cloud in the Fan model, $[radian]$.
λ	constant in equation (4.66)
μ	dynamic viscosity of the atmosphere $[L^2/T]$.
π	circular constant.
ρ_l	density of liquid phase (atmosphere), $[M/L^3]$
ρ_s	density of solid phase (particle), $[M/L^3]$
σ	sorting parameter of the grain-size distribution.
σ_ϕ	sorting parameter of the grain-size distribution in ϕ unit.
τ'	dimensionless time scaled by the source duration.
ϕ	particle size in phi scale.
φ_{src}	volume fraction of particles at the source height.
φ_{stl}	volume fraction of settling particles.
φ_{PF}	volume fraction of particles in sediment corresponding to packing fraction of sediment.
$\sqcap$	rectangular function.

References

[1] Alibidirov, M., and D. B. Dingwell (1996), Magma fragmentation by rapid decompression, *Nature*, *380*, 146–148, doi10.1038/380146a0.

[2] Bonadonna, C., and A. Costa (2013), Plume height, volume, and classification of explosive volcanic eruptions based on the Weibull function, *Bull. Volcanol*, *75*, 742, doi:10.1007/s00445-013-0742-1.

[3] Bonadonna, C., G. G. J. Ernst, and R. S. J. Sparks (1998), Thickness variations and volume estimates of tephra fall deposits: The importance of particle Reynolds number, *J. Volcanol. Geotherm. Res.*, *81*, 173–187, doi:10.1016/S0377-0273(98)00007-9.

[4] Bonadonna, C., and B. F. Houghton (2005), Total grain-size distribution and volume of tephra-fall deposits, *Bull. Volcanol.*, *67*, 441, doi:10.1007/s00445-004-0386-2.

[5] Bonadonna, C., and J. C. Phillips (2003), Sedimentation from strong volcanic plumes, *J. Geophys. Res.*, *108*, 2340, doi:10.1029/2002JB002034.

[6] Bonadonna, C., J. C. Phillips, and B. F. Houghton (2005), Modeling tephra sedimentation from a Ruapehu weak plume eruption, *J. Geophys. Res.*, *110*, B08209, doi:10.1029/2004JB003515.

[7] Carey, S., and H. Sigurdsson (1987), Temporal variations in column height and magma discharge rate during the 79 AD eruption of Vesuvius, *Geol. Soc. Am. Bull.*, *99*, 303–314, doi:10.1130/0016-7606(1987)99<303:TVICHA>2.0.CO;2.

[8] Carey, S., and R. S. J. Sparks (1986), Quantitative models of the fallout and dispersal of tephra from volcanic eruption columns, *Bull. Volcanol.*, *48*, 109–125, doi:10.1007/BF01046546.

[9] Costa, A., A. Folch, and G. Macedonio (2013), Density-driven transport in the umbrella region of volcanic clouds: Implications for tephra dispersion models, *Geophys. Res. Lett.*, *40*, 4823–4827, doi:10.1002/grl.50942.

[10] Costa, A., L. Pioli, and C. Bonadonna (2016), Assessing tephra total grain-size distribution: Insights from field data analysis, *Earth Planet. Sci. Lett.*, *443*, 90–107, doi:10.1016/j.epsl.2016.02.040.

[11] Fierstein, J., and M. Nathenson (1992), Another look at the calculation of fallout tephra volumes, *Bull. Volcanol.*, *54*, 156–167, doi:10.1007/BF00278005.

[12] Folch, A. (2012), A review of tephra transport and dispersal models: Evolution, current status, and future perspectives, *J. Volcanol. Geotherm. Res.*, *235–236*, 96–115, doi:1010.1016/j.jvolgeores.2012.05.020.

[13] Fukuoka District Meteorological Observatory, and Kagoshima Local Meteorological Observatory (2012), *Volcanic Regular Bulletin of Kirishima Volcano in 2011*, pp. 31 (in Japanese).

[14] Girault, F., G. Carazzo, S. Tait, F. Ferrucci, and E. Kaminski (2014), The effect of total grain-size distribution on the dynamics of turbulent volcanic plumes, *Earth Planet. Sci. Lett.*, *394*, 124–134, doi:10.1016/j.epsl.2014.03.021.

[15] Hartmann, W. L. (1969), Terrestrial, lunar, and interplanetary rock fragmentation, *Icarus*, *10*, 201–213, doi:10.1016/0019-1035(69)90022-0.

[16] Hashimoto, A., T. Shimbori, and K. Fukui (2012), Tephra fall simulation for the eruptions at Mt. Shinmoe-dake during 26–27 January 2011 with JMANHM, *SOLA*, *8*, 37–40, doi:10.2151/sola.2012-010.

[17] Ichihara, M. (2016), Seismic and infrasonic eruption tremors and their relation to magma discharge rate: A case study for sub-Plinian events in the 2011 eruption of Shinmoe-dake, Japan, *J. Geophys. Res. Solid Earth*, *121*, 7101–7118, doi:10.1002/2016JB013246.

[18] Iriyama, Y., and A. Toramaru (2015), Stratigraphic Variations in Grain-size Characteristics of Pyroclastic Fall Deposits During the 2011 Subplinian Eruptions of Shinmoedake, Kirishima Volcano, Japan, *Bull. Volcanol. Soc. Japan*, *60*, 399–410 (in Japanese with English abstract).

[19] Kaminski, E., and C. Jaupart (1998), The size distribution of pyroclasts and the fragmentation sequence in explosive volcanic eruptions, *J. Geophys. Res.*, *103*, 29759–29779, doi:10.1029/98JB02795.

[20] Koyaguchi, T. (1994), Grain-size variation of the tephra derived from volcanic umbrella cloud, *Bull. Volcanol.*, *56*, 1–9, doi:10.1007/BF00279724.

[21] Koyaguchi, T., and M. Ohno (2001), Reconstruction of eruption column dynamics on the basis of grain size of tephra fall deposits, 1, Methods, *J. Geophys. Res.*, *106*, 6499–6512, doi:10.1029/2000JB900426.

[22] Kozono, T., H. Ueda, T. Ozawa, T. Koyaguchi, E. Fujita, A. Tomiya, and Y. J. Suzuki (2013), Magma discharge variations during the 2011 eruptions of Shinmoe-dake volcano, Japan, revealed by geodetic and satellite observations *Bull. Volcanol.*, *75*, 695–707, doi:10.1007/s00445-013-0695-4.

[23] Kueppers, U., D. Perugini, and D. Dingwell (2006), “Explosive energy” during volcanic eruptions from fractal analysis of pyroclasts, *Earth Planet. Sci. Lett.*, *248*, 3–4, doi:10.1016/j.epsl.2006.06.033.

[24] Kunii, D., and O. Levenspiel (1969), *Fluidisation Engineering*, John Wiley, New York.

[25] Ledbetter, M. and R. S. J. Sparks (1979), Duration of large-magnitude explosive eruptions deduced from graded bedding in deep-sea ash layers, *Geology*, *7*, 240–244, doi:10.1130/0091-7613(1979)7<240:DOLEED>2.0.CO;2.

[26] Maeno, F., M. Nagai, S. Nakada, R. E. Burden, S. Engwell, Y. Suzuki, and T. Kaneko (2014), Constraining tephra dispersion and deposition from three sub-plinian explosions in 2011 at Shinmoedake volcano, Kyushu, Japan, *Bull. Volcanol.*, *76*, 823–838, doi:10.1007/s00445-014-0823-9.

[27] Martin, D. and R. S. Nokes (1988), Crystal settling in a vigorously convecting magma chamber, *Nature*, *332*, 534–536, doi:10.1038/332534a0.

[28] Miyabuchi, Y., D. Hanada, H. Niimi, and T. Kobayashi (2013), Stratigraphy, grain-size and component characteristics of the 2011 Shinmoedake eruption deposits, Kirishima Volcano, Japan, *J. Volcanol. Geotherm. Res.*, *258*, 31–46, doi:10.1016/j.jvolgeores.2013.03.027.

[29] Nakada, S., M. Nagai, T. Kaneko, Y. Suzuki, and F. Maeno (2013), The outline of the 2011 eruption at Shinmoe-dake (Kirishima), Japan, *Earth Planets Space*, *65*, 475–488, doi:10.5047/eps.2013.03.016.

[30] Ozawa, T., and T. Kozono (2013), Temporal variation of the Shinmoe-dake crater in the 2011 eruption revealed by spaceborne SAR observations, *Earth Planets Space*, *65*, 527–538, doi:10.5047/eps.2013.05.004.

[31] Pyle, D. M. (1989), The thickness, volume and grain size of tephra fall deposits, *Bull. Volcanol.*, *51*, 1–15, doi:10.1007/BF01086757.

[32] Rust, A. C., and K. V. Cashman (2011), Permeability controls on expansion and size distributions of pyroclasts, *J. Geophys. Res.*, *116*, B11202, doi:10.1029/2011JB008494.

[33] Shimbori, T., T. Sakurai, M. Tahara, and K. Fukui (2013), Observation of eruption clouds with weather radars and meteorological satellites: A case study of the eruptions at Shinmoedake volcano in 2011, *Q. J. Seismolog.*, *77*, 139–214.

[34] Sparks, R. S. J. (1986), The dimensions and dynamics of volcanic eruption columns, *Bull. Volcanol.*, *48*, 3–16, doi:10.1007/BF01073509.

[35] Sparks, R. S. J., M. Bursik, S. Carey, J. Gilbert, L. Glaze, H. Sigurdsson, and A. Woods (1997), *Volcanic Plumes*, pp. 574, John Wiley & Sons Ltd., Chichester, U. K.

[36] Suzuki, T. (1983), A theoretical model for dispersion of tephra, *In: Shimozuru, D., Yokoyama, I. (Eds.), Volcanism: Physics and Tectonics. Arc, Tokyo*, pp. 95–113.

[37] Suzuki, Y. J., and T. Koyaguchi (2013), 3D numerical simulation of volcanic eruption clouds during the 2011 Shinmoe-dake eruptions *Earth Planets Space*, *65*, 581–589, doi:10.5047/eps.2013.03.009.

[38] Taddeucci, J., P. Scarlato, C. Montanaro, C. Cimarelli, E. Del Bello, C. Freda, D. Andronico, M. T. Gudmundsson, and D. B. Dingwell (2011), Aggregation-dominated ash settling from the Eyjafjallajökull volcanic cloud illuminated by field and laboratory high-speed imaging, *Geology*, *39*, 891–894, doi:10.1130/G32016.1.

[39] Turcotte, D. L. (1986), Fractals and fragmentation, *J. Geophys. Res.*, *91*, 1921–1926, doi:10.1029/JB091iB02p01921.

[40] Ueda, H., T. Kozono, E. Fujita, Y. Kohno, M. Nagai, T. Miyagi, and T. Tanada (2013), Crustal deformation associated with the 2011 Shinmoe-dake eruption as observed by tiltmeters and GPS, *Earth Planets Space*, *65*, 517–525, doi:10.5047/eps.2013.03.001.

[41] Walker, G. P. L. (1973), Explosive volcanic eruptions: A new classification scheme, *Geol. Runtisch.*, *62*, 431–446, doi:10.1007/BF01840108.

[42] Walker, G. P. L. (1980), The Taupo pumice: Product of the most powerful known (ultraplinian) eruption?, *J. Volcanol. Geotherm. Res.*, *8*, 69–94, doi:10.1016/0377-0273(80)90008-6.

[43] Wilson, L. (1976), Explosive volcanic eruptions–III. Plinian eruption columns, *Geophys. J. R. Astron. Soc.*, *45*, 543–556, doi:10.1111/j.1365-246X.1976.tb06909.x.

[44] Woods, A. W. (1988), The fluid dynamics and thermodynamics of eruption columns, *Bull. Volcanol.*, *50*, 169–193, doi:10.1007/BF01079681.